UNIVERSITY OF OKLAHOMA

GRADUATE COLLEGE

COMPARISON OF SURFACE AND DOWNHOLE MICROSEISMIC ACQUISITION

A THESIS

SUBMITTED TO THE GRADUATE FACULTY

in partial fulfillment of the requirements for the

Degree of

MASTER OF SCIENCE

By

KARA ROHAN
Norman, Oklahoma
2017

COMPARISON OF SURFACE AND DOWNHOLE MICROSEISMIC ACQUISITION

A THESIS APPROVED FOR THE
CONOCOPHILLIPS SCHOOL OF GEOLOGY AND GEOPHYSICS

BY

_____
Dr. Kurt Marfurt, Chair

_____
Dr. Jamie Rich

_____
Dr. Xiaowei Chen

Acknowledgements

I would like to thank Devon Energy for supporting my education and for providing data for this thesis. I would also like to thank my coworkers, classmates, friends, and family who have encouraged me throughout this long, yet illuminating journey in the quest for pursuing my Master's degree.

Table of Contents

List of Tables

List of Figures

Abstract

The most common microseismic monitoring methods used in the industry today are by the use of surface arrays and downhole arrays. In surface acquisition, sensors are deployed on the surface in large two-dimensional arrays, allowing this method to provide a greater accuracy in horizontal locations due to the wide aperture it can cover. In contrast, downhole acquisition places the sensors directly in the subsurface, allowing monitoring to be closer to the fracture events, therefore resulting in higher fidelity results.

To address these issues, a high quality microseismic dataset was acquired in the Anadarko Basin, Canadian County, Oklahoma, in January 2013, with its target formation being the Woodford Shale. The final microseismic event catalogues produced 1074 events from a surface array and 6450 events from a downhole array. Through proper alignment of the catalogues and correlation of events by time, 768 events were located by both acquisitions.

Upon analysis of the microseismic events, it was observed that those events recorded by the surface array were systematically shifted too deep compared to the events recorded by the downhole array. The surface events however did appear to be better constrained on lateral location as the events took on a linear pattern, aligned in their expected hydraulic fracture paths. In contrast, the downhole events were much more dispersed laterally. After thorough analysis, the highest quality interpretation was made based on co-identified events.

Because attenuation modifies the seismic velocity, I evaluated it as a possible factor in the difference between each mode of acquisition. The raw dataset of microseismic events were filtered, vector-rotated, and muted prior to Q estimation using a spectral ratio analysis.

The event location ambiguities and difficulties in Q estimation provide insight into the complexity of the downhole waveforms. The signals recorded from the later stages of the hydraulic fracture job were the most difficult signals for arrival time picking. This was due to the amount of noise in the signals from the superposition of head waves and late arrivals, as well as the inconsistency of source signatures among the signals. The Q values obtained from the earlier stages were reasonable, while those from later stages were non-physical, suggesting attenuation and scattering effects associated with irregular ray paths and for some events, propagation through a zone damaged by previous microseismic events.

Chapter 1: Introduction

In this study, microseismic events recorded by both surface and downhole acquisition of the same fracture job are analyzed and compared, resulting in an observation that different modes of acquisition can lead to dramatically different interpretations. This thesis focuses on the depth discrepancies observed between the two modes of acquisition and provides evidence that supports the depth values captured from the downhole array as the proper interpretation. For a surface array, identifying the event location in the vertical direction is less constrained due to the placement of the sensors being on the Earth's surface (Thornton and Duncan, 2012). This limitation causes a decreased signal strength due to the longer travel paths from perforation shot to surface, as well as increased noise at the surface, which can decrease the overall detectability of the array (Thornton and Duncan, 2012). The downhole dataset in this study places more confidence in the depth of event locations, which can have implications in future development and vertical well placement. Based on this knowledge, it can be determined whether it is necessary to drill another well in the same area based on how accurate structural drilling hazards can be imaged with microseismic data.

Although this thesis focuses on the advantages of a downhole array, it is important to recognize that the strengths and weaknesses of each method are in some sense complimentary, since downhole acquisition offers a better sensitivity on the vertical event location while surface acquisition offers a better sensitivity on the lateral event location (Thornton and Duncan, 2012). By combining these two methodologies, an optimal interpretational dataset is achieved in this thesis by applying the depth values from the downhole dataset with the horizontal values from the surface dataset.

Chapter 2: Geologic Setting

This study takes place in the Anadarko Basin of Western Oklahoma, Canadian County, just west of Oklahoma City (Figure 1).

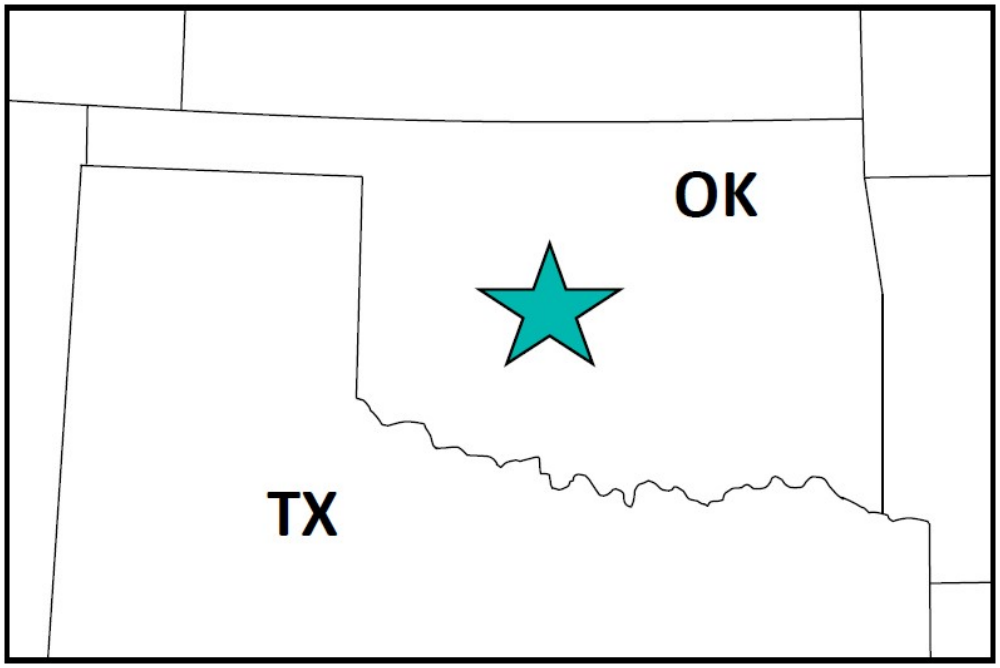

Figure 1. *The location of the dataset used in this study as indicated by the teal star.*

The Woodford Shale is a hydrocarbon-rich formation that was deposited in an epeiric sea during the Late Devonian-Early Mississippian (Verma et al., 2013) (Figure 2). Prior to the Woodford deposition, an erosional unconformity occurred where 500 – 1,000 ft of strata eroded away, leaving the Woodford and Misener Sandstone to rest on Ordovician and Silurian rocks (Johnson and Luza, 2008) (Figure 3). During much of the Devonian and Mississippian, most of Oklahoma was covered by shallow seas, where limestone and chert were the dominant sedimentary rocks in the area (Johnson and Luza, 2008).

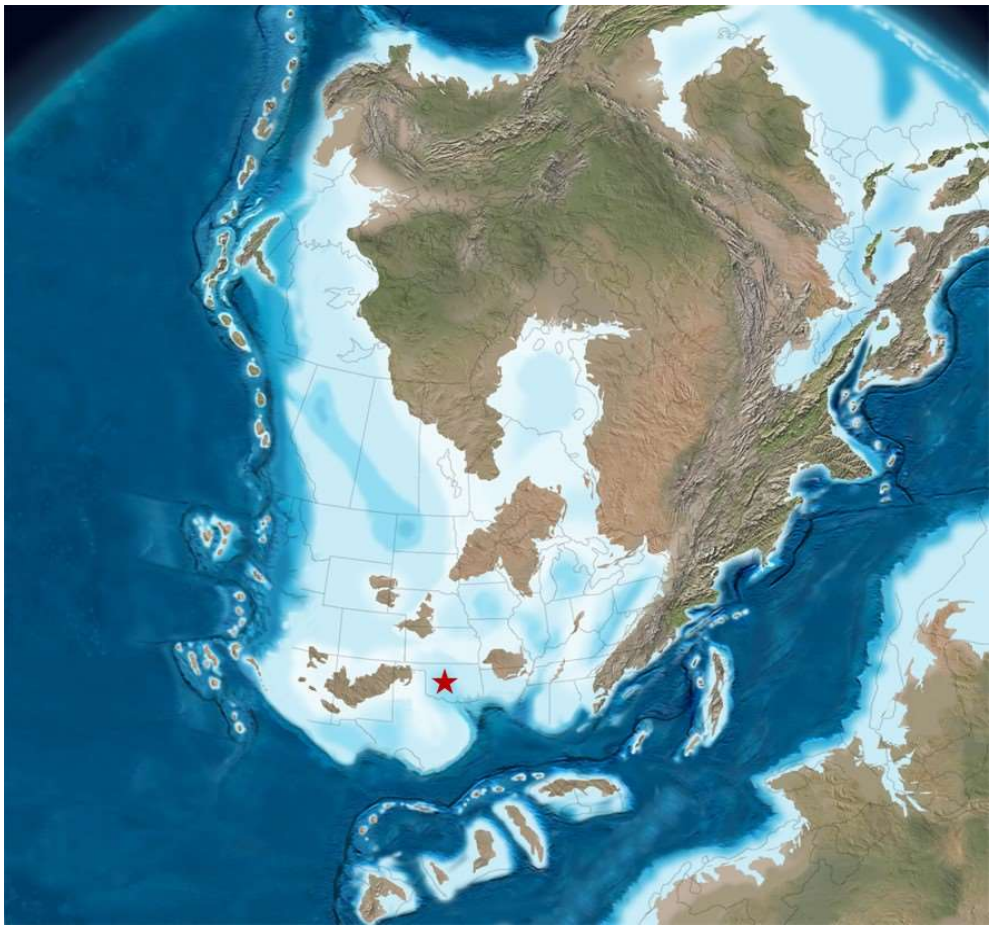

Figure 2. *Paleogeographic map of North America during the Late Devonian (360 Ma). The location of the dataset is indicated by the red star (Modified from Blakey, 2011).*

It was also during this time that marine upwelling played a part in the preservation of the high organic content in the Woodford, through wind-driven movement of nutrient-rich, dense, cooler water up towards the ocean surface (Kvale and Bynum, 2014). It was the presence of the Precambrian Nemaha Ridge (Figure 4) that prevented the upwelling of chert to be distributed across the Anadarko Basin during most of the Woodford deposition, resulting in more bioturbated intervals throughout the Woodford west of the Ridge (Kvale and Bynum, 2014).

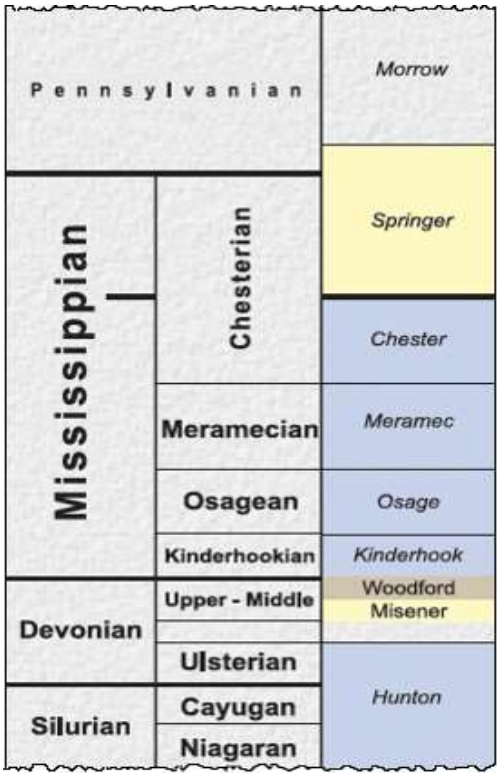

Figure 3. *Stratigraphic column showing the Devonian-aged Woodford formation. Below that is the Misener Sandstone and below that is a gap in the time, representing an erosional unconformity. Blue intervals represent carbonates, yellow is sandstone, and beige is shale (Modified from Boyd, 2008).*

In the last half of the Mississippian, basins in the southern part of Oklahoma subsided rapidly, resulting in thick deposits of shale, with intermingling of limestone and sandstone (Johnson and Luza, 2008). In the Pennsylvanian, an orogenic episode caused the Oklahoma Basin to break apart into a series of uplifts, forming the Arkoma and Anadarko Basins (Verma et al., 2013) (Figure 5).

The Woodford Shale now serves as a prominent source rock in Oklahoma and contains many fractures and subtle faults (Verma et al., 2013). Regional facies variations throughout the Woodford are seen through paleogeography, submarine sediment depositional systems, and upwelling currents (Kvale and Bynum, 2014).

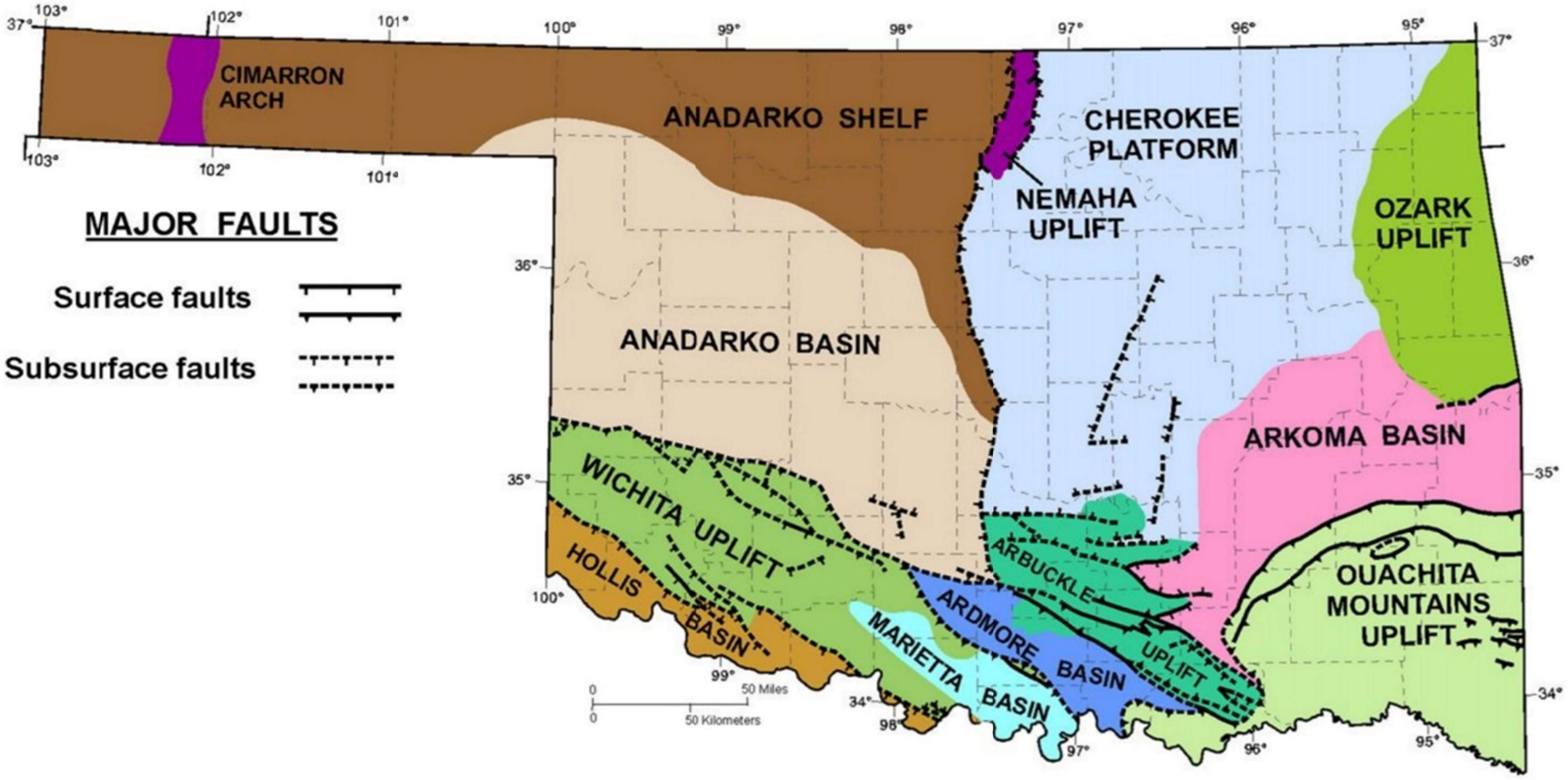

Figure 4. *Geologic provinces of Oklahoma. The Nemaha Uplift, or Ridge, is oriented north-south and splits the Anadarko Basin from the Arkoma Basin. The presence of the Nemaha Ridge is what prevented the upwelling of chert to be distributed across the Anadarko Basin during most of the Woodford deposition, resulting in more bioturbated intervals throughout the Woodford west of the Ridge (Modified from Cardott, 2012).*

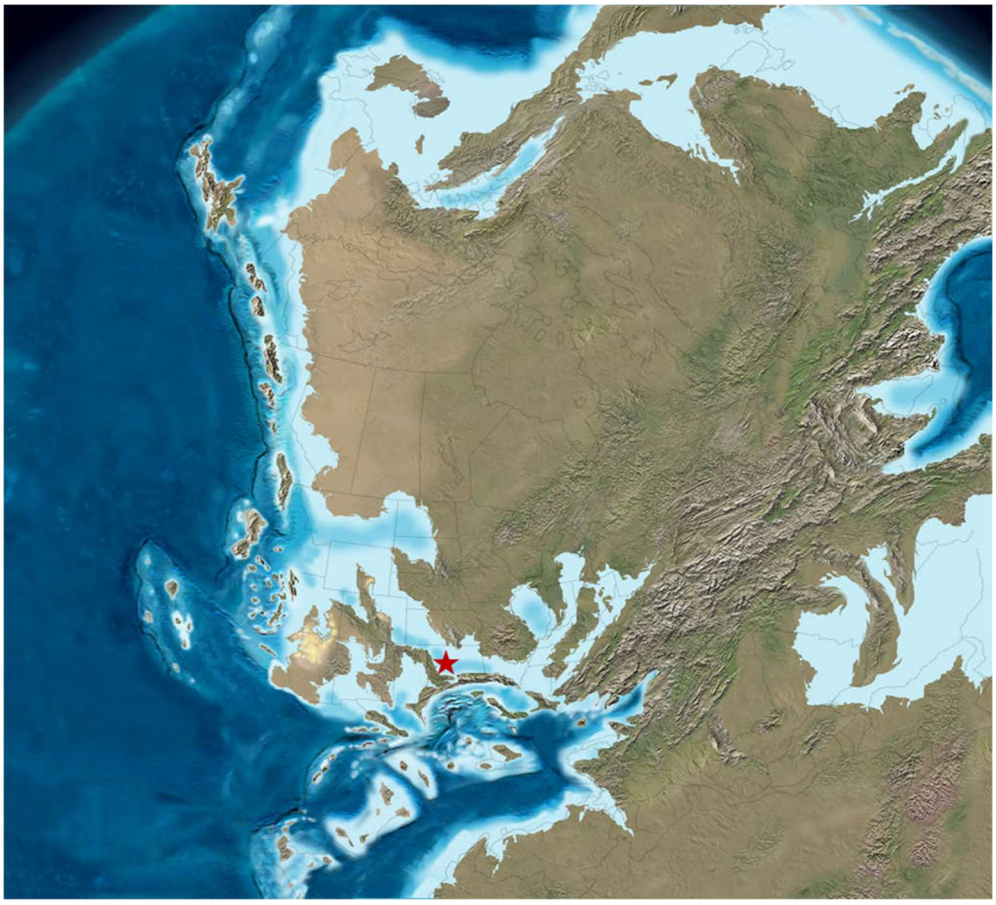

Figure 5. *Paleogeographic map of North America during the Early Pennsylvanian (315 Ma). The location of the dataset is indicated by the red star (Modified from Blakey, 2011).*

Chapter 3: Data Acquisition

Array Configuration

The microseismic dataset in this study was acquired with a surface array and a downhole array. The surface array consisted of a ten-arm radial array covering an area of 26 sq. mi., with the treatment well located at the center of the array (Figure 6).

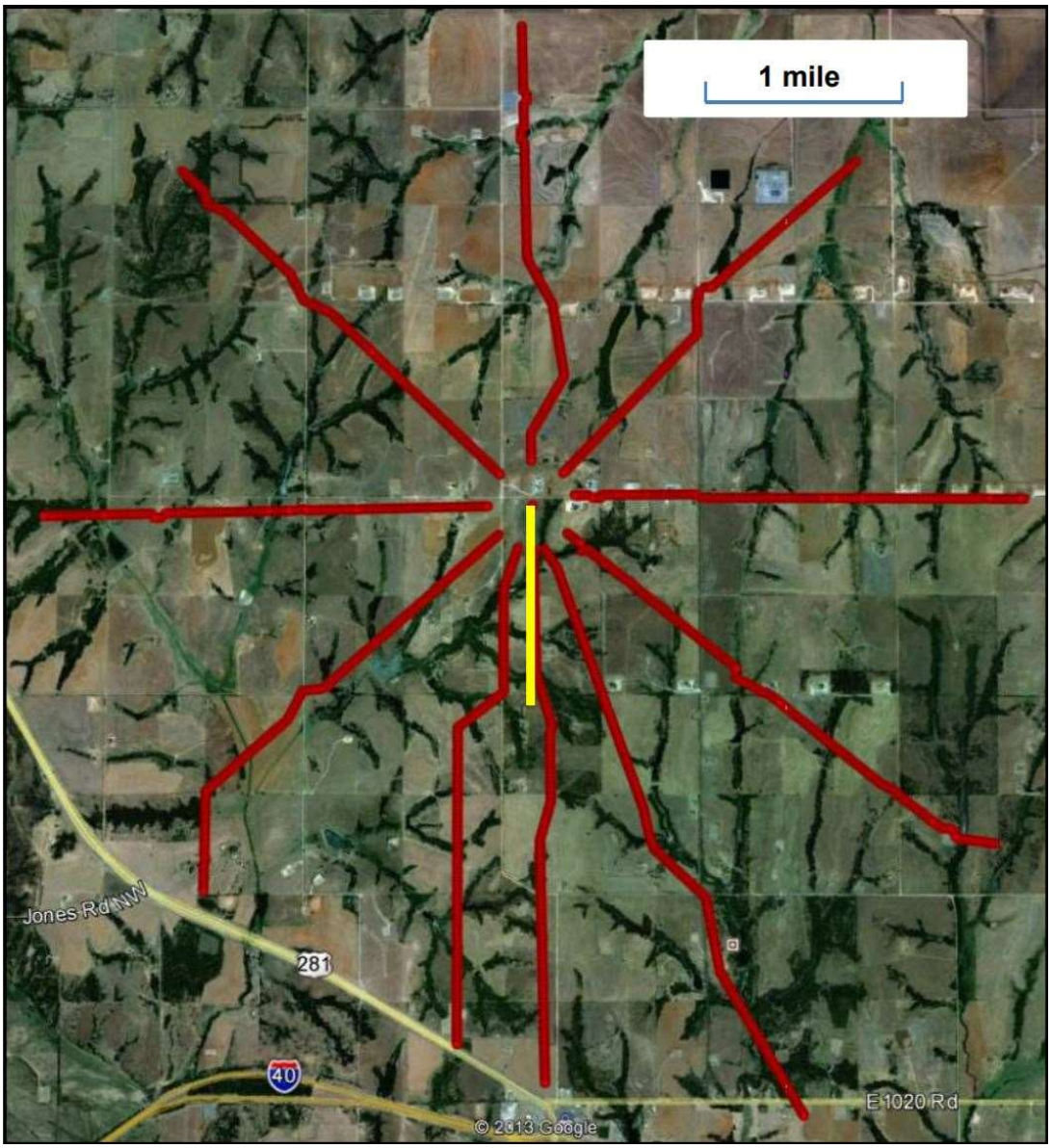

Figure 6. *Surface array configuration. The array consists of 10 arms radiating out from the wellhead. The treatment well is shown in yellow (Lowe et al., 2013).*

A total of 1,476 single vertical-component geophones were used, with spacing being 90 ft. Data were acquired at a 2 ms sample rate.

The downhole array consisted of only one monitor well, about 600 ft. east of the treatment well. Twelve 3-component sensors were placed in the downhole array, with spacing being 100 ft. Data were acquired at a 0.5 ms sample rate. The total length of the array is 1,100 ft, with the shallowest sensor at 9,500 ft. and the deepest sensor at 10,600 ft. (Figure 7).

The treatment well had a lateral length of 4,600 ft with a target depth of 11,400 ft subsea and was fracked using 12 stages via sliding sleeve completion design with one to four sleeves per stage. A sliding sleeve completion involves the use of pre-perforated sleeves along the lateral so that a perforating gun is not needed. A ball is pumped down in order to open and close the sleeves with perforations, causing an acoustic signal. The velocity model calibration was also taken via string shot prior to the completion of the well. The string shot is an explosive charge that is set off at the heel of the well, which is then imaged onto the arrays, allowing the velocity model to be calibrated at the heel only.

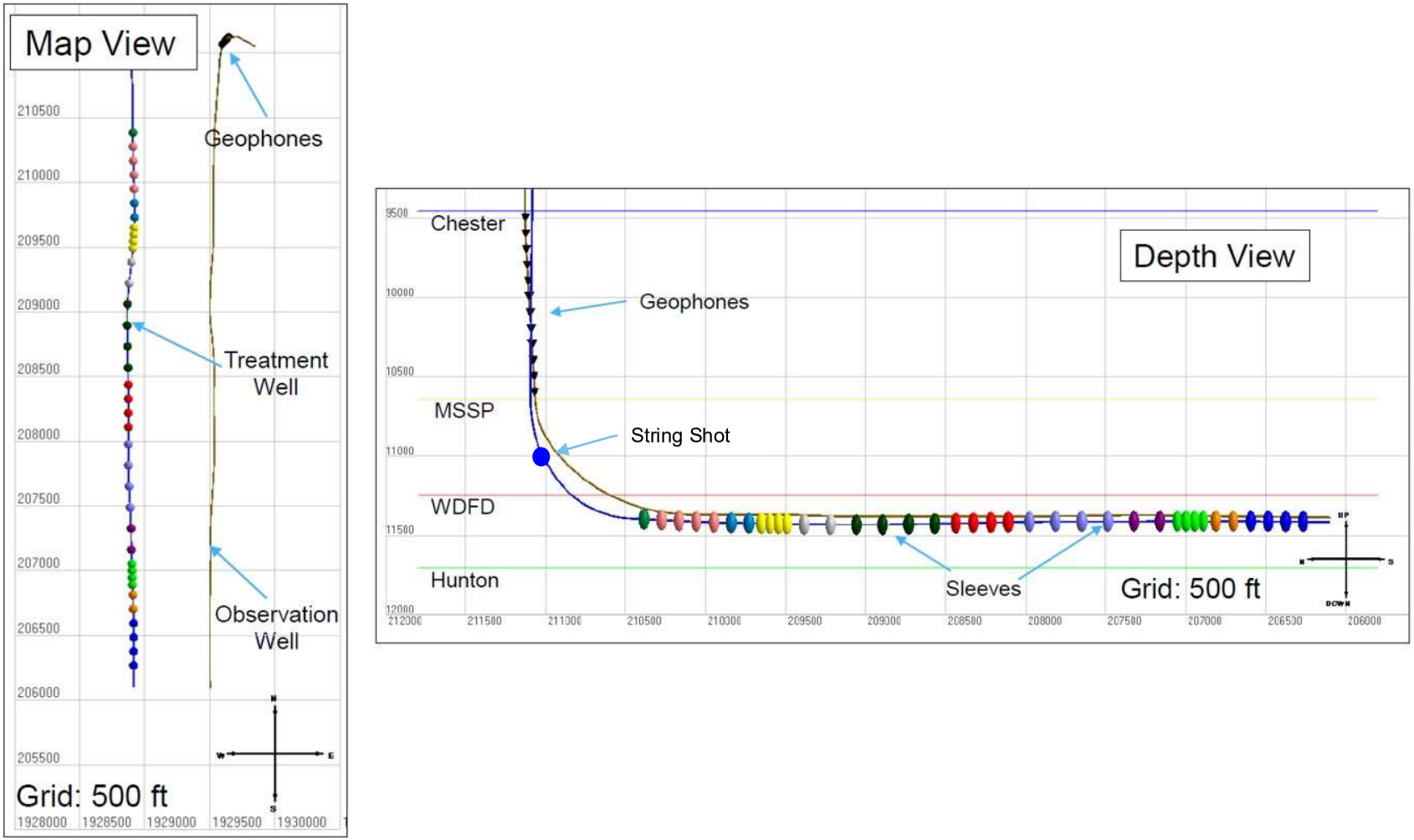

Figure 7. *Downhole array configuration. The array consists of one monitor well with twelve 3-component sensors, with spacing being 100 ft. The total length of the array is 1,100 ft., with the shallowest sensor at 9,500 ft and the deepest sensor at 10,600 ft. (Modified from IMaGE Final Report, 2015).*

Velocity Model

The initial velocity models for both arrays were constructed from the treatment well's dipole sonic log. Anisotropy was accounted for in both models. For the surface array, a VTI velocity model was produced (MicroSeismic, Inc. Final Report, 2013). For the downhole array, horizontal velocity was taken from the lateral sonic log and Thomsen parameters were estimated based on the relationship between the horizontal and vertical logs (IMaGE Final Report, 2015). The final calibration for the surface array's velocity model was performed using strong microseismic events across the wellbore and verified with the string shots. (MicroSeismic, Inc. Final Report, 2013). Calibration for the downhole array's velocity model was performed based on the identification of "control shots," which consists of events with a known location that can be used for sensor orientation/velocity calibration. (IMaGE Final Report, 2015). This includes triggered/flagged data, perforation shots, and sliding sleeve events. Of these control shots, the theoretical arrival times of P, Sh, and Sv are matched to the observed times to minimize the pick time residual. Early events from every stage were also picked to calibrate the velocity model, assuming that these events originated at the wellbore. The string shot produced at the heel of the well, however, was the only true known location (IMaGE Final Report, 2015).

Chapter 4: Correlation of Events

Initial Comparison of Arrays

The processed datasets from both the downhole and surface arrays were loaded into the Transform software for 3D visualization of all microseismic events captured, and to make any initial observations and comparisons between the two arrays. When observing the events in map view (Figure 8), notice how the surface events take on a more linear pattern, as opposed to the downhole events which look to be a bit more dispersed. This suggests the surface events provide a greater accuracy in horizontal location, as they are aligned along the fractures they originated from. The overall trend of the microseismic events is at an E – W orientation at roughly 84° (MicroSeismic, Inc. Final Report, 2013), which corresponds with the regional horizontal stress in western Oklahoma. This trend can also be seen in the downhole events, but it is not as obvious. When observing the events in a cross-section view, a dramatic difference in the interpretation of height growth is noted for each mode of acquisition (Figure 9). Both sets of events are originating within the Woodford where the well has landed. However, the surface events indicate fractures are extending into the Hunton, whereas the downhole events indicate that they are progressing up into the Mississippi Lime.

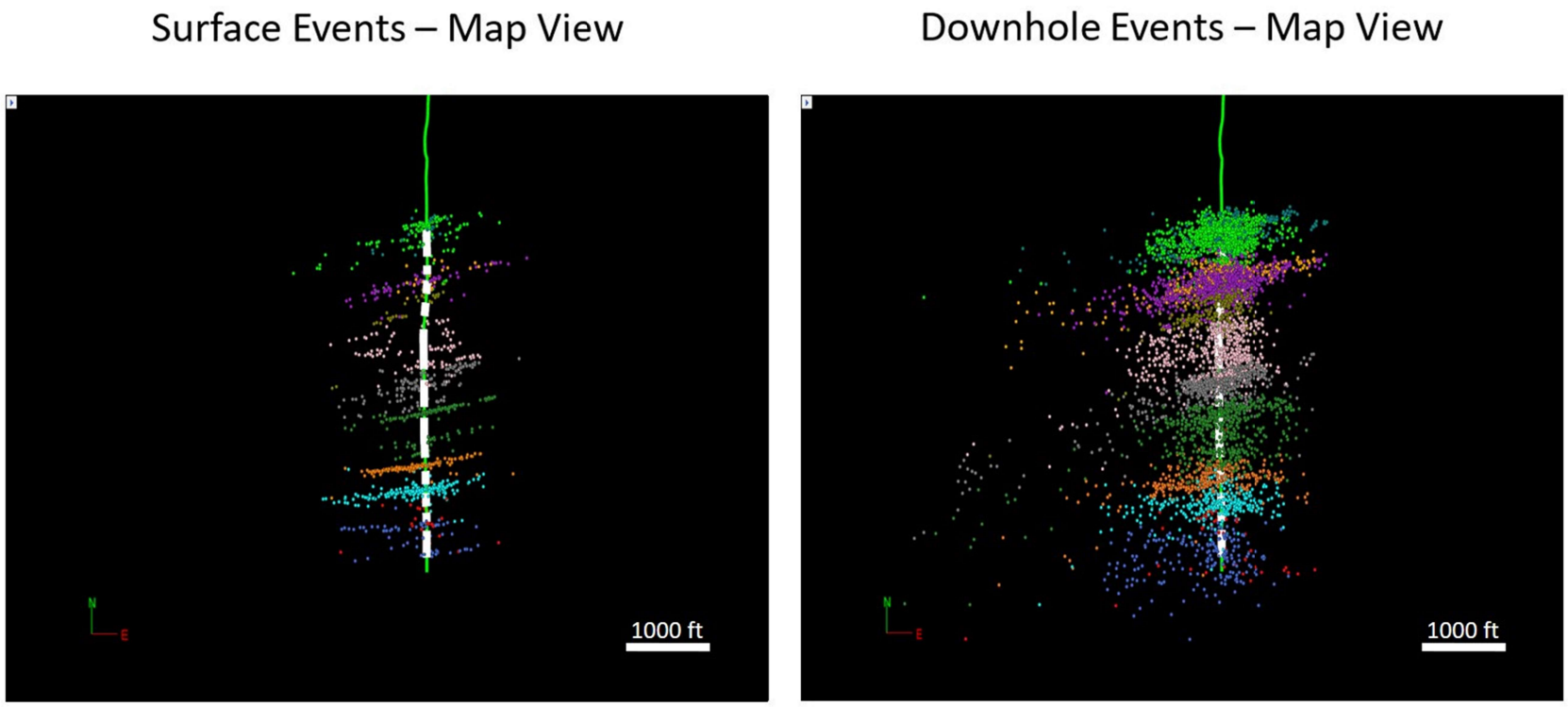

Figure 8. *A comparison of the events captured from the surface array, and events captured from the downhole array, in map view. Notice how the surface events take on a more linear pattern, as opposed to the downhole events which look to be a bit more dispersed.*

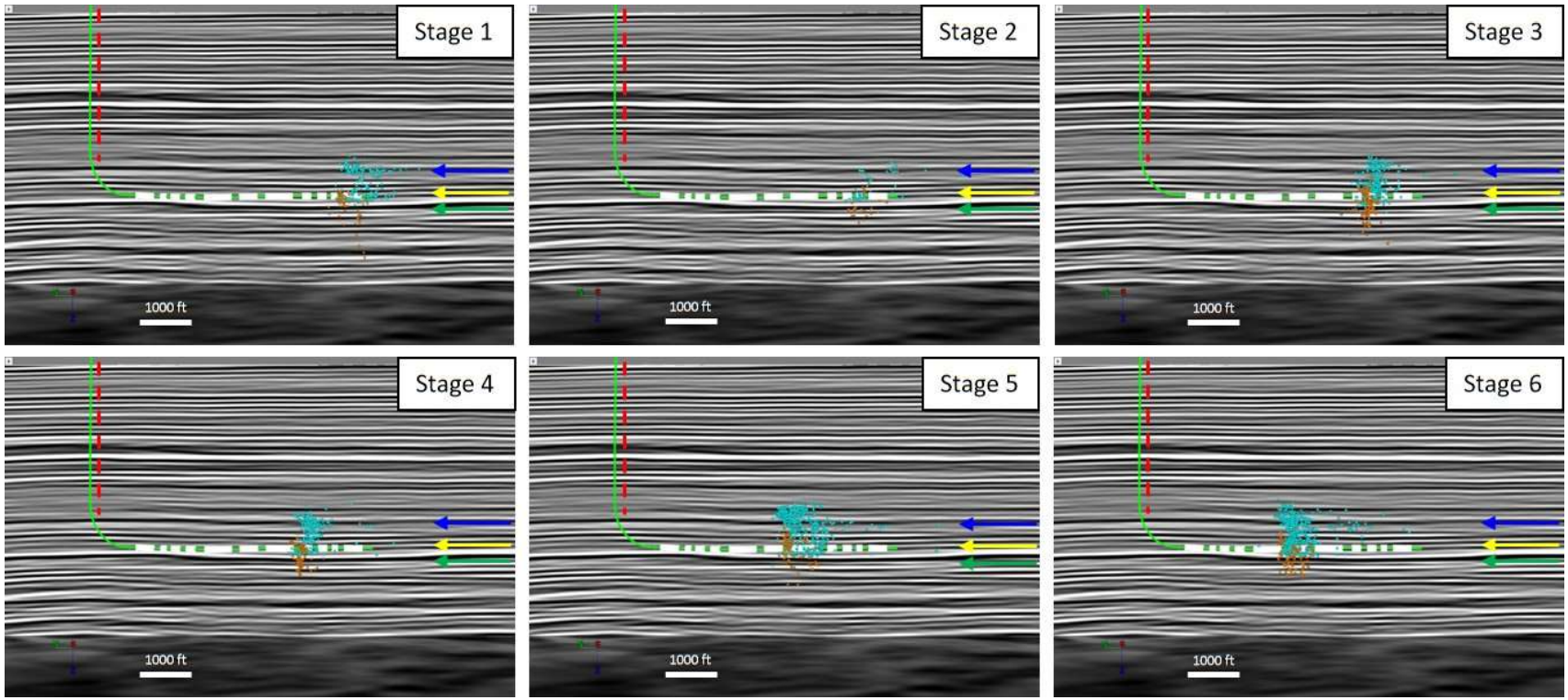

Figure 9. *Stages 1-12, one-by-one, in cross-section view. There is a dramatic interpretation in depth between the two methods of acquisition. Aqua events are those captured by the downhole array, and orange events are those captured by the surface array. The blue arrow represents the Lower Miss Top, yellow arrow represents the Woodford Top, and green arrow represents the Hunton Top. The red dotted line represents where the downhole geophones are located. The white blocks along the wellbore are the length of the frack stages.*

Stage 9
1000 ft
Stage 12
1000 ft
Stage 8
1000 ft
Stage 11
1000 ft
Stage 7
1000 ft
Stage 10
1000 ft

Synchronizing Event Catalogues

To further analyze these microseismic events, both surface and downhole event catalogues were correlated by event origin times. For each event in the surface catalogue, the nearest event in time from the downhole catalogue was considered. First, the catalogues needed to be synchronized by minimizing the difference in times between the origin times of the downhole events to that of their nearest surface event. In this case, the origin time of the surface catalogue was shifted -17.1 seconds to best align the catalogues (Rich et al., 2016).

Next, a 0.5 second time window was applied to both datasets, meaning that for every surface event that was within 0.5 seconds of a downhole event, they were considered the same event (Rich et al., 2016). A half-second was determined because of the observation that when a catalogue was correlated against itself, only about 1% of the events occur within 0.5 seconds of each other, meaning that the other 99% of events had a time difference between events of more than half a second (Rich et al., 2016). The idea was to make this time window big enough so that timing differences that still exist between the catalogues can be accounted for, and yet keep the window just small enough so that events that are different from each other are not being cross-identified. Based on this methodology, 781 events were co-identified out of 1074 events from the surface catalogue, and 6450 events from the downhole catalogue. It was later discovered that out of the co-identified catalogue of events, 13 of the surface events were duplicated. This can be explained by the fact that when the downhole catalogue was being correlated against the surface catalogue, there were 13 times when a downhole event matched up with the same surface event twice, and in one case, three

times. Due to this observation, those 13 duplicates and corresponding downhole events were not considered into this research, therefore resulting in a final total of 768 co-identified events. Figure 10 shows a comparison of all recorded events to all co-identified events. The filtering of events can be clearly seen here.

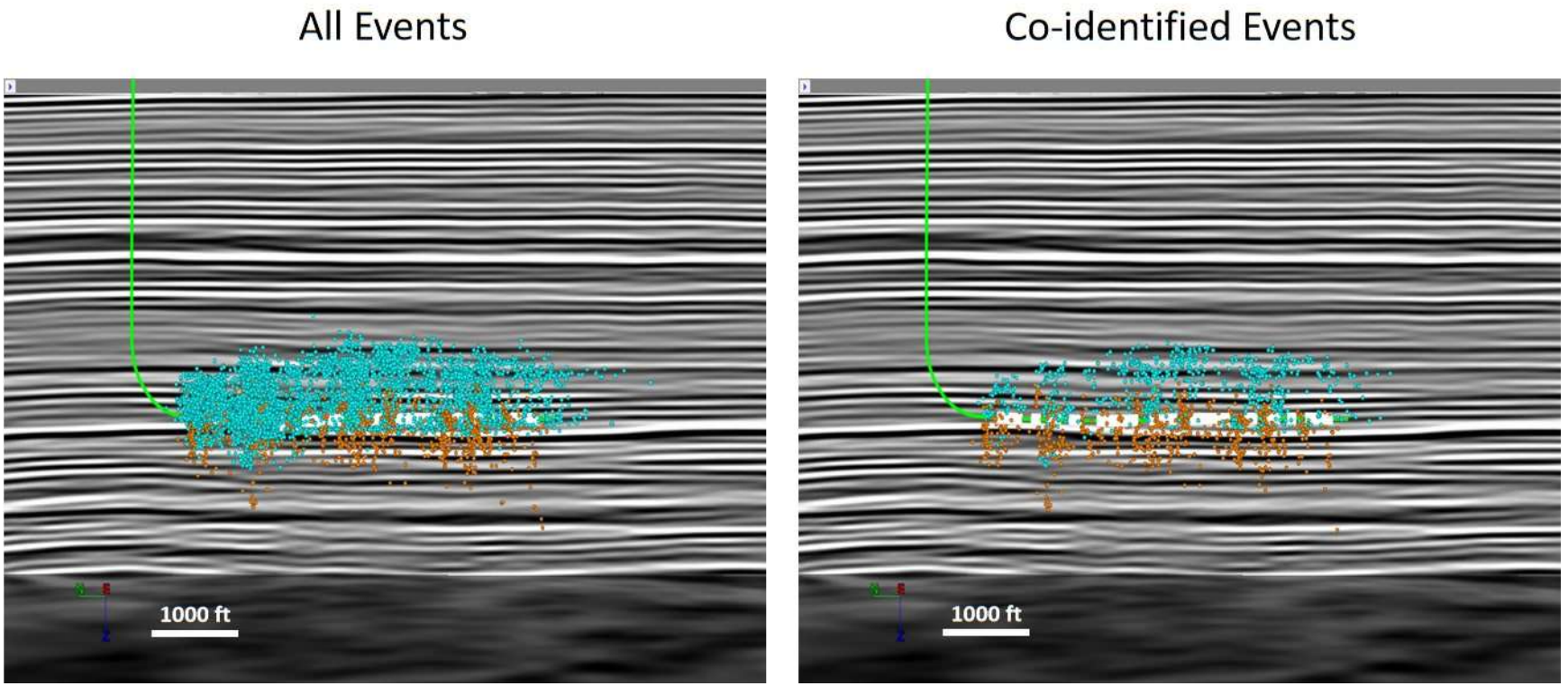

Figure 10. *A comparison of all recorded events to all co-identified events. Aqua events are those captured by the downhole array, and orange events are those captured by the surface array.*

Location Comparison

When the co-identified events were compared, their horizontal location differences average 100 ft, but the depth differences averaged at about 400 ft (Figure 11), resulting in significant interpretational differences (Rich et al., 2016). The azimuthal differences relative to the monitor well reveal an average of 1.8 degrees, which indicates a high degree of precision (Rich et al., 2016). This would be about the level that one would expect from hodogram analyses (Maxwell, 2009).

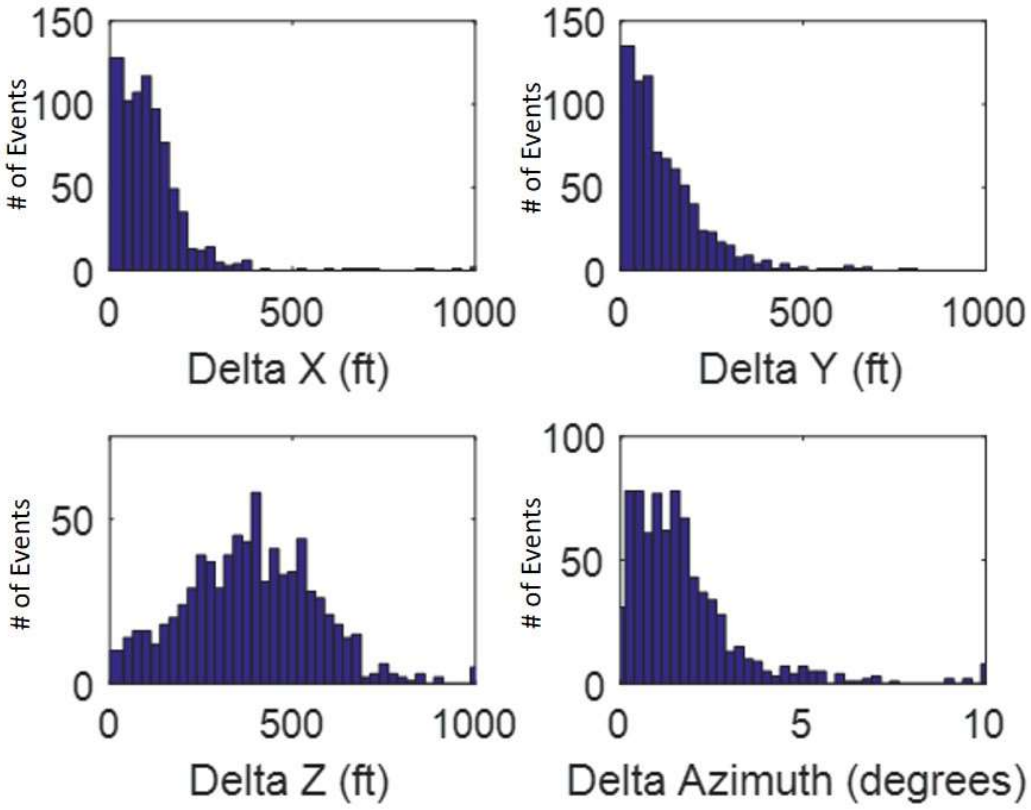

Figure 11. *Histograms of location differences for co-identified events. The mean difference in both X and Y locations was approximately 100 ft. while the mean difference in depth was 400 ft. The azimuthal differences relative to the monitor well reveal an average of 1.8 degrees (Rich et al., 2016).*

The hodogram analysis measures particle motion at the sensor array and determines the azimuth of the event (Kidney et al., 2010). Hodograms that detect a more consistent particle motion between sensors leads to more accurate azimuth determinations (Kidney et al., 2010). An example of a P-wave hodogram can be seen in Figure 12. A line of best-fit is placed on the hodogram that approximates the particle motion and is what defines the P-wave polarization vector (Grechka et al., 2011). Wherever on the hodogram that the line deviates from the particle motion is a measure of the polarization uncertainty (Grechka et al., 2011).

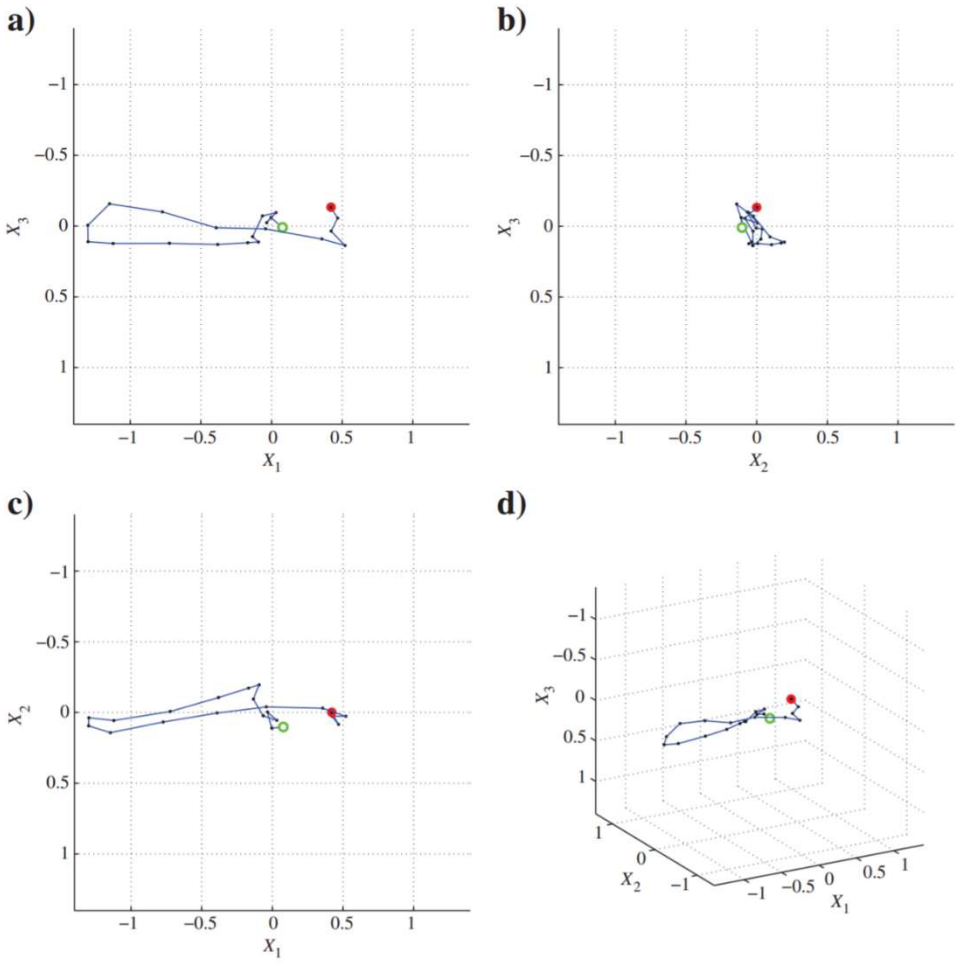

Figure 12. *Example of a P-wave hodogram analysis observed at four different angles. The open green circle marks the start of particle motion and the red solid circle marks the end of it (Grechka et al., 2011).*

Any kind of uncertainty in the event azimuth can be shown through error bars (Figure 13), with the uncertainty being unique to each event (Kidney et al., 2010).

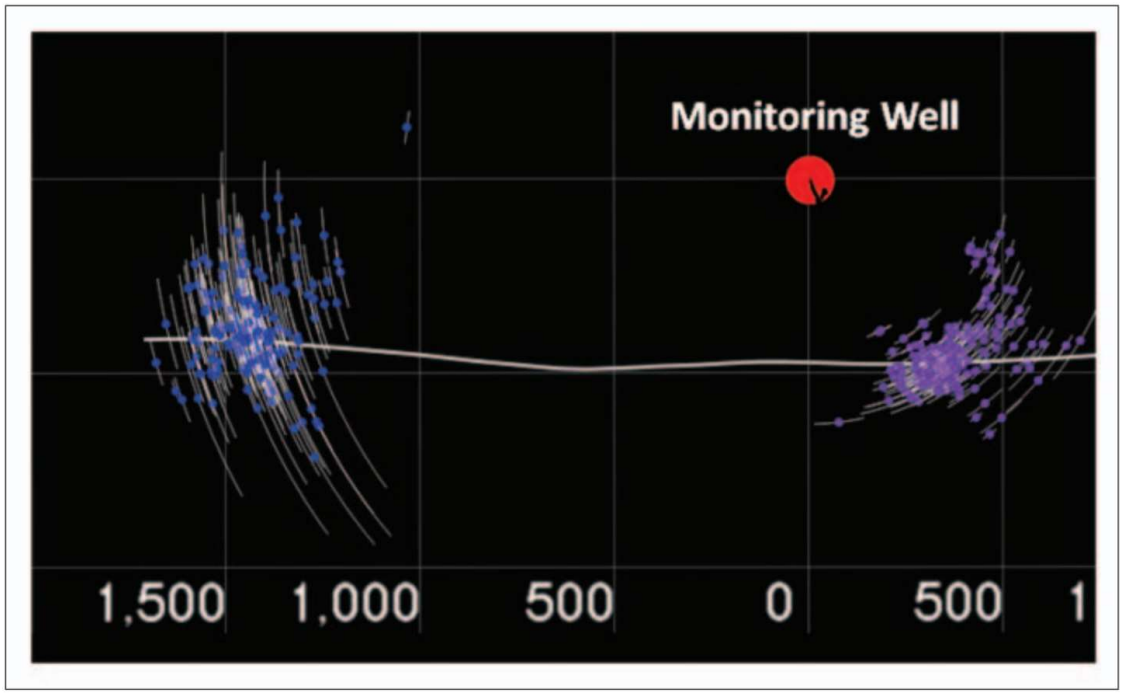

Figure 13. *Example in Map view of a horizontal well with a nearby monitor well and azimuthal error bars for two stages. There are smaller error bars in the stage closest to the monitor well, indicating a detection bias. Grid dimensions in feet (Kidney et al., 2010).*

Figure 14 displays histograms of horizontal and depth locations. Figures 14a and 14b show that the horizontal locations relative to the monitor well are similar in comparison. Figure 14c however reveals a dramatic difference in the interpretation of height growth (Rich et al., 2016). The black vertical line represents the top of the Woodford. This reinforces what was shown earlier in the cross-section views, showing depth discrepancies between the surface and downhole events. The events from the surface array are relatively constrained within the Woodford, whereas the events from the downhole array travel through the top of the Woodford. Also, there appears to be a bimodal distribution within the downhole set of events for Figure 14c, as indicated by the two dashed ovals. There is a good portion that looks to be constrained within the

Woodford, but there is a separate distribution above the Woodford as well. One hypothesis that could explain this is a possible fault plane located between the two distributions, allowing an establishment of a fluid flow pathway. As the fault was being activated, energy was absorbed and diverted into more fractures, developing a second distribution of events above the first. A similar effect was observed by Kratz et al. 2013).

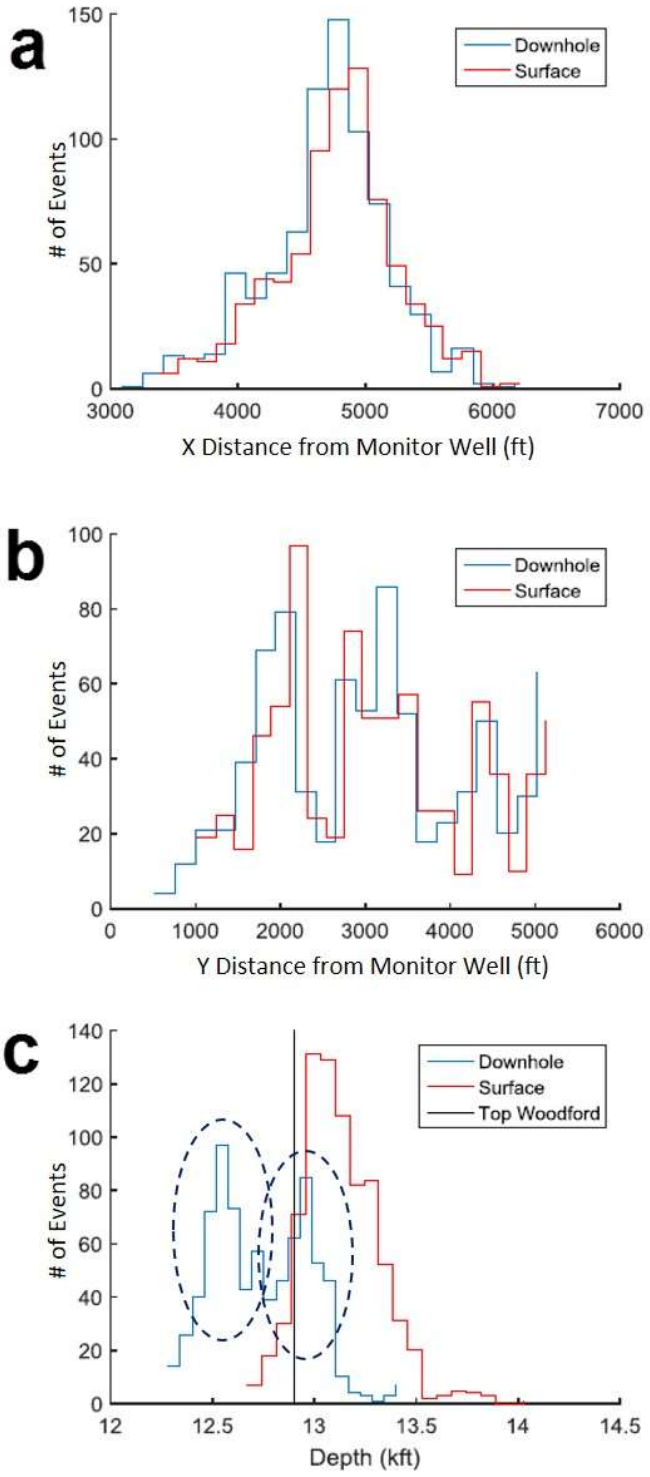

Figure 14. *Histogram of differences in event location for co-identified events. Figures a and b show the similarity in horizontal locations relative to the monitor well. Figure c displays the difference in interpretation of height growth, along with a bimodal distribution as indicated by the two dashed ovals. (Modified from Rich et al., 2016).*

Chapter 5: Identifying Fault Activation

Evidence from a Pressure Curve

An R-T plot for stages 4, 5, and 6 is shown in Figure 15. The R-T plot defines the radial distance from each perforation (y-axis) against the elapsed time (x-axis). The green arrow is pointing to a suspected fault activation during stage 4 that can be seen from the steep move-out of events. Further implications of the height differences can be seen by examining the location of the fault activation, because the surface events seem to be placing the fault at the wellbore, whereas the downhole events are placing the fault above the wellbore, in the shallower Mississippian section. The bright green curve represents the pressure treatment curve. There looks to be no change or drop in the treating pressure upon activation of the fault, indicating that the fault is not directly connected to the wellbore, supporting the downhole events as the proper interpretation. To further support the evidence of the fault not being at the wellbore is that there was no indication of a fault on the open-hole image log, and based on the geosteering interpretation, no fault was observed while drilling.

Another thing to point out are the single downhole and surface events located at the origin of the graph at stage 4 (Figure 15). As mentioned before, the treatment well was fracked using a sliding sleeve completion, and these two events more than likely represent the ball drop associated with this stage. The downhole event is placed right at r=0, meaning that it occurred at the wellbore, whereas the surface event is placed about r=300, meaning that it has been placed about 300 ft below the wellbore. This suggests that all the other surface events are being imaged too deep as well.

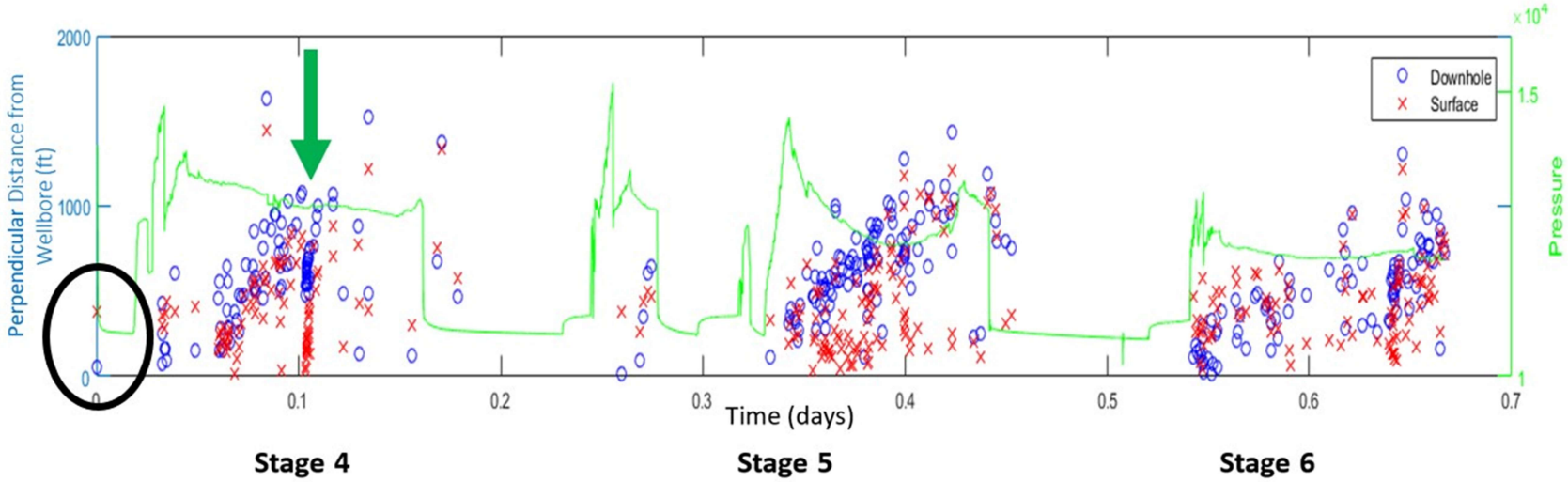

Figure 15. *R-T plot for stages 4, 5, and 6. The green arrow is pointing to a suspected fault activation during stage 4, as shown by the steep move-out of events. The bright green curve represents the pressure treatment curve. There looks to be no change or drop in the treating pressure upon activation of the fault, indicating that the fault is not directly connected to the wellbore, supporting the downhole events as the proper interpretation. Another thing to point out are the single downhole and surface events located at the origin of the graph at stage 4. Being that the treatment well was fracked using a sliding sleeve completion, these two events more than likely represent the ball drop associated with this stage (Modified from Rich et al., 2016).*

A closer look at stage 4, based on an image captured from the final report (Figure 16), shows the pressure treatment curve in red plotted against the histogram of seismic events in time. The bar showing the largest number of events indicates where the fault activation is, and as the treatment curve passes through, there is no indication of a change or drop in pressure, further reinforcing this fact.

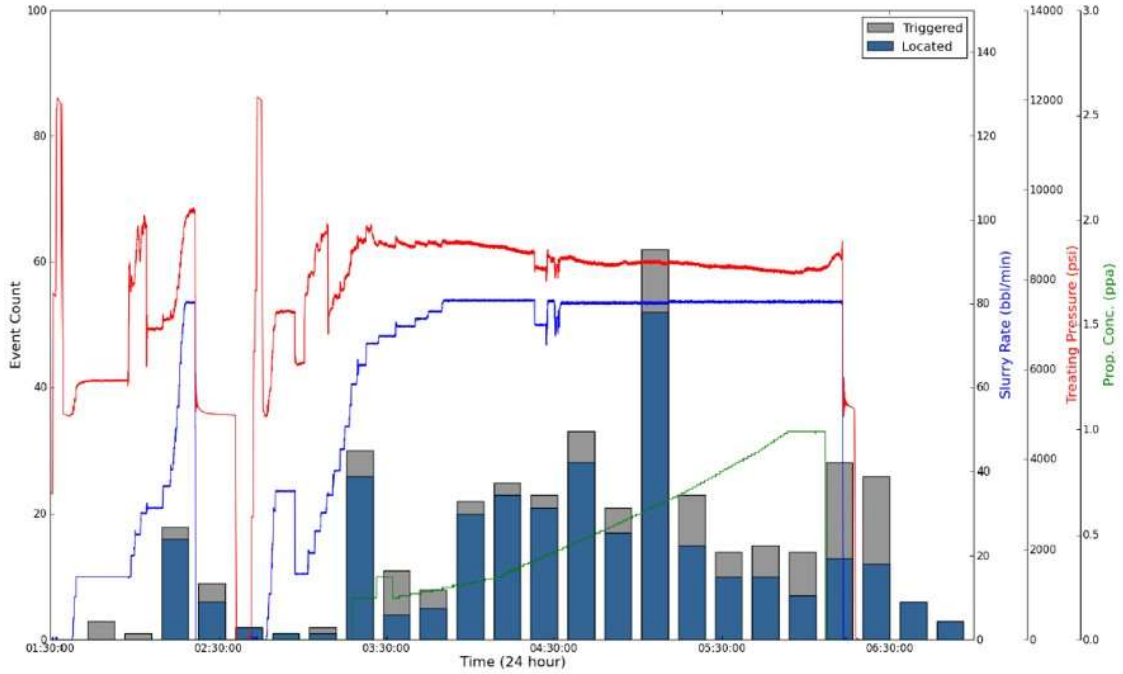

Figure 16. *Image captured from the final report showing stage 4 only. The pressure treatment curve is plotted in red against the histogram of the seismic events in time. The largest bar indicates where the fault activation is, and the treatment curve passing through this spot does not show indication of a change or drop in treating pressure (IMaGE Final Report, 2015).*

Now we will take a closer look at stage 4, which we saw previously in the R-T plot, showing isolated events from the fault activation (Figure 17). The downhole events are represented by blue circles and the surface events are represented by red circles. Taking this into consideration, an ideal microseismic representation is shown by the yellow circles, combining the downhole depths with the surface lateral locations.

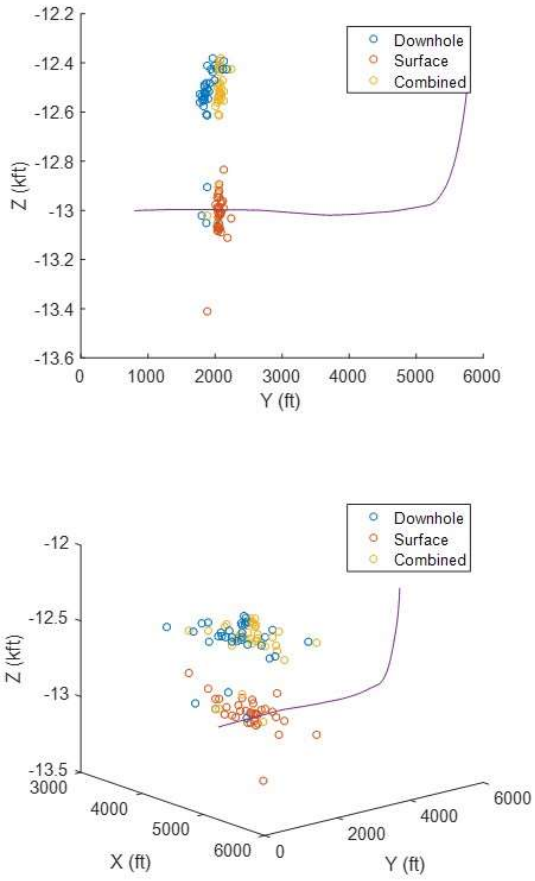

Figure 17. *Plots showing the isolated events from stage 4 that image the fault activation. An ideal microseismic interpretation combines depth locations from the downhole data and horizontal locations from the surface data (Rich et al., 2016).*

Figure 18 shows a comparison of events in cross-section and in map view. The first image shows all recorded downhole (aqua) and surface (orange) events, the second image shows all co-identified surface and downhole events, and the third image uses the idea from Figure 17, where an ideal representation of the microseismic events are plotted. The depth locations in this dataset are taken from the downhole data and the horizontal locations are taken from the surface data.

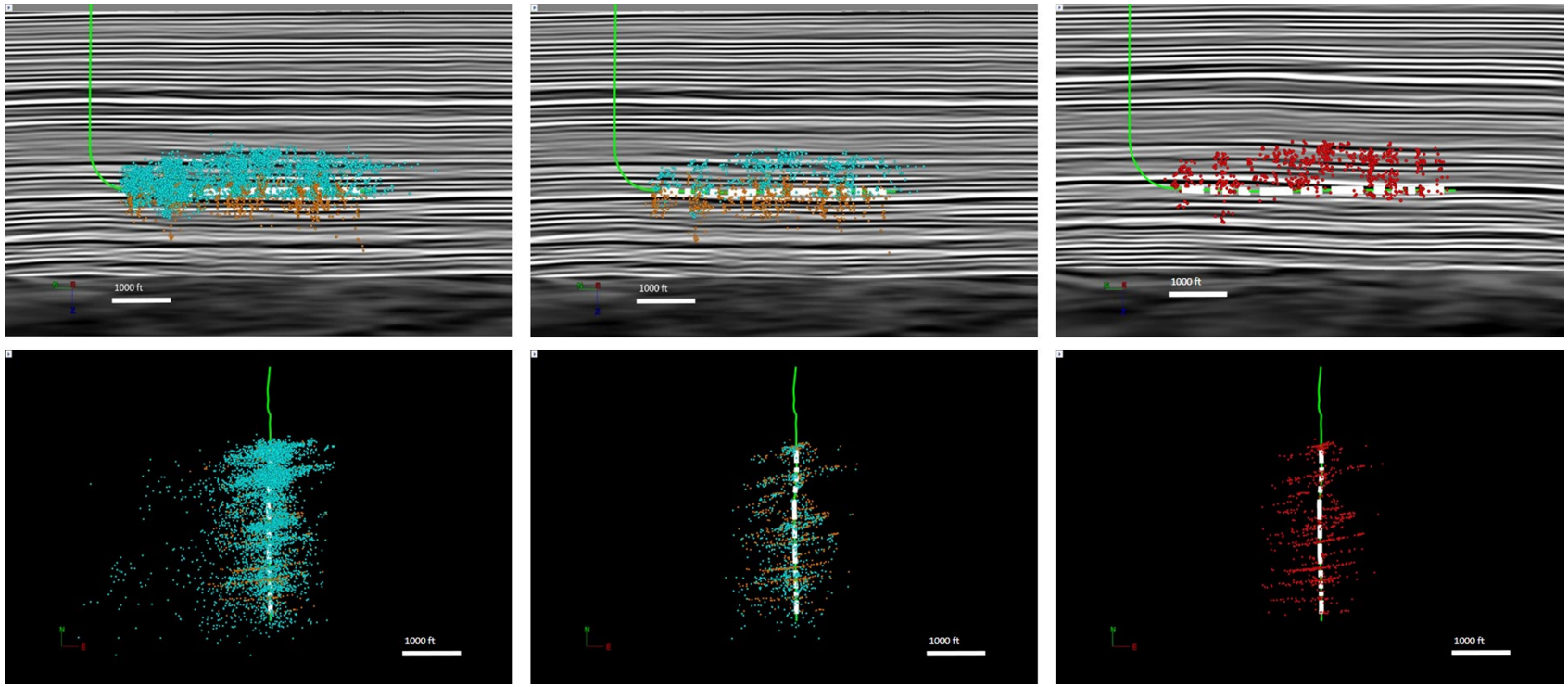

Figure 18. *Comparison of events in cross-section (top) and map view (bottom). The first image shows all recorded downhole (aqua) and surface (orange) events, the second image shows all co-identified surface and downhole events, and the third image combines the depth locations from the downhole data and the horizontal locations from the surface data.*

Event Magnitude vs. Distance

In the case where subsurface data may not prove to be adequate for fault detection or even in the absence of certain subsurface data, magnitude vs. distance plots can be useful in microseismic interpretation (Cabarcas and Davogustto, 2013). Event magnitude vs. distance plots show the relationship between the relative magnitude of seismic events and their distances from the monitor well.

Figure 19 shows two magnitude vs. distance plots comparing the surface events with the downhole events. For the surface catalogue, the magnitude was not reported by the vendor, instead, the amplitude was. Therefore, the log of the amplitudes was calculated to determine a representation of the surface magnitudes. Figure 19a shows all the events and reveals that most events only seen from the downhole array are below the minimum magnitude of observation from the surface. The smallest events downhole are only located when they're close to the monitor well, indicating a detection bias.

When looking at the co-identified event plot, Figure 19b, you no longer see a monitor well bias because the smallest event seen on the surface is at about -1.2M, which is also approximately the magnitude of completeness, *Mc*, which is marked on the graphs (Rich et al., 2016). The magnitude of completeness is the smallest magnitude at which one can observe consistently throughout all captured microseismic events. It removes monitor well bias, giving you a better distribution. This means that the magnitudes seen at the farthest stage away from the monitor well are approximately equivalent to the smallest magnitude seen from the surface array. This also tells us that the events captured from the surface array display a fairly even distribution of magnitudes due to

all the geophones recording at approximately the same distance away from the treatment well. In most cases, it is preferred to not have a bias associated with the location of the sensors for interpretation purposes, and it is not uncommon to see those biased events even be discarded during the interpretation phase (Cabarcas and Davogustto, 2013). On the other hand, these biased events can be important for detailed analysis, given that they are the lowest magnitude events and in some cases contain most of the technical information regarding the hydraulic stimulation (Cabarcas and Davogustto, 2013). Not only do the smallest magnitude events tell us something but so do the highest magnitude events. On the magnitude vs. distance plot, you can indicate where the highest magnitude events are at the farthest distance. This combination defines the maximum detection distance, indicating the maximum distance that a monitor well can be placed. This is important for the placement of monitor wells in future treatment jobs (Cabarcas and Davogustto, 2013).

You can also see that the magnitude of completeness marks a "kick-off" where the downhole events start a downward sloping trend. This is explained by the monitor well bias, but this is also a noticeable characteristic that will be brought up again in the section titled, 'Gutenberg-Richter Law.' Also, it is important to point out that this plot is an indication that the downhole events were matched well with the surface events upon synchronization of the catalogues because most of the smallest magnitudes from the downhole array on the co-identified plot are filtered out, which should be the case considering they should not be detected by the surface array.

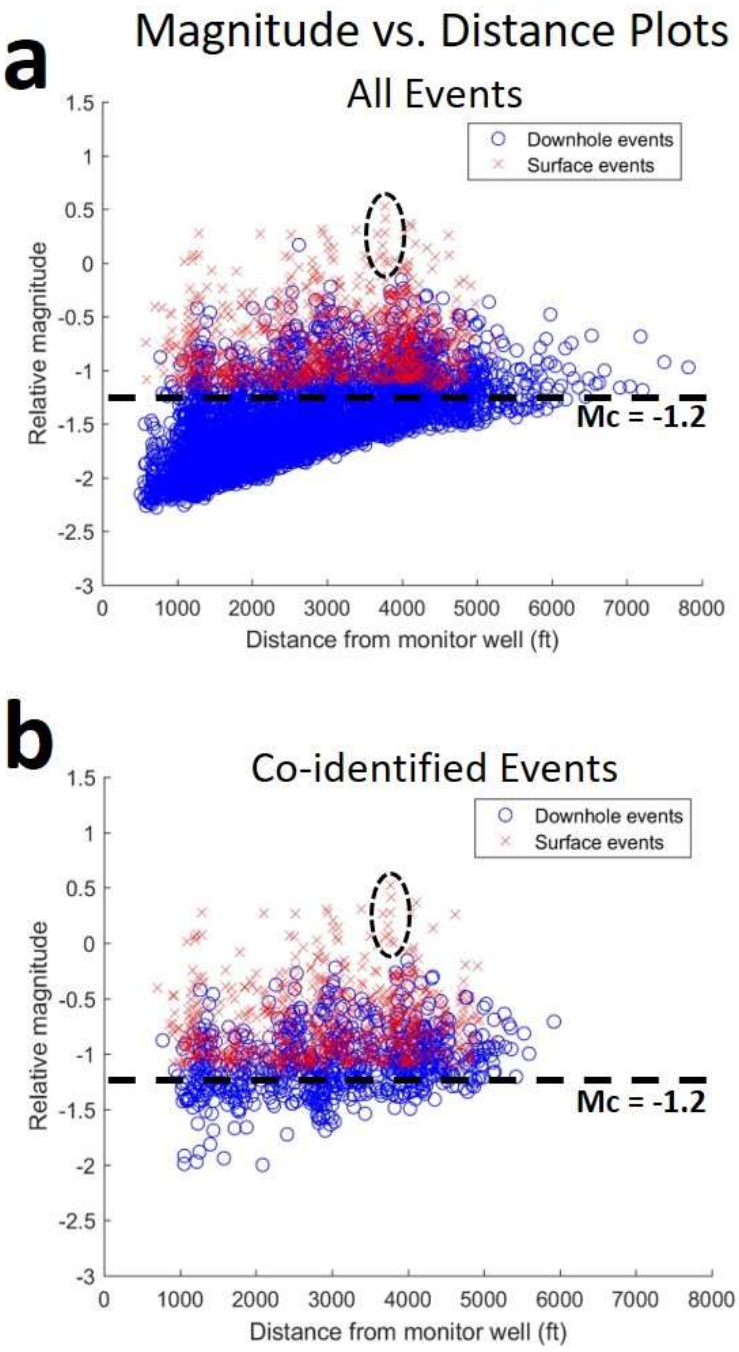

Figure 19. *Magnitude vs. Distance plots for all events (a) and co-identified events (b). The smallest events downhole are only located when they're close to the monitor well, indicating a detection bias as seen in figure a. The co-identified plot in figure b no longer shows a monitor well bias because the smallest event seen on the surface is at about -1.2M, which is also approximately the magnitude of completeness (Mc), where the distance from the events to the surface is nearly constant (Modified from Rich et al., 2016).*

These magnitude vs. distance plots can also provide some insight into fault reactivation. It is important to note that high-magnitude microseismic events are typically characteristic of reactivated faults (Cabarcas and Davogustto, 2013). As is well known in earthquake seismology, magnitude values are proportional to the size of the surface plane and the displacement involved in faulting (Aki and Richards, 2002), meaning the higher the magnitude, the larger the fault plane surface, and the higher the chances are for those magnitudes to characterize fault reactivation (Cabarcas and Davogustto, 2013). The presence of faults becomes noticeable on the magnitude vs. distance plots because the microseismic events associated with faulting have magnitudes that are distinctly higher (Cabarcas and Davogustto, 2013). An example of fault activation is shown by Cabarcas and Davogustto in Figure 20. It displays data from a multi-stage hydraulic treatment. The higher magnitudes are circled, representing those events associated with fault reactivation. In comparison with Figures 19a and 19b, notice the grouping of surface events that are circled. They follow a steeply-sloping trend which is reminiscent of the same events associated with the faulted events seen in stage 4. The top two events enclosed in the circle are indeed from stage 4, meaning these are the two largest events out of the entire surface and downhole catalogues. The largest event from the downhole catalogue of all events was observed in stage 6, however in the co-identified catalogue, the largest surface event co-identifies with the largest downhole event. This suggests that since the largest events were recorded in stage 4, a fault reactivation is possibly what occurred here.

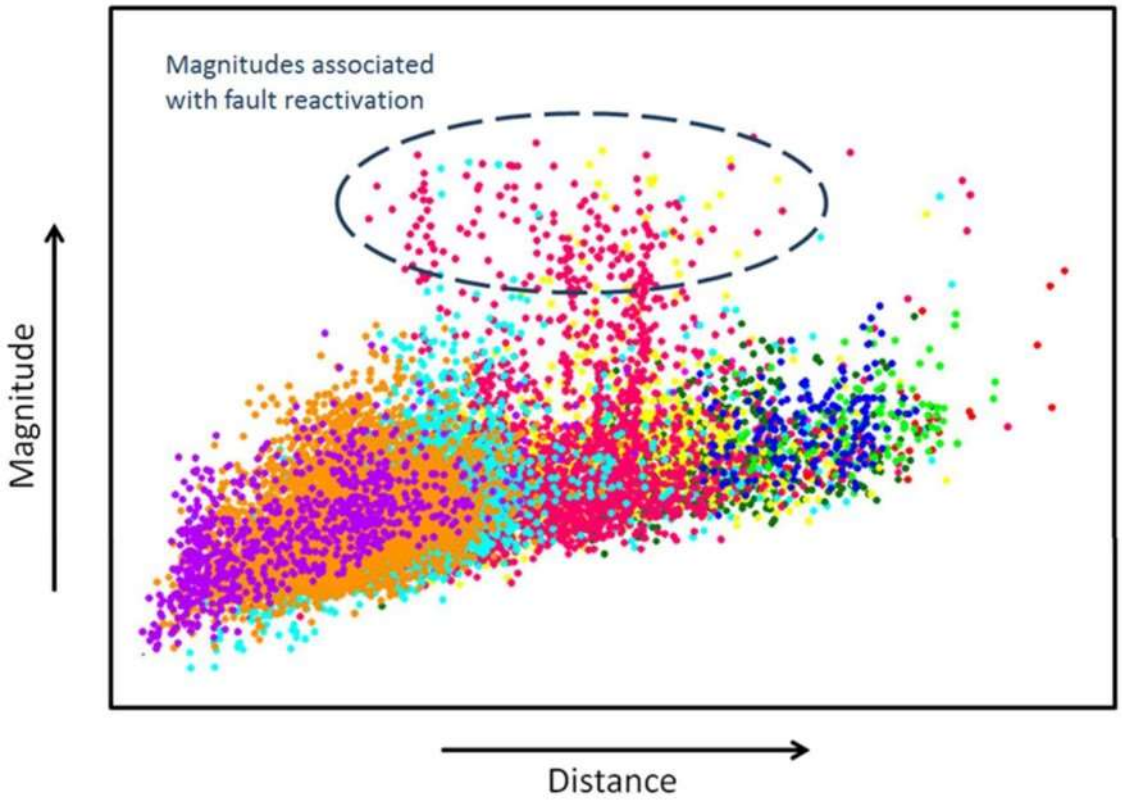

Figure 20. *An example magnitude vs. distance plot shows data from a multi-stage hydraulic treatment job and higher magnitudes are circled, representing those events associated with fault reactivation. (Cabarcas and Davogustto, 2013).*

Gutenberg-Richter Law

It is important to understand how hydraulic fracture treatments stimulate a reservoir, and if fault-related microseismicity is identified during a treatment (Kratz et al., 2013). This knowledge can be useful when identifying the best places to drill, as to avoid any identified fault features on nearby wells, which can lead to maximized production and reduced costs (Kratz et al., 2013).

Upon generation of a hydraulic fracture, the microseismic activity recorded during that time generally follows a power law distribution (Maxwell et al., 2009) described by the Gutenberg-Richter Law (1942), which defines the distribution of earthquakes relative to the magnitude:

$$\log N = a - bM \ , \tag{1}$$

where N is the number of earthquakes with magnitudes greater than or equal to a magnitude M and a and b are positive, real constants (Maxwell et al., 2009). The *b-value* describes the slope of the relationship where a value of 1 is typically observed with fault deformation and a value of closer to 2 is common with induced seismicity caused by hydraulic treatment (Kratz et al., 2013). Frequency magnitude distributions can help define certain geologic trends as well as source mechanisms within an area by the calculation of the *b-value*, which can confirm the difference between fault-related and hydraulic fracture-related events (Kratz et al., 2013). This earthquake-magnitude relationship exhibits a scale invariability due to earthquakes not being uniformly distributed in time, space, and magnitude (Kulhanek, 2005). The ratio of small- to large-magnitude events is what determines the slope. These ratios in magnitudes may

depend on the stress regime of that area, where the larger the shear stresses, the higher chance that the number of small events are equal to the number of large events. A smaller amount of shear stresses will display a higher number of small events to large events (Schorlemmer, 2005). This relationship is plotted as a frequency magnitude distribution ($\log_{10}(N)$ vs. Magnitude) (Bhattacharya, 2009). To make a proper b-value calculation for a certain catalogue of events, as a rule, the number of events used for analysis must reach a minimum of 50 events in length (Kratz et al., 2013).

Figure 21 shows four frequency magnitude plots. Figures 21a and 21b compare the downhole co-identified events to the surface co-identified events to observe what the overall trend is at a large scale. Then a closer look is taken at the stage where fault activation was observed in Figures 21c and 21d, which compare the downhole co-identified events to the surface co-identified events from stage 4 only. A trend line is fit along the downhill slope of every graph and their corresponding equations are written next to them. The slope of each linear equation is the *b-value* of that linear distribution. The magnitude of completeness, *Mc*, is marked on the downhole distributions. The surface distributions do not contain magnitudes that are smaller than the magnitude of completeness, so the *Mc* marker is not added to those graphs. The *b-values* were determined by measuring the slope above the magnitude of completeness for consistency.

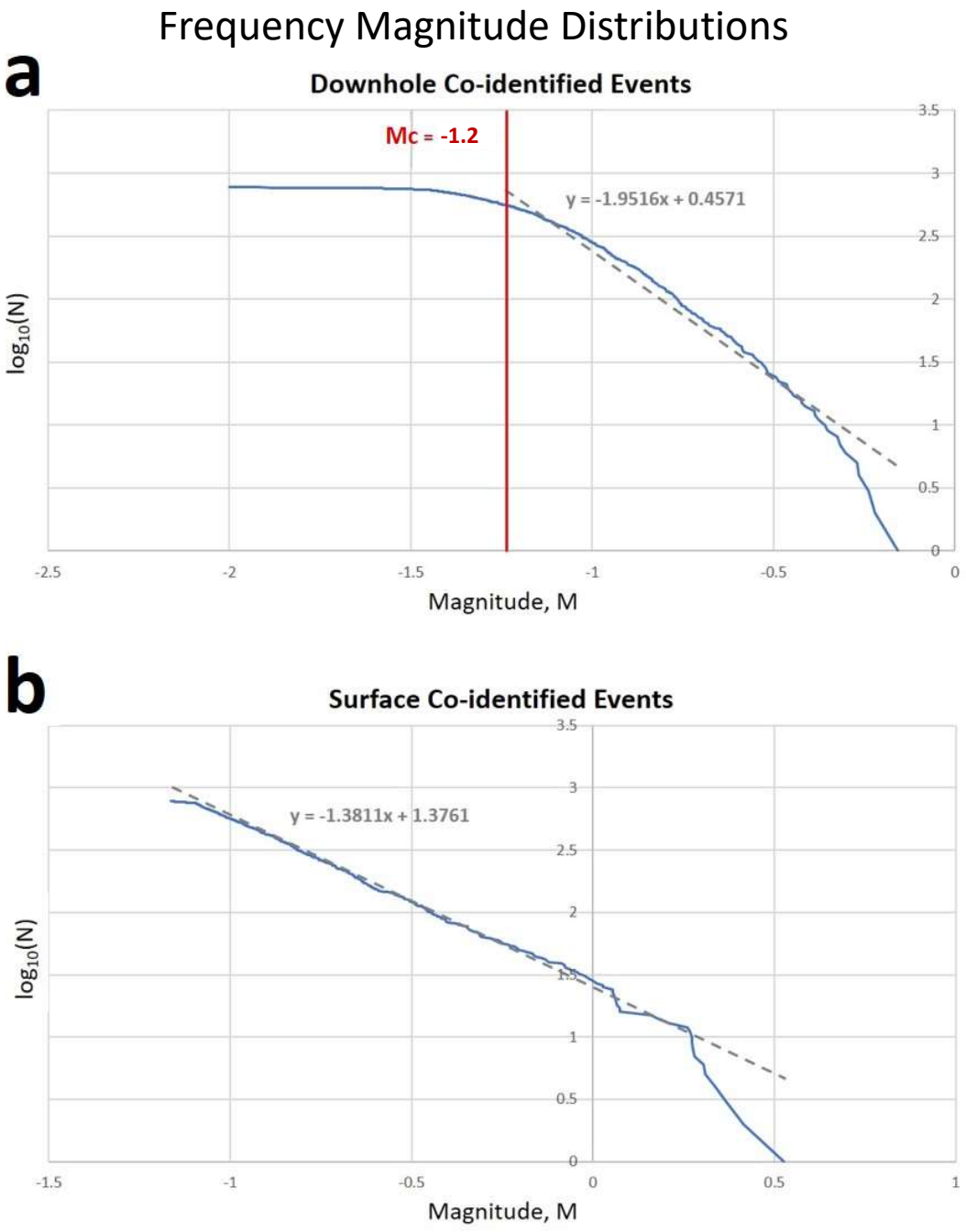

Figure 21. *Four frequency magnitude distributions where (a) and (b) compare the downhole co-identified events to the surface co-identified events and (c) and (d) compare the downhole co-identified events to the surface co-identified events from stage 4 only, the stage where the fault activation occurred. A trendline has been fitted along the downhill slope of every graph and their corresponding equations are written next to them. The slope of each linear equation is the b-value of that linear distribution. The magnitude of completeness, Mc, is marked on the downhole distributions only because the surface distributions do not contain magnitudes that are smaller than the magnitude of completeness.*

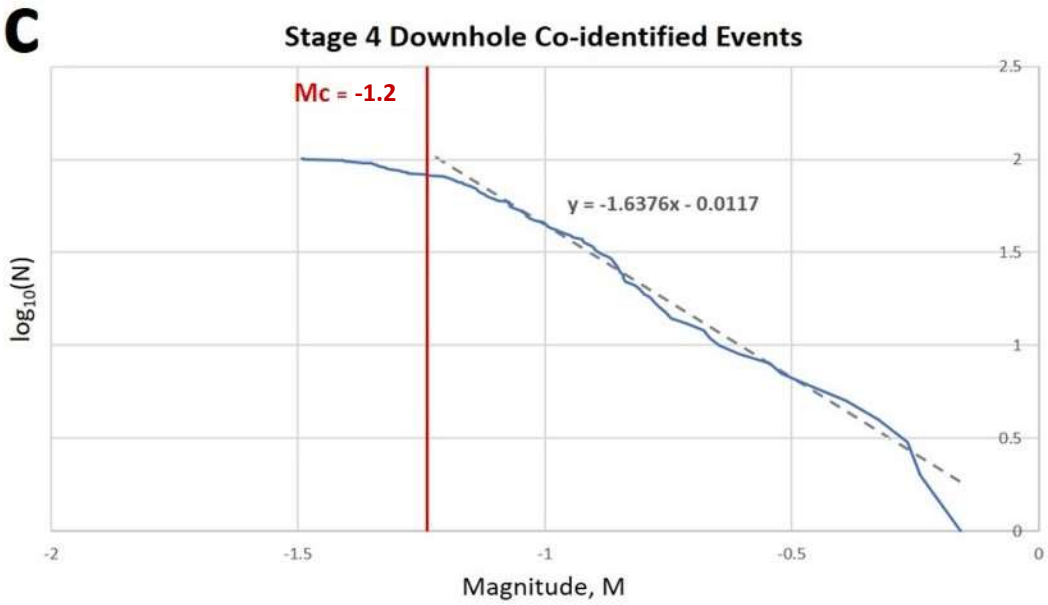
c
Stage 4 Downhole Co-identified Events
Mc = -1.2
y = -1.6376x - 0.0117
log10(N)
Magnitude, M
2.5
2
1.5
1
0.5
0
-2
-1.5
-1
-0.5
0

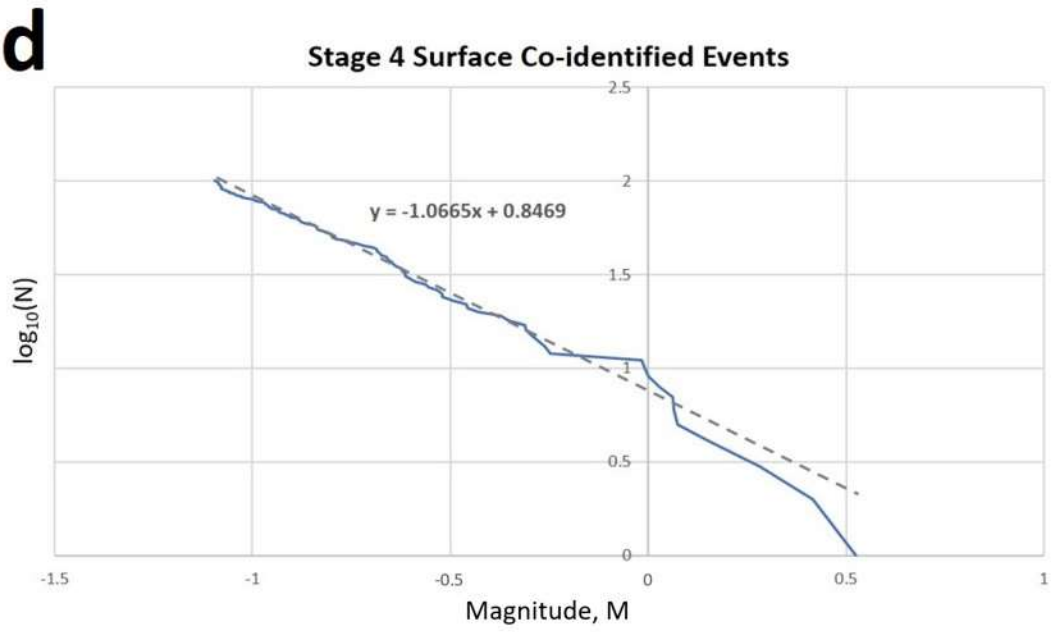
d
Stage 4 Surface Co-identified Events
y = -1.0665x + 0.8469
log10(N)
Magnitude, M
2.5
2
1.5
1
0.5
0
-1.5
-1
-0.5
0
0.5
1

There is a distinct characteristic shown by the distribution of downhole events which shows a flattening of the graph, or a "leveling off" of the number of events. This is described as a "roll-off" of the *b-value*, due to a drop-off in the number of low magnitude events (Bhattacharya, 2009). This drop-off in low magnitude events is due to detectability limits that stem from instrument sensitivity and signal-to-noise ratio. How soft or how harsh the "roll-off" is depends on monitor well bias. As a result of monitor well bias, the closer you approach the monitor well, the more likely you are to detect not only lower magnitude events but also more events in that vicinity rather than farther away from it (Cabarcas and Davogustto, 2013). The frequency magnitude distributions for the surface data on Figures 21b and 21d appear to not show a flattening of the graph, due to the amplitude threshold used to qualify events, which would eliminate all events below a certain cutoff.

When looking at these plots, all downhole co-identified events shown in Figure 21a have a *b-value* of about 2 and the stage 4 downhole co-identified events shown in Figure 21c have a *b-value* of about 1.6. All surface co-identified events in Figure 21b have a *b-value* of about 1.4 and the stage 4 surface co-identified events shown in Figure 21d have a *b-value* of about 1.1. Both plots from stage 4 have lower *b-values* than the plots showing all events, which is evidence that stage 4 is indicating higher potential of fault activation relative to the entire fracture job as a whole, as represented by Figures 21a and 21b, which is more typical of induced fractures. This further reinforces that the surface array is detecting more large events than small.

The frequency in small-magnitude events decreases rapidly at the magnitude of completeness, however recent studies in earthquake seismology suggest that the number

of small earthquakes as predicted by the *b-value* are really not as frequent as one would think, suggesting that the decrease in small-magnitude events may, to a certain extent, be real (Kulhanek, 2005). Notice on the frequency magnitude distributions that the downhole plots have a steeper slope than the surface plots. This attributes to the fact that the surface plots have a more complete catalogue of events. They do not have an overabundance of small-magnitude events and contain higher magnitude events than the downhole plots.

The decrease in large-magnitude events on the downhole plots can be associated with the way the magnitudes are measured. For example, this decrease can indicate that there is some sort of bias with the way the sensors are detecting the events, and assigning the events to a magnitude smaller than what they actually are. This can happen with a typical downhole array since these sensors usually record at a higher frequency than surface array sensors for capturing smaller magnitude events (Urbancic et al., 2013). The problem with this is that they are not recording the lower frequencies and therefore are not properly identifying the magnitude of the larger events. Figure 22 illustrates the frequency response of typical sensors and the Brune model plots for magnitude determination. The magnitude saturation is plotted as defined for sensors at 0.7Hz, 4.5Hz, and 15Hz (Urbancic et al., 2013). Synthetic events were computed with an assumed average stress drop of 0.1 MPa, and are showing magnitudes comparable to events recorded in a hydrocarbon reservoir (Viegas et al., 2012).

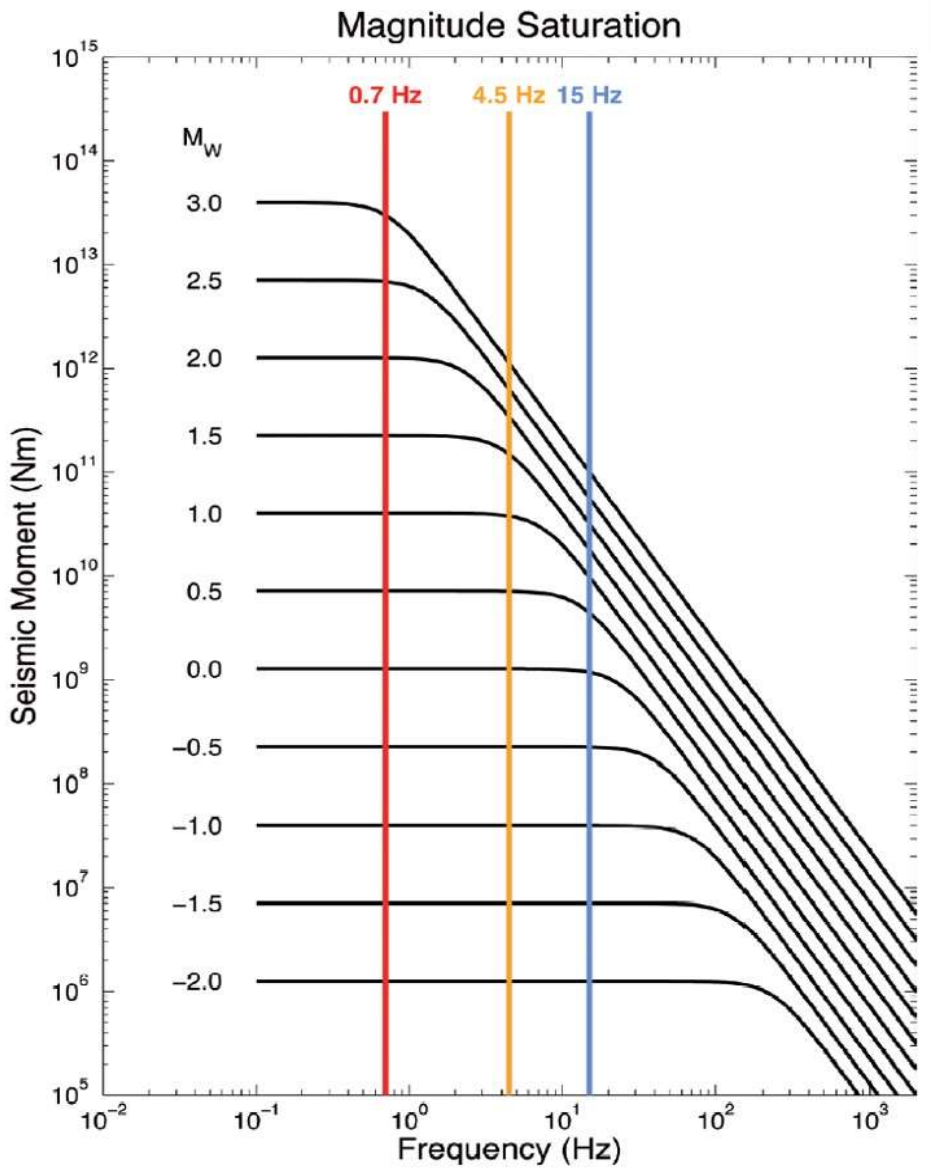

Figure 22. *Demonstration of how the sensors used in microseismic monitoring have certain restrictions in recording frequency and can affect the magnitude saturation. The magnitude saturation is plotted as defined for sensors at 0.7Hz, 4.5Hz, and 15Hz. Magnitude saturation occurs when the event corner frequency is greater than or equal to the recording frequency of the instrument, so the lower frequency sensor can capture larger seismic events than the higher frequency sensor (Urbancic et al., 2013).*

Magnitude saturation occurs when the event corner frequency is greater than or equal to the recording frequency of the instrument (Viegas et al., 2012). For example, in Figure 22 the 15Hz geophone appears to have a magnitude saturation at around Mw 0.5 because this is where the spectral plateau starts to fall outside of the recording bandwidth (Viegas et al., 2012). This means that Mw 0.5 is the highest magnitude that can be accurately recorded with that sensor. With this in mind, the 4.5Hz geophone has a magnitude saturation at around Mw 1.5 and the 0.7Hz geophone has a magnitude saturation at around Mw 3 (Viegas et al., 2012). If the recorded signal was captured by a geophone having a natural frequency higher than the event's corner frequency, then the signal will contain a fraction of the energy released at the source and give the appearance of a smaller magnitude than what it actually is (Urbancic et al., 2013). Based on Figure 22 the sensor with the lowest frequency response was able to accurately characterize all events, including the larger ones. This leads to the observation based on the frequency magnitude distributions in Figure 21, that the difference in the *b-values* between the downhole and surface events is that the downhole data shows a significant decrease in large-magnitude events compared to the surface data. The frequency response of the sensors from both arrays was never reported, therefore based on the frequency magnitude distributions in Figure 21, an observation can be made that the large-magnitude events recorded from the downhole array are not properly being characterized. This suggests us to believe the downhole sensors may be underestimating the strength of the stronger events and that the *b-values* of the surface events are more credible than those of the downhole events.

Differences in Event Detection

The same series of events identified as fault activation are used in Figure 23 to identify differences in surface and downhole event detection. This depicts a downhole geophone with event origin times of those events that are co-identified, as well as downhole- and surface-only detected events (Rich et al., 2016). What has been observed is that when two events occur very close in time, such as those events circled in black, one can see that the downhole array is only locating the earlier event, while the surface array is locating both events. This is most likely due to the event detection window missing the secondary events. Each event picked up by the surface array shows to have a larger amplitude than the event before it. The downhole array should have been able to pick up that signal. Because of these observations, these failed detections could very well be an artifact from the processing of the data, due to an error in the event location algorithm (Rich et al., 2016).

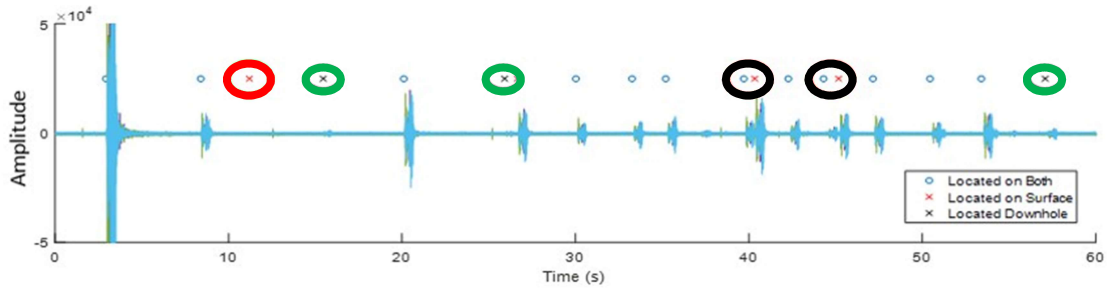

Figure 23. *Data from a downhole geophone with origin time of events from downhole and surface locations (Modified from Rich et al., 2016).*

Looking at Figure 23 once more, there is a single event captured only by the surface array, circled in red. It is possible that the downhole data lies along a nodal plane, which is what represents the boundary between positive and negative amplitude radiation patterns. Figure 24 depicts an example of the radiation pattern over a sphere centered on the origin, with plus signs denoting outward displacement and minus signs

denoting inward displacement (Aki and Richards, 2002). This is commonly referred to as a focal mechanism diagram, with the *Fault plane* and *Auxiliary plane* being the nodal planes, and *point P* marks the pressure axis and *point T* marks the tension axis (Aki and Richards, 2002). Since this event corresponds to a very low SNR on the surface catalog, this could also be a false event (Rich et al., 2016). Going back to Figure 23, the final note to point out are the smallest amplitudes on the plot, circled in green, correspond with downhole detection only, because they are too small for the surface array to detect.

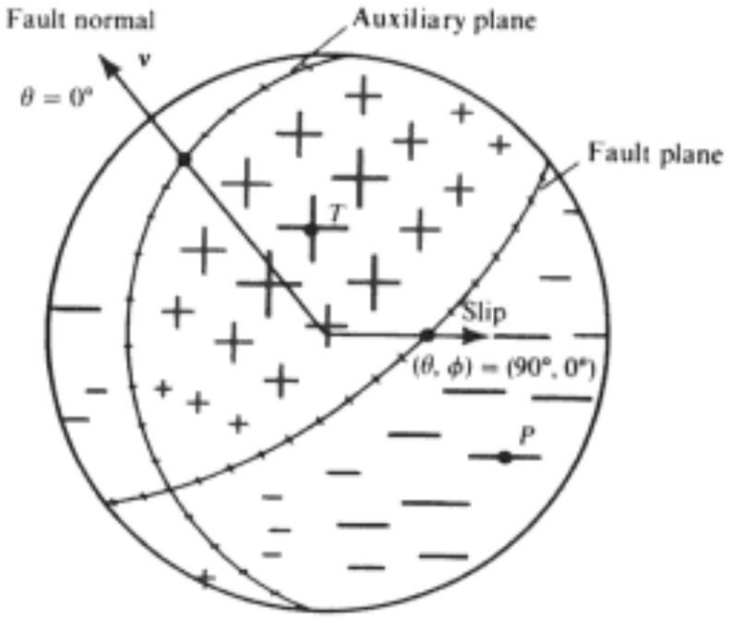

Figure 24. *The radiation pattern over a sphere centered on the origin, with plus signs denoting outward displacement and minus signs denoting inward displacement. The Fault plane and Auxiliary plane are nodal planes, and point P marks the pressure axis and point T marks the tension axis (Aki and Richards, 2002).*

Chapter 6: Waveform Analysis

Visualizations of the surface and downhole signals play an important part in this research, as it enhances our understanding of the components of the waveform.

Figure 25. *Downhole Signal:*

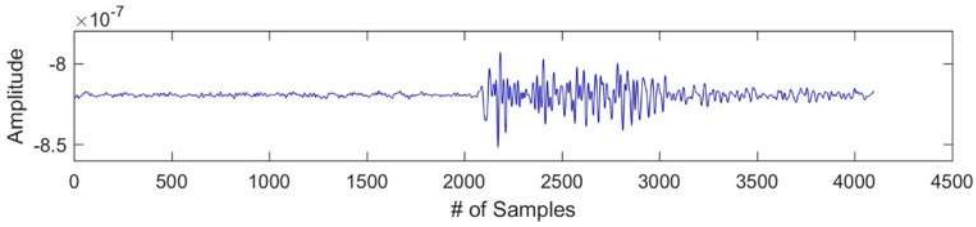

Figure 26. *Surface Signal:*

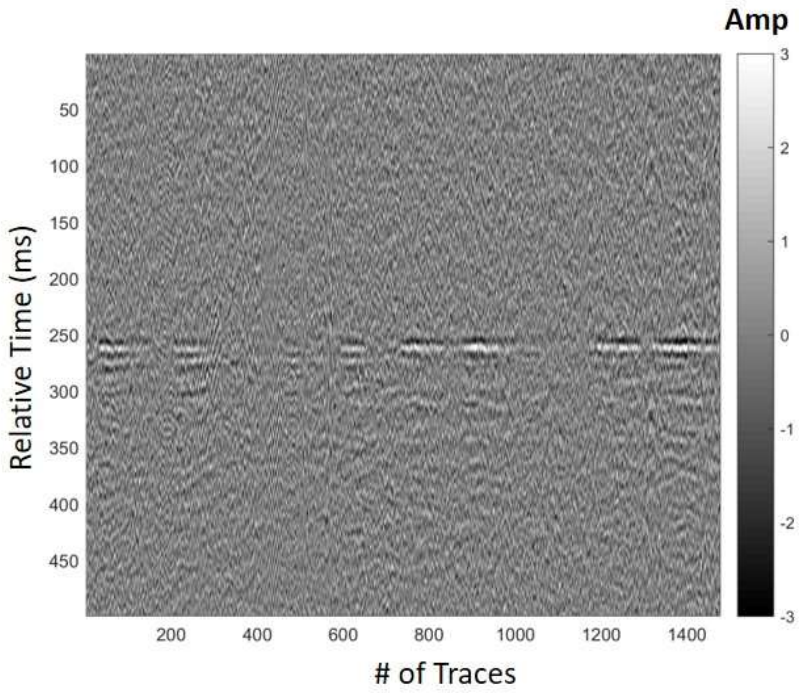

Figure 25 shows a single trace from the 36 traces being recorded from the twelve 3-component sensors. The Y-axis is the amplitude and the X-axis is the number of samples recorded. What is being shown for the surface signal in Figure 26 is one gather from all ten arms of the surface array with NMO applied, aligning the events in time.

The Y-axis is relative time of a 500 ms time window centered on the event. The X-axis is the relative trace number. There is one trace from every surface geophone, and with 1,476 total geophones in the array, each of the plotted surface signals displays 1,476 traces. Significant shear-wave data were recorded along with the P-wave data, however only the P-wave was imaged from the surface array.

Chapter 7: Spectral Ratio Method

Signal Attenuation and Quality Factor

Velocities are usually considered to be independent of frequency, which would imply a purely elastic homogeneous earth (Haase and Stewart, 2003). This is an invalid assumption, which would then bring up the question as to why there would be such a significant discrepancy between two sets of microseismic events acquired by two different modes of acquisition. Velocity dispersion can account for this due to anelastic behavior of the rock (Haase and Stewart, 2003). To better understand the difference between the downhole array events and the surface array events, attenuation must be considered.

Attenuation of the seismic signal due to the seismic waves travelling a longer distance to reach the surface geophones may be a reasoning behind the depth discrepancy. Since attenuation increases with distance, the events recorded on the surface array should be more affected in terms of amplitude and frequency than those recorded on the downhole array. This leads to a greater error in the picking of the P- and S-wave arrival times on the surface array (Igonin and Eaton, 2016). An increase in time delay between the P- and S-wave arrival times could explain why events located by surface arrays would be deeper than events located by downhole arrays (Igonin and Eaton, 2016). Figure 27 demonstrates this, as shown by Igonin and Eaton (2016). In the figure, an experimental model was set up, in which a downhole array and a surface array were designed, and seismic traces from each mode of acquisition was compared. These traces were modeled with and without attenuation. It can be shown that the higher the frequency and the longer the distance, the larger the time difference between the picked arrival

time, with and without attenuation (Igonin and Eaton, 2016). It is possible that the velocity models used for each array may contribute to the depth discrepancies observed, but considering both vendors produced and calibrated their own models for processing, there is reason to trust the accuracy of these models. Therefore, the focus is geared toward the study of the attenuation factor and how it may play a role in the mislocation of events.

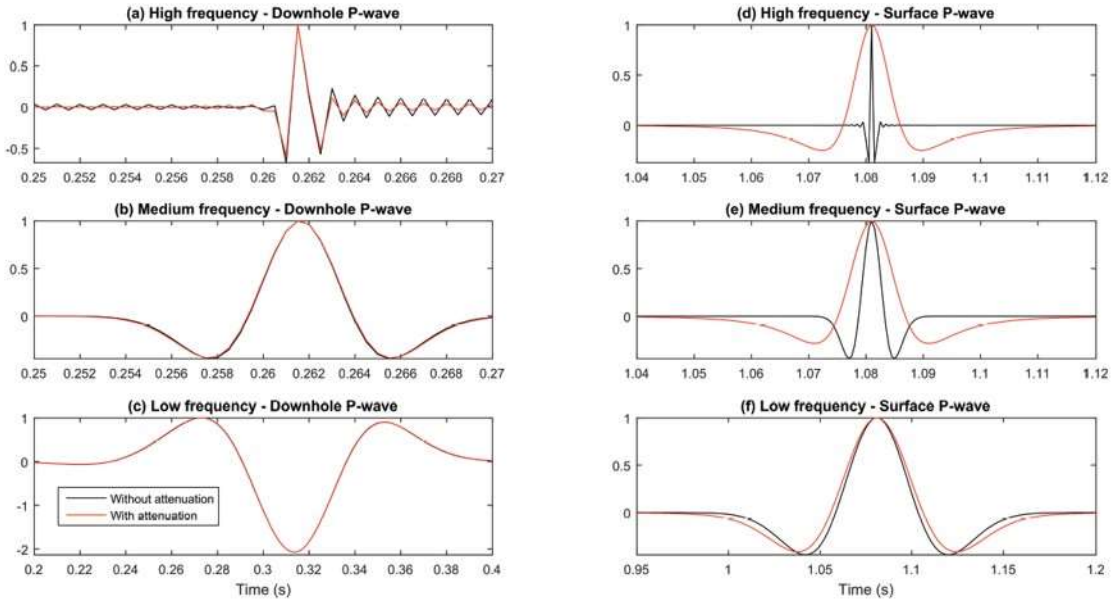

Figure 27. *An experimental model showing a comparison of traces with and without attenuation. Left side shows traces from a downhole geophone and right side shows traces from a surface geophone. High frequency means 1000 Hz, medium frequency is 100 Hz, and low frequency is 10 Hz. The effect of attenuation can clearly be seen on the surface waves. It can be seen here that the higher the frequency and the longer the distance, the larger the time difference between the picked arrival time, with and without attenuation (Igonin and Eaton, 2016).*

To further analyze and characterize attenuation, the spectral ratio method was performed to determine an estimation of Q, or quality factor, which is what describes the seismic energy loss through a material. It finds the ratio of the energy stored to the energy lost per frequency cycle due to anelasticity (Cheng and Margrave, 2008), which is what causes velocity dispersion (Haase and Stewart, 2003). Velocity dispersion is

what changes a waveform's shape due to a decrease in the amplitude, where the amplitude is a function of frequency (Igonin and Eaton, 2016).

In general Q describes energy loss, but specifically it is what measures the absorption of a material (Igonin and Eaton, 2016). The inverse of Q (Q^{-1}) measures the attenuation factor of a material. A large Q value describes a material with low absorption losses, whereas a small Q value describes a material with high absorption losses (Igonin and Eaton, 2016). Q values between 20 and 100 are typical of Earth materials with values below 40 considered to be 'low' (Igonin and Eaton, 2016). There are a variety of methods that can be used to estimate the Q-factor, however, none of these methods is significantly better than the others in all situations (Haase and Stewart, 2003). Most of these computational methods can result in different Q values, even for the same type of materials (Badri and Mooney, 1987). One of the better-known methods out of all of these is the spectral ratio method (Tonn, 1989). Since the compressional waves of the microseismic events were generated from several different source signatures, this makes the spectral ratio method preferable to use since it is independent of the source (Badri and Mooney, 1987). For this thesis, Q was computed for the events recorded on the downhole array using the spectral ratio method.

Q Estimation along a Downhole Receiver Array

The spectral ratio method was described in detail by Bath (1974) in which he discussed how its application can be used in three different ways: as the frequency-ratio, station-ratio, and wave-ratio methods. The method used in this thesis most closely matches Bath's station-ratio method, in that an amplitude ratio is computed at two stations, or in this case, two distances, making a more general term for this method to be the distance-ratio method (Bath, 1974).

The spectral ratio method is used to compute an attenuation factor by analyzing the changes in spectra between two different depth levels (Haase and Stewart, 2004):

$$\ln\left[\frac{\left|A(\omega,t_2)\right|}{\left|A(\omega,t_1)\right|}\right] = (const\ .) - \omega\,\frac{d}{2cQ}\ , \tag{2}$$

where $A(\omega,t_1)$ and $A(\omega,t_2)$ are the spectral amplitudes at different depths based on the arrival times of the direct arrivals, $\omega = 2\pi f$ is the angular frequency, d is the travel distance, c is the travel velocity, and Q is the quality factor (Haase and Stewart, 2004). The expression, $-\omega\frac{d}{2cQ}$, can be rewritten as $\frac{\pi\delta t}{Q}f$, transforming the equation into the following (Tonn, 1989):

$$\ln\left[\frac{\left|A(\omega,t_2)\right|}{\left|A(\omega,t_1)\right|}\right] = (const\ .) - \frac{\pi(t_2\text{-}t_1)}{Q}f\ , \tag{3}$$

where the *(const.)* variable represents the y-intercept of the linear regression, (t_2-t_1) is the difference in arrival times, and f is the frequency representing the x-value. This version of the formula was coded into MATLAB.

Due to the complexity of the surface array and the number of factors involved in finding a proper Q value for the surface events, it was determined that for this thesis only the downhole events were to be quantitatively evaluated for Q. Certain factors affecting a proper Q analysis of the surface events include the signal being too weak to measure due to a greater distance away from the source, the free-surface effect, radiation patterns, and instrument response to name a few. Most of these issues can be corrected for with the appropriate resources, however the main issue with the surface events is the low SNR. The downhole events are better to work with due to the better signals received from being closer to the source. Also, the number of sensors used are dramatically less than the number used for the surface array, making our workflow more organized.

To include the surface data into our research, a side-by-side comparison of the downhole Q values were made against their corresponding surface signals' waveform. The amplitude spectrum of the events in the downhole array were also compared to the amplitude spectrum of the events from the surface array. After doing this, a better understanding of attenuation can be made as the signals travel to the surface. In the end, a quantitative analysis was made for the downhole events, while a qualitative analysis was made for the surface events. Since the source signature is not known for these events, the goal of this study is not to determine the type of attenuation that is measured, but rather only a measurement of the total Q observed by the downhole mode of acquisition, and what the apparent attenuation is for the surface mode of acquisition.

For the downhole events, we determined an average Q for the highest signal-to-noise ratio (SNR) event of every stage, adding up to a total of 12 events for analysis. These

events gave us the best amplitude response, as the higher the SNR, the more confident the data (Maxwell, 2009), which should lead to a more accurate Q value. Multiple steps were taken to prepare the data for spectral ratio analysis. All the data processing and analysis was done in MATLAB. The process was set up in the following order:

1. **Determine the sensor orientation for the downhole receivers** – It is important to know the orientation we are starting with. The angles of orientation for the X and Y components of each geophone were calculated, and those values were used to help determine the proper angle of rotation for the components.
2. **Apply vector rotation to the traces** – We wanted to rotate the X and Y (azimuthal) components so that the P-waves reach maximum signal response. This helped determine where exactly the direct arrival of the P-wave was to isolate it for analysis.
3. **Pick direct arrivals of P-waves and apply mute to traces** – The arrival times mark where the limits are for the mutes that are applied to the traces. The mute is meant to take out the noise on the front-end of the trace, any scattered events immediately after the direct arrival, and the S-wave on the back-end of the trace.
4. **Estimate Q using spectral ratio method** – Once all signals were prepared for analysis, the spectral ratio algorithm was applied, determining an estimation of Q between the near vs. far geophones.
5. **Qualitatively interpret the surface signals and compare to downhole signals** – The surface signals were plotted and through observation of the waveform, can be compared to the results of each of their co-identified downhole events.

Sensor Orientation for Downhole Receivers

A sensor orientation spreadsheet was provided by the vendor for the downhole geophones (Table 1). The geophones are labeled from '1' being the topmost sensor, to '12' being the deepest sensor. As mentioned before, these are 3C sensors, and the *Axis_Number* column corresponds the numbers *0, 1, 2* with the X, Y, Z components, respectively. Of the twelve sensors in the array, each one had three components or *channels*, so therefore, 12x3=36 channels.

Instrument_Number	Instrument_Label	Channel_Number	Down	Axis_Number	Orientation_N	Orientation_E	Orientation_D
1	VSI-12_001	1	9500.763158	0	0.615926	-0.787656	-0.015274
1	VSI-12_001	2	9500.763158	1	-0.787687	-0.615385	-0.029173
1	VSI-12_001	3	9500.763158	2	0.013579	0.03	-0.999458
2	VSI-12_002	4	9600.671579	0	-0.293598	0.955652	0.023013
2	VSI-12_002	5	9600.671579	1	0.955006	0.292172	0.050987
2	VSI-12_002	6	9600.671579	2	0.042001	0.036948	-0.998434
3	VSI-12_003	7	9700.472766	0	-0.541771	-0.83802	-0.06485
3	VSI-12_003	8	9700.472766	1	-0.838487	0.544217	-0.02771
3	VSI-12_003	9	9700.472766	2	0.058514	0.039364	-0.99751
4	VSI-12_004	10	9800.218737	0	0.998374	0	0.056999
4	VSI-12_004	11	9800.218737	1	0.002436	-0.999086	-0.042667
4	VSI-12_004	12	9800.218737	2	0.056947	0.042736	-0.997462
5	VSI-12_005	13	9899.971684	0	0.243913	-0.969301	-0.031009
5	VSI-12_005	14	9899.971684	1	-0.968345	-0.241674	-0.062463
5	VSI-12_005	15	9899.971684	2	0.053052	0.045263	-0.997565
6	VSI-12_006	16	9999.728085	0	-0.882846	0.468993	-0.02502
6	VSI-12_006	17	9999.728085	1	0.466746	0.882048	0.064323
6	VSI-12_006	18	9999.728085	2	0.052237	0.045109	-0.997615
7	VSI-12_007	19	10099.42442	0	-0.59805	-0.797438	-0.08018
7	VSI-12_007	20	10099.42442	1	-0.799162	0.600913	-0.015615
7	VSI-12_007	21	10099.42442	2	0.060633	0.054738	-0.996658
8	VSI-12_008	22	10199.1239	0	-0.541348	-0.837737	-0.071679
8	VSI-12_008	23	10199.1239	1	-0.838722	0.544033	-0.023942
8	VSI-12_008	24	10199.1239	2	0.059052	0.047157	-0.99714
9	VSI-12_009	25	10298.86894	0	-0.888528	-0.453613	-0.068937
9	VSI-12_009	26	10298.86894	1	-0.455318	0.890266	0.01053
9	VSI-12_009	27	10298.86894	2	0.056596	0.040745	-0.997565
10	VSI-12_010	28	10398.58421	0	-0.975903	-0.207635	-0.067098
10	VSI-12_010	29	10398.58421	1	-0.210475	0.976846	0.038379
10	VSI-12_010	30	10398.58421	2	0.057576	0.051577	-0.997008
11	VSI-12_011	31	10498.29842	0	-0.943203	-0.325126	-0.068266
11	VSI-12_011	32	10498.29842	1	-0.327763	0.944234	0.031521
11	VSI-12_011	33	10498.29842	2	0.054211	0.052106	-0.997169
12	VSI-12_012	34	10598.1	0	-0.036282	0.998746	0.034495
12	VSI-12_012	35	10598.1	1	0.998571	0.034877	0.040501
12	VSI-12_012	36	10598.1	2	0.039247	0.035915	-0.998584

Table 1. *Downhole sensor orientation spreadsheet (Provided by IMaGE).*

The *Channel_Number* column numbers every X, Y, Z component for every sensor. This leads into the data structure for every downhole event captured. All downhole events were delivered in .SGY format, and when opened in MATLAB. Every downhole event had a total of 36 columns, which translates to 36 traces—3 from every sensor in the array. The number of rows varied throughout the stages, as they represent the number of samples taken for each trace. Stages 1 – 4 contains 4096 samples, or 2.048 seconds for every trace, stages 5 – 11 contains 2048 samples, or 1.024 seconds for every trace, and stage 12 contains 1024 samples, or 0.512 seconds for every trace. The differences in record length are likely due to the data being cut out of continuously recorded data based on where events are detected. Stages 1 through 12 start from the toe of the well and end at the heel, and the closer the stages are to the heel, the smaller the window is needed to capture both P and S waves.

The orientations (*Orientation_N, Orientation_E, Orientation_D*) of the X, Y, and Z components were provided to us. We assume the geophones are vertical—since the wellbore is vertical—and rotate the X and Y (azimuthal) horizontal components to determine the direction back to the source. The Z (inclinational) component is vertical, and since we cannot assume homogeneity in the vertical plane due to layering, it would be difficult to determine that orientation without the use of hodogram analysis. We want to compute the radial and tangential components of ground motion based on the observed X and Y components (Ammon, 2001). Rotation of the radial and tangential components will also maximize the P-waves from the shear waves (Ammon, 2001). It is ideal to rotate the geophone into the direction of the incoming wave so that maximum

amplitude of the P wave is achieved, and therefore the orthogonal components of the geophone will have the maximum amplitude of the shear waves.

A coordinate system is displayed in Figure 28, which can be comparable to the structure of a geophone from our downhole array. The north and east components are shown but not the vertical (Z) component. The radial and tangential components are what characterize the geophone's orientation in the horizontal direction. These components were what were used to rotate the geophone for better alignment with a single microseismic event. Better alignment results in better signal response and better analysis of the seismic waves. The radial and tangential components will always be orthogonal to each other, even after vector rotation.

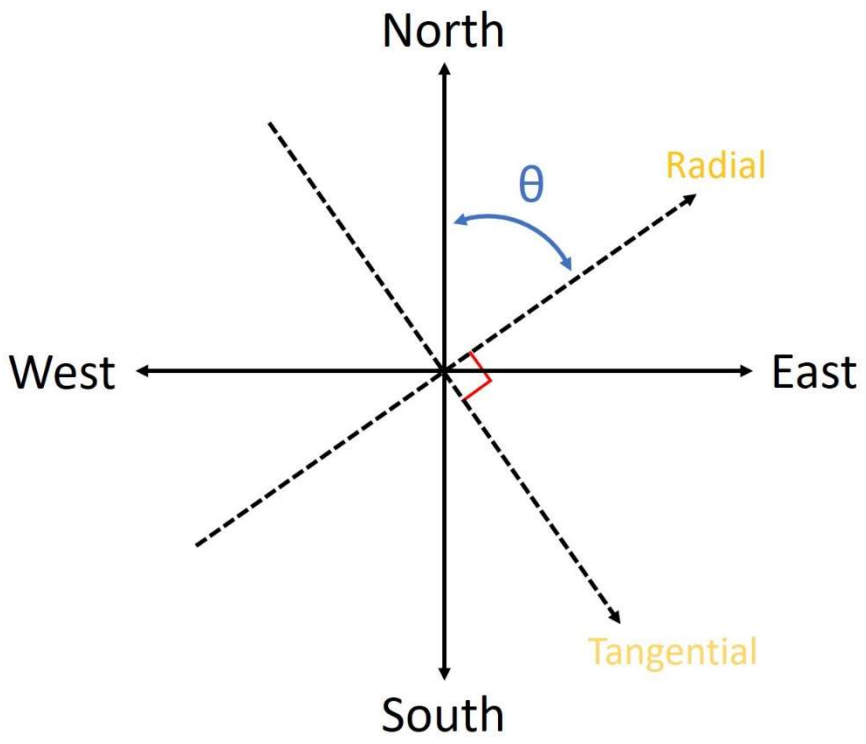

Figure 28. *A simple coordinate system can be used to describe the structure of a geophone in our downhole array. The radial and tangential components shown here will be rotated to better align the geophone with the microseismic event for better signal response.*

To calculate the orientations of the sensors, all that was needed to be done was determine the orientation of the X component, and then base the radial and tangential vector rotation off that value. In this case, we based all our vector rotations off the values listed under the *Orientation_N* column of the spreadsheet. No significance was behind using the *Orientation_N* column over the *Orientation_E* column. Either way would be fine because the Pythagorean Trigonometric Identity can be used to show the complementary characteristics of the north and east orientations, as shown in Table 1, because $(Orientation\_N)^2 + (Orientation\_E)^2 = 1$, much like the identity in Figure 29, $\cos^2\theta + \sin^2\theta = 1$. The values under *Orientation_N* were determined to be the direction cosines, and using trigonometric functions would define the angles using the arc cosine function (Figure 29). Our focus is on the radial component, which is written as $\cos(\theta) = \frac{x}{r}$. Then, $\arccos\left(\frac{x}{r}\right)$ is used to find θ.

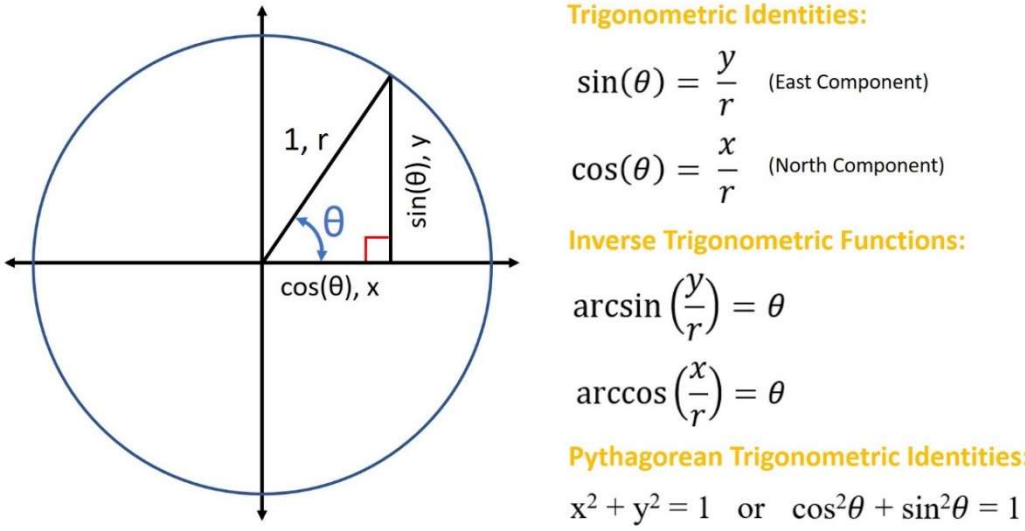

Figure 29. *Trigonometric functions and identities used to determine original angle orientation of the X and Y components of each geophone. The angles were defined by taking the arc cosine of a given value and then converting the result from radians to degrees. A north and east orientation for each X and Y component were provided by the vendor. The relationship between north and east is shown by the pythagoean trigonometric identity, where both values are complimentary with each other and add up to 1.*

Vector Rotation

The next step was to apply a vector rotation to the radial and tangential components of each of the twelve geophones. Prior to vector rotation, a simple bandpass filter was applied to the traces, removing the high and low frequencies. Upon vector rotation, both radial and tangential components shift a certain amount of degrees, keeping them both orthogonal at all times. We wanted to rotate these components in such a way that the P-wave of the recorded signal increases while also removing the influence of the shear waves. In the end, we want to isolate the P-waves of the downhole events for analysis when comparing with the surface events since the P-waves were only imaged from the surface events. More specifically, we want to isolate the direct arrival of the P-waves for the downhole events because it contains the most reliable information, since it most likely does not include complex coda waves.

Figure 30 shows the significance of vector rotation. The microseismic waves hit the geophone at an arbitrary angle, and we mathematically rotated the components to maximize P-wave energy. By rotating the vectors in the direction of the signal, we are adjusting the amplitude response, therefore maximizing the P-wave on the radial component, and maximizing the shear wave on the tangential component. It is the radial component that was used for the spectral ratio method since it was the component with the highest P-wave influence.

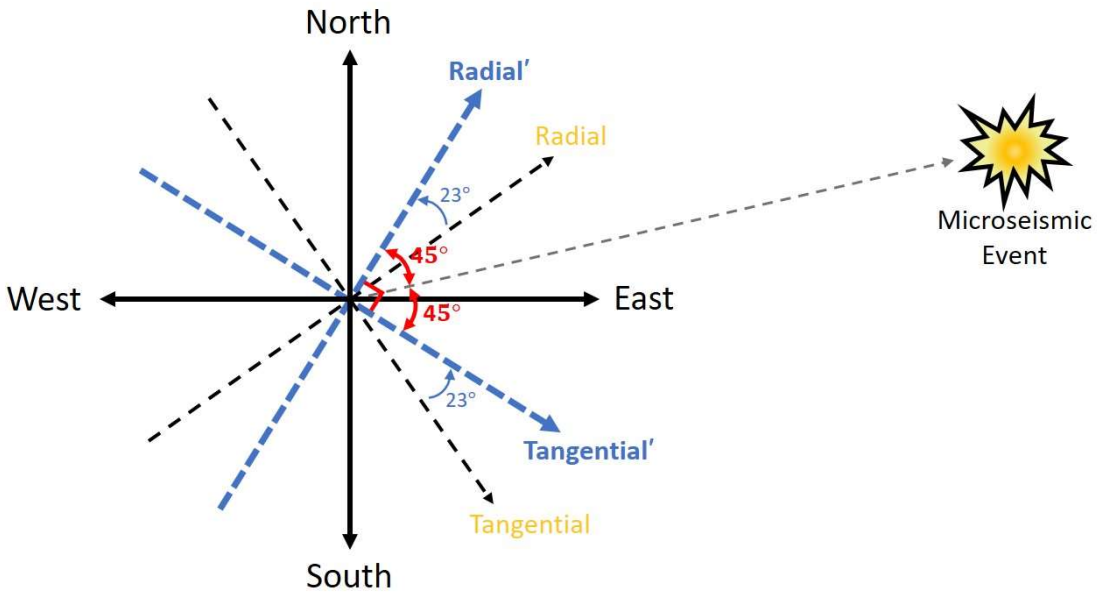

Figure 30. *Diagram showing the concept behind vector rotation. In this case, the radial and tangential components are situated in such a way where they need to shift 23° to align with the microseismic event. We mathematically rotated the components to maximize P-wave energy. The vectors with yellow labels are the original orientation and the vectors with the blue labels are the rotated orientation.*

In MATLAB, the data was filtered and then rotated according to the angles calculated in Table 1. The variables required for input include the X and Y components of every geophone (*Channel_Number* column from Table 1) and the angle of rotation. The outputs would be the rotated radial and tangential components. Note that the angle values calculated from Table 1 are not the final values used. They were initially used as a consistent starting point, and then rotated from there until maximum P-wave energy was reached. The goal of the vector rotation was to adjust the amplitude response of the shear waves in that we want to minimize them so they will provide a smoother amplitude spectrum in the end.

For each of the 12 events analyzed, vector rotation was applied to only the traces recorded from geophones 1 and 12. We wanted to limit this analysis down to the

nearest vs. farthest geophone because the depth between these two is at about 1,100 ft. In our case, the near geophone is geophone 12 (closest to the source) and the far geophone is geophone 1 (farthest from the source). Figure 31 shows the downhole array in relation to the frack stages and the order at which each are numbered. Stage 1 and geophone 1 are the farthest distance from each other while stage 12 and geophone 12 are the closest distance to each other.

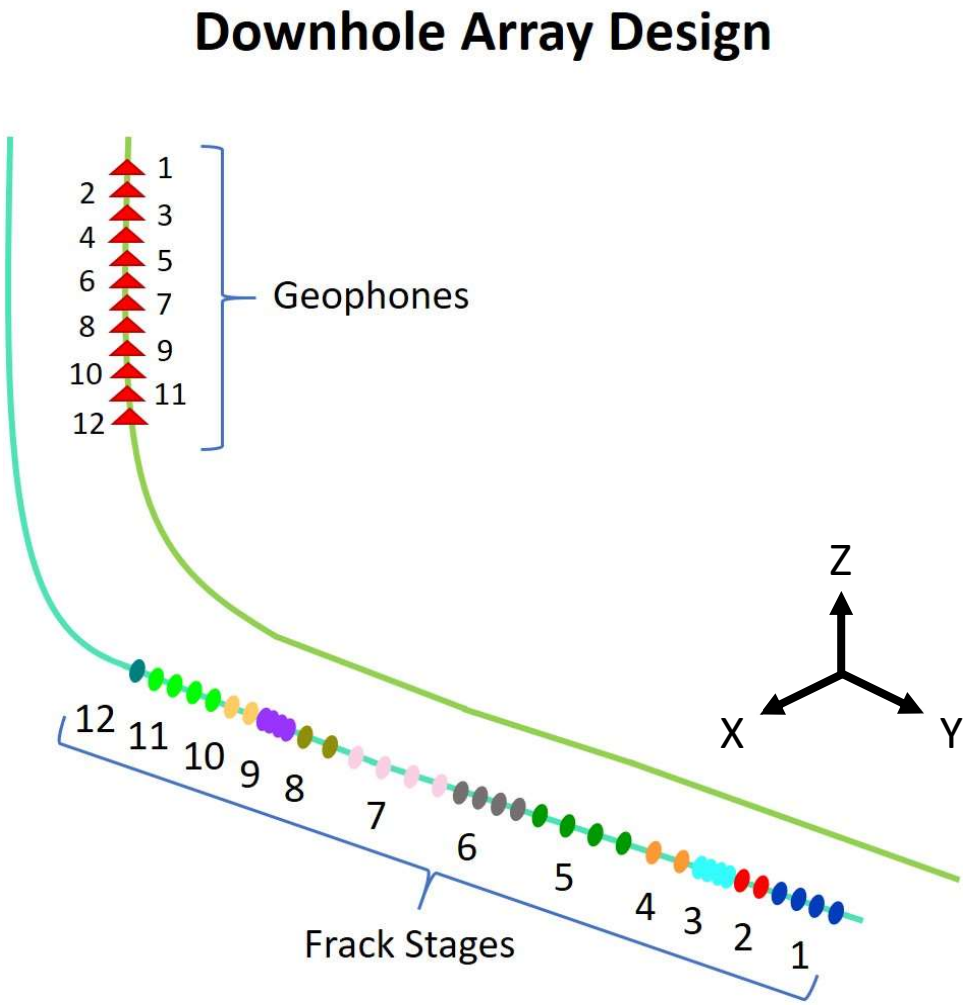

Figure 31. *Downhole array in relation to the frack stages and the order at which each are numbered. The well on the bottom is the treatment well and the well on the top is the monitor well. It is easier to see here why geophone 12 is considered "near" and geophone 1 is considered "far." Geophone 12 is deepest in the array and therefore closest to the source of the fracks.*

According to the Q model, the amplitude spectrum would be too unstable when Q is estimated at such a small depth range, such as between immediately neighboring geophones, where there is not much observable attenuation (Margrave, 2017). We calculated Q only between the amplitude spectrums of geophones 1 and 12 because based on the Q model, a smaller offset between geophones would cause problems. The closer the distance between two geophones get, the smaller the slope will be on the amplitude-frequency spectrum (amplitude ratio), therefore resulting in a large and impractical Q value (Margrave, 2017). We chose geophone 1 and 12 because it maximized our chance of success.

Filtering and vector rotation was applied to the highest SNR event from stage 9 (Figure 32). The figure shows the traces recorded from geophone 1. The first two traces display the filtered X and Y components before vector rotation. The last two traces show the resultant radial and tangential traces after vector rotation. As the traces undergo rotation, they are also shifted to centralize at zero mean, removing the DC component. Notice how the radial component has a distinct P-wave arrival, due to the high amplitude response making it easier for picking. There is quite a bit of noise on the back-end of this trace, however, that will be removed at a later step when the mute is applied. This will cut off the rest of the trace as we are only wanting to analyze the P-wave for this thesis. All 12 stages can be viewed in Appendix A.

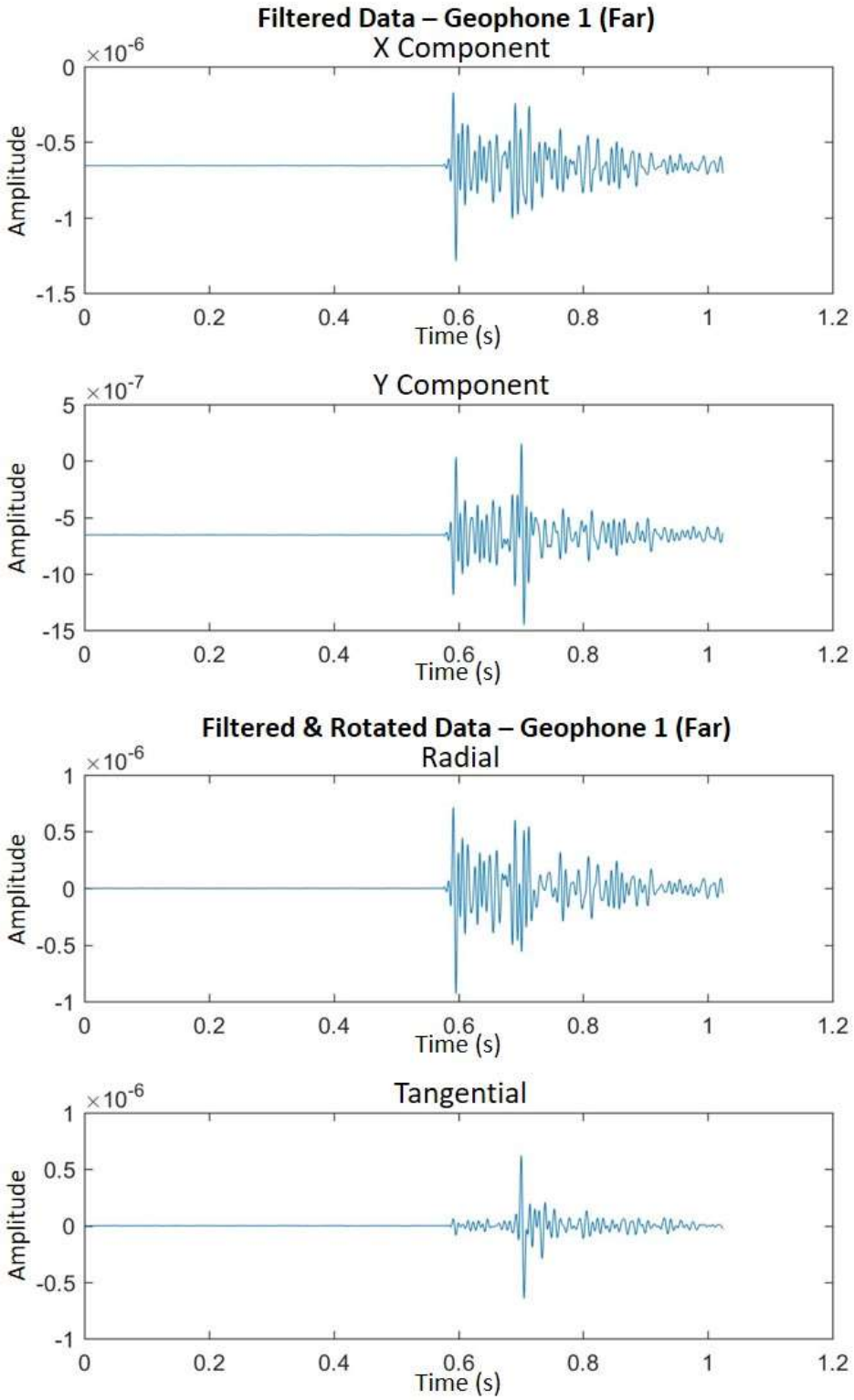

Figure 32. *The first two traces display the filtered X and Y components before vector rotation. The last two traces show the resultant radial and tangential traces after vector rotation and removal of the DC component, centralizing the signal at 0. Notice how the radial component has a distinct P-wave arrival, due to the high amplitude response, making it easier for picking.*

Muting the Signals

After vector rotation has been applied to all 12 events, the direct P-waves must now be picked. A window is designated for each direct arrival. This window will define the limits for the mute that will be applied to these traces, ultimately taking out the noise on the front-end of the trace, any scattered events immediately after the direct arrival, and the S-wave and coda on the back-end of the trace. The arrival times are different between stages, and furthermore between geophones. The arrival times are only the same between radial and tangential components of the same geophone. The window size, however, of the far geophone mutes are the same length as the window size of the near geophone mutes amongst geophones of the same stage. This is because we want the window sizes to be consistent, in that ideally, we want to compare the direct arrival of the near geophone with the direct arrival of the far geophone by removing as many of the later arrivals that have been superimposed onto the signal.

Next, the mute must be applied to all traces to isolate the direct arrival. The amplitude spectrums shown in this thesis will be plotted using relative amplitude, which is in decibel scale. A tapered mute was selected to avoid ringing associated with the Gibbs phenomena. The mute was designed to add a tapered effect in that it was logarithmic, starting from 1 (highest point on the amplitude scale) to 0 (Figure 33). The top left edge of the mute indicates where the direct P-wave arrival pick is, and the top right edge of the mute indicates where the direct P-wave arrival ends. Notice as the mute approaches closer and closer to zero-amplitude, it appears to have a softer, curved appearance. The logarithmic algorithm is applied at every sample number starting from the top of the mute, which allows the mute to get substantially smaller as it approaches zero-

amplitude. The sample number at each edge of the mute is determined by taking the arrival time pick, and dividing that number by the sample rate at which the data was captured (0.5ms, or 0.0005s). All signals with superimposed mutes are displayed in Appendix B.

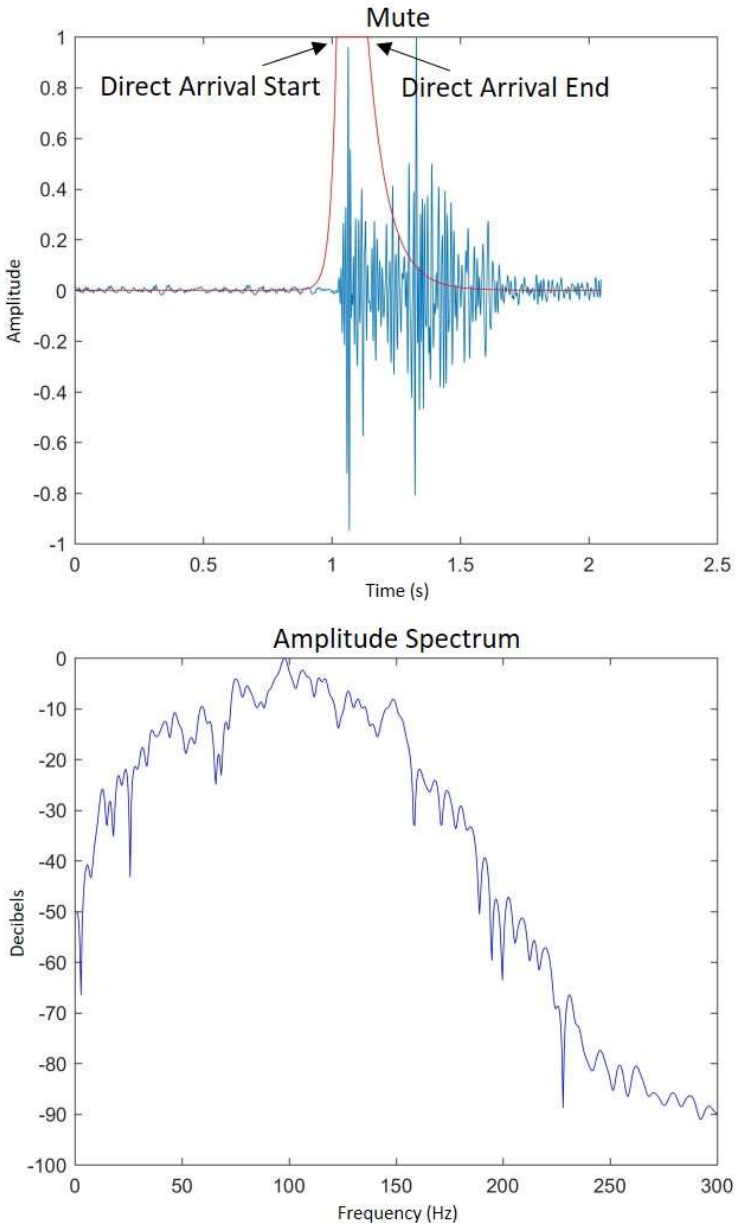

Figure 33. *The design for the new mute is shown in the top image and the resulting amplitude spectrum is shown in the bottom image. The mute applied now has more of a tapered effect, and the beginning and end of the direct P-wave arrival is shown, as they provide the limits as to where the mute is not applied in order to isolate the direct arrival.*

Application of the Spectral Ratio Method

By this point all signals have gone through filtering, vector rotation, and muting and are now ready for the spectral ratio method for determining a Q value at each stage of the microseismic shoot. The spectral ratio method compares amplitude response from geophone one with the amplitude response from geophone twelve. In other words, we looked at the bottom-most geophone of the array (near) vs. the top-most geophone of the array (far).

The spectral ratio script in MATLAB was written to perform all preparation and final output all at once. A flow chart showing the overall inputs and outputs of the process are shown below in Figure 34. This process is repeated for all 12 events.

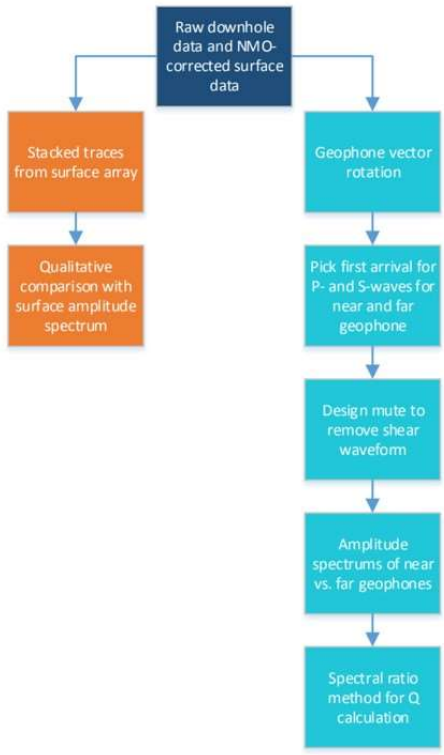

Figure 34. *A flowchart that illustrates the inputs that were computed and the data that was output. The dark blue box represents the inputs and the orange boxes represent the surface data outputs while the aqua-colored boxes represent the downhole data outputs.*

The amplitude spectrum was computed from the absolute value of the Fourier transform of the muted signal. Very commonly, when an amplitude spectrum is displayed, the frequency is not plotted against raw amplitude, but instead plotted against the relative amplitude in decibels. The amplitude units were then converted into decibels with the following formula:

$$\mathrm{dB} = 20log_{10}\frac{A}{A_{max}} \quad , \tag{4}$$

where A is the amplitude at each frequency and A_{max} is the relative maximum amplitude. The decibel units are a relative measurement and therefore it is best to use the same reference amplitude for both near and far geophones.

The amplitude ratios are plotted using the logarithm of the ratio of the near and far geophone's amplitude spectrum, against its corresponding frequency. A line of best fit was plotted on every amplitude ratio plot. Figure 35 shows a side-by-side comparison of an amplitude spectrum with an amplitude ratio.

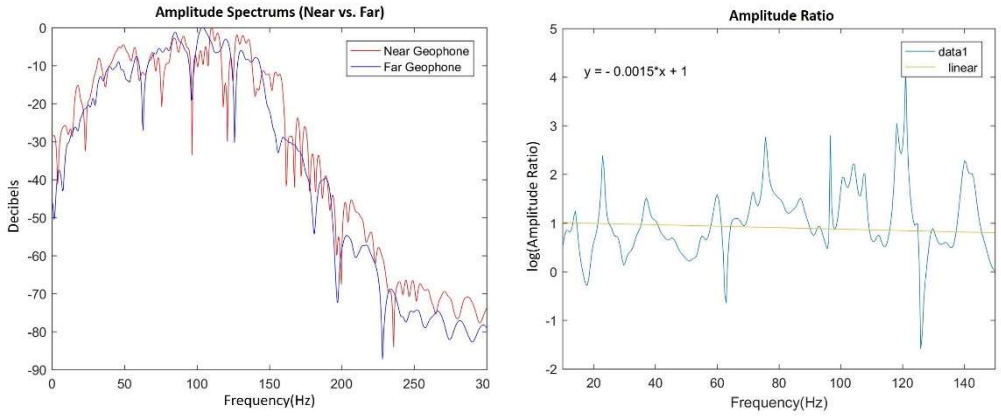

Figure 35. *The downhole amplitude spectrums and amplitude ratio of stage 2. The amplitude ratio is the log of the ratio of the amplitude spectrums and produces a slight downward slope.*

The amplitude ratio plots range from 10Hz – 150Hz on the frequency scale because based on the amplitude spectrums, the signal response dies off before 10Hz and after 150Hz. A line of best fit is plotted on the amplitude ratio and the value of the slope is what is needed for the determination of the Q value. All amplitude ratios and corresponding amplitude spectrums between near vs. far geophones are shown in Appendix C.

A Q value is calculated by taking the value of the slope from the spectral amplitude ratio and setting that equal to $\frac{\pi \delta t}{Q}$ in the spectral ratio formula:

$$m = -\frac{\pi(Tp2 - Tp1)}{Q} \quad , \tag{5}$$

where *m* is the slope, *Tp1* is the direct P-wave arrival time for the near geophone and *Tp2* is the direct P-wave arrival for the far geophone. We can rearrange this formula to solve for Q:

$$Q = -\frac{\pi(Tp2 - Tp1)}{m} \quad . \tag{6}$$

Using this formula and applying all the necessary values will result in a representative Q value for every stage. A list of Q values for all 12 events are listed in Table 2.

Event (By Stage)	Downhole Magnitude	SNR	Slope	Q Value
1	-0.549	34.867	-0.0031	13.1744
2	-0.68	16.006	-0.0015	27.2271
3	-0.302	135.449	-0.0033	17.136
4	-0.157	212.076	-0.0028	26.9279
5	-0.557	159.779	-0.001	62.8319
6	-0.271	622.862	0.0028	-36.4649
7	-0.352	284.076	0.0036	-27.9253
8	-0.791	109.503	0.0082	-23.5619
9	-0.422	1074.41	0.0095	-15.5426
10	-0.545	749.372	0.014	-10.098
11	-0.461	970.16	0.0041	-46.7408
12	-0.941	222.32	-0.0028	76.8568

Table 2. *List of Q values for all 12 events.*

Each event in the chart is numbered based on the stage it is from, therefore every Q value is considered representative of that stage. The Quality factor from stages 1-5 appear to be positive values, however stages 6-11 appear to have positive slopes therefore giving them negative values for Q. As the stages progress from first to last, their distance from the downhole array gets shorter and shorter, meaning less attenuation. Q is generally considered a constant, however Table 2 shows that Q is varying spatially. The change in Q is unknown, but could be explained by the noise in the data, as well as a varying lithology that is affecting the analysis. This sheds some light into just how complex these waveforms are.

The velocity model was produced from the dipole sonic log of the treatment well (Figure 36). All 12 geophones are placed according to their true depth location in the downhole array of the nearby monitor well, 600 ft. east of the treatment well. This is done to correlate geophones 1 and 12 to their position on the velocity curves.

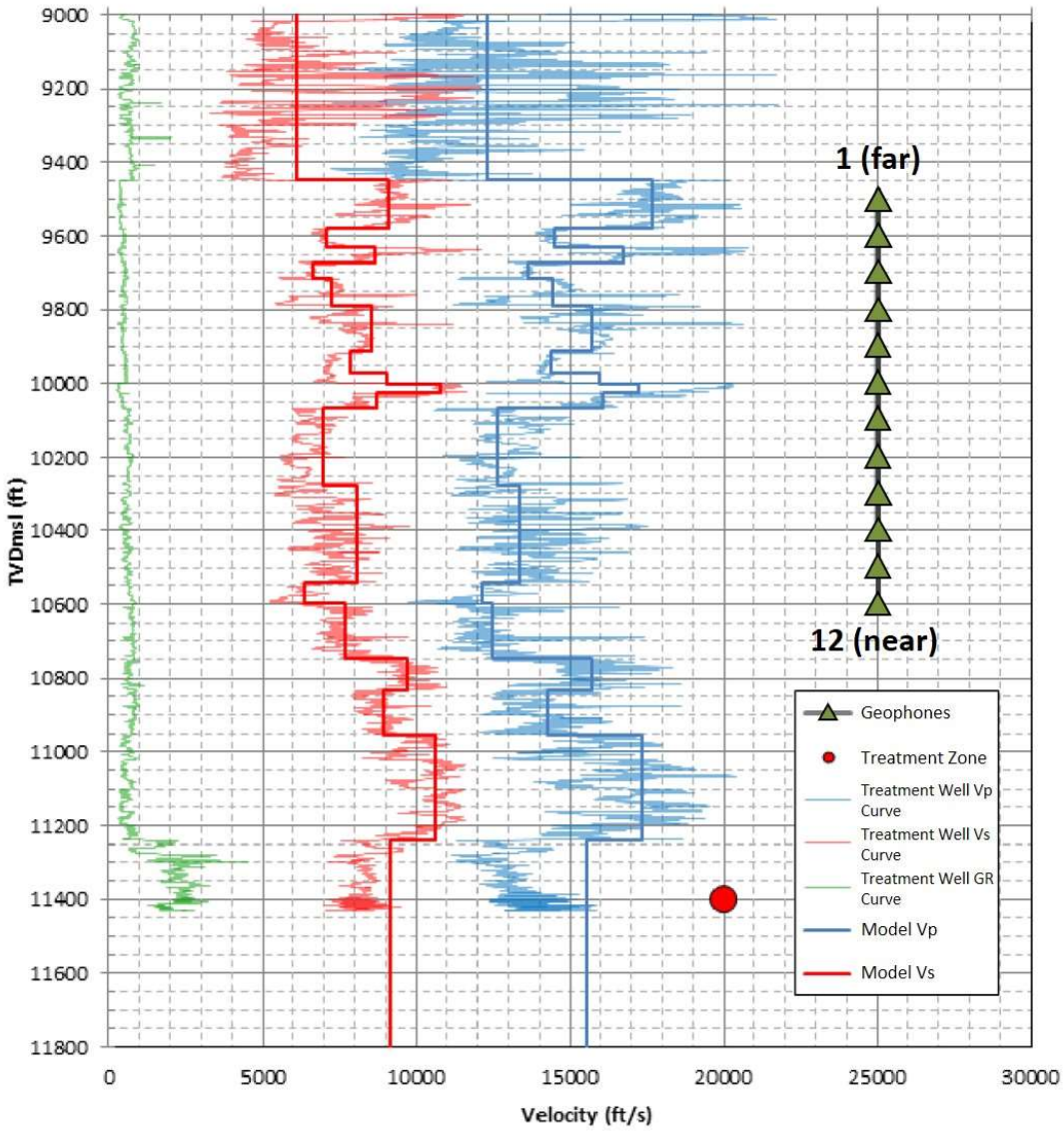

Figure 36. *Velocity model produced by the downhole vendor. All 12 geophones are placed according to their true depth location in the downhole array of the nearby monitor well, 600 ft. east of the treatment well (Modified from IMaGE Final Report, 2015).*

It was discovered that the top of the Chester Limestone is at around the placement of geophone 1 and the bottom of the Chester Limestone is at around the placement of geophone 12. Further analysis would have to be made to make substantial conclusions, but based on these observations, there may have been multiple scattering of waves and interbed multiples to have occurred within the Chester Limestone to have produced a

decrease in velocity from top to bottom of the formation. This could perhaps indicate a reason for the puzzling spectral ratio analysis on stages 6-11. The signals from those stages may have had to directly pass through that section, resulting in complex waveforms and an inability to separate the direct arrival from the head wave. Stage 12 however, may have just been close enough to geophone 12 to capture an adequate signal.

In the vendor's final report, it was also stated that the first arrival picks were very difficult to make out in the last half of the stages due to the high complexity of the compressional waves (Figure 37). This figure shows the seismograms for one of the stages. There are 12 sets of seismograms, one for each geophone, and they are numbered in order from top to bottom. As you can see from the circled area, the first arrivals are not obvious on the bottom sensors due to the high waveform complexity of the P-wave. The moveout is not consistent and the refracted arrival is arriving earlier. This results in the mispicking of arrivals. The far receivers show that the first arrivals are the direct arrivals, but then the moveout clearly changes further down the receivers. The arrows are pointing to where the true first arrivals are. This is in a way counter-intuitive because these are the sensors that are closest to the sources, so you would think the first arrival would be more obvious. These downhole signals have shown to be highly complex, due to an overlapping of head waves, superimposed late arrivals, noise, and different source signatures.

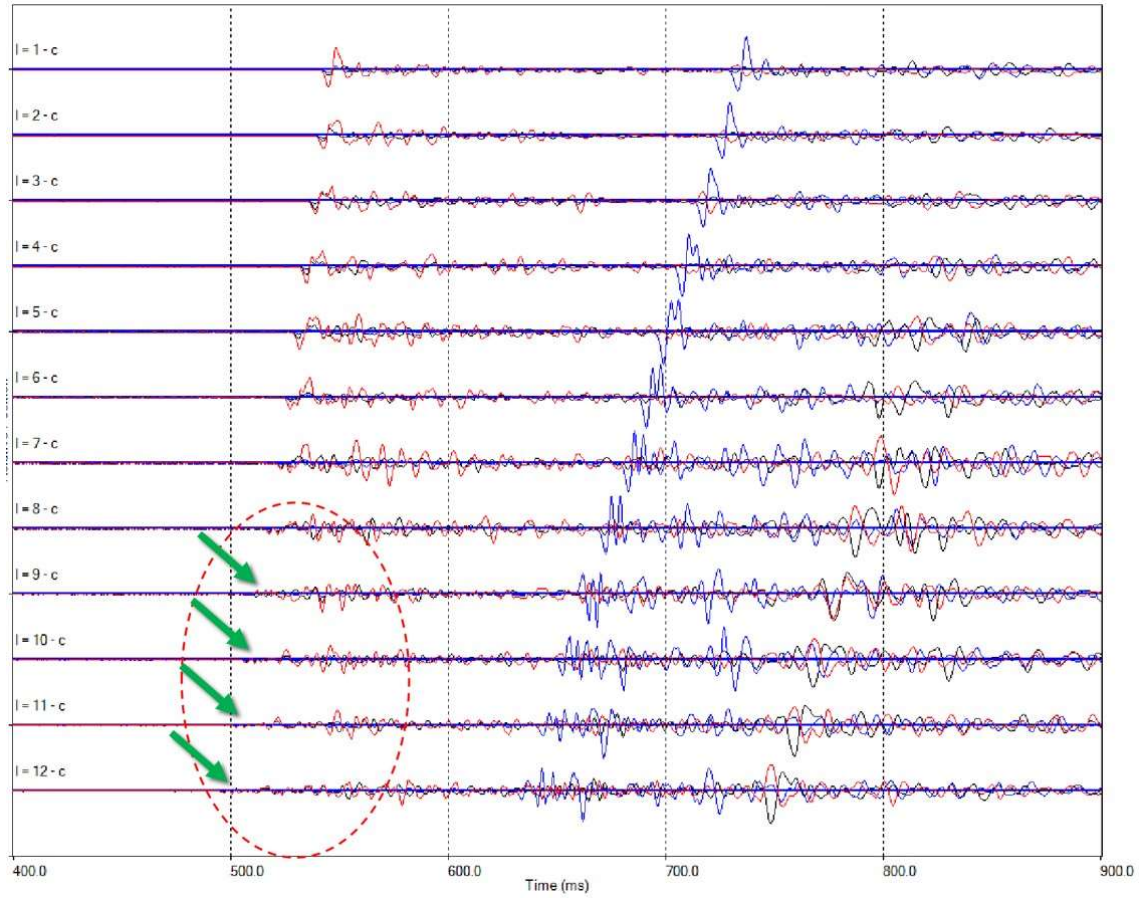

Figure 37. *This figure shows the seismograms for one of the stages. As you can see from the circled area, the first arrivals are not obvious on the bottom sensors due to the high waveform complexity of the P-wave. The arrows are pointing to where the true first arrivals are (Modified from IMaGE Final Report, 2015).*

Qualitative Interpretation of the Surface Signals

The next step was to analyze each downhole signal's co-identified surface event. This was done by making a qualitative interpretation based on the waveforms of each event, and comparing their amplitude spectrum with that of the downhole events. Figure 38 displays a surface signal and corresponding amplitude spectrum, showing the spectrum of the surface event, combined with the spectrum of its co-identified downhole event.

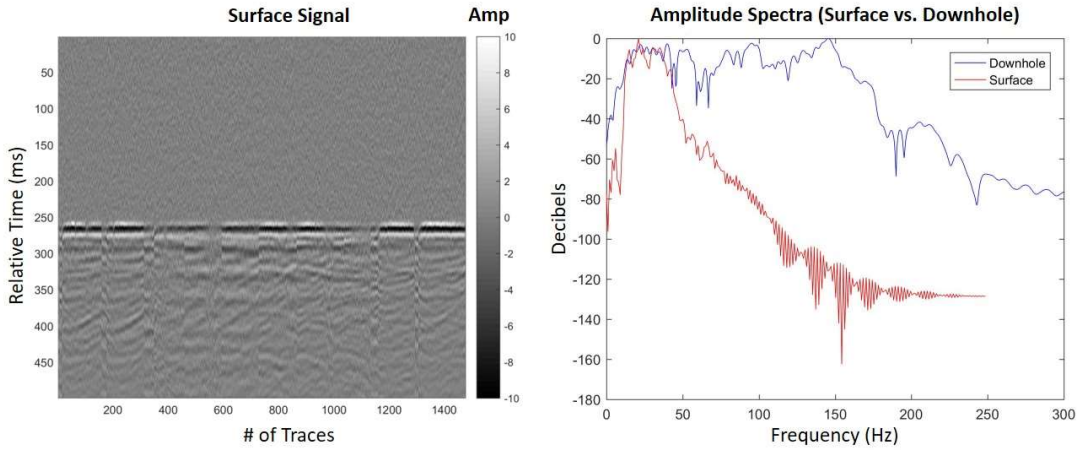

Figure 38. *Surface signal and corresponding amplitude spectrum of surface vs. downhole for stage 4. Notice how the surface spectrum captures a very limited range of low frequencies, while the downhole spectrum has a much broader range of frequencies.*

The downhole spectrum shown here is that of the near geophone. The surface spectrum was created by stacking all traces from the entire surface array of 1,476 geophones, like how the surface signal is plotted above. The absolute value of the Fourier transform was then performed on the resultant single trace, plotting its spectrum.

In Figure 38, the surface signal is very strong. This event is taken from stage 4, which is the stage containing the fault activation. This was the highest magnitude event captured from the surface array. Notice how the surface spectrum captures a very

limited range of low frequencies, while the downhole spectrum has a much broader range of frequencies, and even covers the lower frequencies that the surface array captures. All surface signals and corresponding downhole vs. surface amplitude spectrums are displayed in Appendix D. Compared to stage 4, the other surface signals appear to be very weak, which is what we expect of the surface array.

Results and Discussion

The highest SNR event per stage was used for analysis and a positive Q value was calculated between stages 1-5 and 12, whereas a negative Q value was calculated between stages 6-11. Due to the waveform complexity, it was challenging to obtain meaningful Q values for all events. Overall, the difficulty of the analysis attributes to the instability of the amplitude spectrum because Q is being estimated at small distances, and there is not much observable attenuation. The events from stages 6-11 showed to have unreasonable Q values, in that they were negative due to a positive slope produced from their amplitude ratios. These complex signals could be due to the overlying formation above the completed stages, where sources may have traveled through multiple paths to reach the sensors. Head waves may have traveled along the Woodford interface, which, based off Figure 36, is at around 11,200ft. From the direction in which the source travels, the Woodford boundary is a transition from slow to fast velocity, allowing these critically refracted or head waves to travel at a faster rate than the direct waves. In the earlier stages the direct arrival might be fast and reach the downhole sensors first, but once you move past a certain offset, the critically refracted waves are faster since they are travelling along the interface of the velocity of the faster layer, making the travel time shorter. These multipath waves produce late arrivals onto the signal, creating a complex signal that is too noisy for picking arrivals. The analysis however, provided insight into signal attenuation of microseismic events that are recorded using downhole and compared to surface arrays.

The negative Q values may also potentially indicate that those receivers lie along a nodal plane, due to the unexpected nature in character that the amplitude ratios are exhibiting compared to those with the positive Q values. Further evidence would have to indicate which stages lie on the compressional or tensional axes of the focal mechanism. A recommendation for future work would be to perform a focal mechanism interpretation on these events, and shear wave amplitude would be included in the interpretation.

Chapter 8: Conclusions

It is important to recognize the benefits and limitations of both surface and downhole acquisition geometries. In this case study, the use of both geometries provided a more complete interpretation using the horizontal location from the surface events and the depth from the downhole events.

The highest quality interpretation of microseismic event locations was demonstrated and discussed. The analysis and comparison of both microseismic datasets can serve as a template for interpretation of other jobs when only one modality is available. Determining the most accurate way to utilize both acquisition geometries will have implications on future development and vertical well placement.

This project also provided a detailed understanding of processing raw signals from microseismic events in the downhole array. I have shown that the complexity of the signal waveforms originating from microseismic events made it harder to put the events in the correct location in space. Also, a significant signal attenuation was seen in the downhole array and a comparison with the surface array shows similar results. This analysis could be useful for building an attenuation compensated velocity model during microseismic processing. Finally, even though the spectral ratio method provided only some physically plausible results, a lesson can be learned in finding new approaches for estimating attenuation, specifically for microseismic acquisitions when we only have a limited depth range to work with.

References

Aki, K., and P. G. Richards, 2002, Quantitative seismology, 2nd Ed.

Ammon, C. J., 2001, MATLAB Exercise Level 1: The Rotation of Vectors and Tensors, Department of Geosciences, Penn State University.

Badri, M., and H. M. Mooney, 1987, Q measurements from compressional seismic waves in unconsolidated sediments: Geophysics, **52**, 772-784.

Båth, B. M., 1974, Spectral analysis in geophysics: Development in Solid Earth Geophysics: Elsevier, **7**.

Bhattacharya, P., B. K. Chakrabarti, and D. Samanta, 2009, Fractal models of earthquake dynamics: Heinz Georg Schuster (ed) Reviews of Nonlinear Dynamics and Complexity, **2**, 107–158.

Blakey, R., 2016, Paleogeography: http://jan.ucc.nau.edu/~rcb7/index.html, (accessed March 4, 2017).

Boyd, D. T., 2008, Stratigraphic Guide to Oklahoma Oil and Gas Reservoirs: Oklahoma Geological Survey, University of Oklahoma.

Cabarcas, C., and O. Davogustto, 2013, The magnitude vs. distance plot–A tool for fault reactivation identification: AAPG Annual Convention and Exhibition, Pittsburgh, Pennsylvania.

Cardott, B. J., 2012, Thermal maturity of Woodford Shale gas and oil plays, Oklahoma, USA: International Journal of Coal Geology, **103**, 109-119.

Cheng, P., and G. F. Margrave, 2008, Complex spectral ratio method for Q estimation: CREWES Research Report, **20**, University of Calgary, Canada.

Grechka, V., P. Singh, and I. Das, 2011, Estimation of effective anisotropy simultaneously with locations of microseismic events: Geophysics, **76**, WC143-WC155.

Gutenberg, B., and C. F. Richter, 1942, Earthquake magnitude, intensity, energy, and acceleration: Bulletin of the Seismological Society of America, **32**, no.3, 163-191.

Haase, A. B., and R. R. Stewart, 2003, Q-factor estimation from borehole seismic data: Ross Lake, Saskatchewan: CREWES Research Report, **15**, 1-7.

Haase, A. B., and R. R. Stewart, 2004, Attenuation estimates from VSP and log data: SEG Technical Program Expanded Abstracts 2004, 2497-2500.

Igonin, N., and D. W. Eaton, 2016, On the origin of focal-depth discrepancies between ISM and MS monitoring: Microseismic Industry Consortium, **7**, Chapter 30, 325-330.

IMaGE (ITASCA Microseismic and Geomechanical Evaluation), 2015, XXXXXXXX* Microseismic Reprocessing Results. Retrieved from IMaGE.

Johnson, K. S., and K. V. Luza, 2008, Earth Science and Minerals Resources of Oklahoma: Educational Publication 9, Oklahoma Geological Survey, 1-21.

Kidney, R. L., U. Zimmer, and N. Boroumand, 2010, Impact of distance-dependent location dispersion error on interpretation of microseismic event distributions: The Leading Edge, **29**, 284-289.

Kratz, M., A. Aulia, and A. Hill, 2013, Identifying fault activation in shale reservoirs using microseismic monitoring during hydraulic stimulation: source mechanisms, b values, and energy release rates: Geohorizons, **37**, no.6, xx-yy.

Kulhanek, O., 2005, Seminar on b-value: Dept. of Geophysics, Charles University, Prague, 10-190.

Kvale, E. P., and J. Bynum, 2014, Regional Upwelling During Late Devonian Woodford Deposition in Oklahoma and Its Influence on Hydrocarbon Production and Well Completion: AAPG Annual Meeting, AAPG Search and Discovery.

Lowe, T., M. Potts, and D. Wood, 2013, A Case History of Comprehensive Hydraulic Fracturing Monitoring in the Cana Woodford: SPE Annual Technical Conference and Exhibition, SPE 166295.

Margrave, G. F., 2017, Seismic attenuation measures from VSP data by two different methods: 87th Annual International Meeting of the SEG, Expanded Abstracts, 5994-5998.

Maxwell, S., 2009, Confidence and accuracy of microseismic images, CSPG CSEG CWLS Convention Abstracts, 480–483.

Maxwell, S., 2009, Microseismic location uncertainty, CSEG Recorder, **34**, 41-46.

Maxwell, S. C., M. Jones, R. Parker, S. Miong, S. Leaney, D. Dorval, D. D'Amico, J. Logel, E. Anderson, and K. Hammermaster, 2009, Fault activation during hydraulic fracturing: 79th Annual International Meeting of the SEG, Expanded Abstracts, 1552-1556.

Maxwell S., 2014, Microseismic imaging of hydraulic fracturing: Improved engineering of unconventional reservoirs: SEG.

MicroSeismic, Inc., 2013, Devon Energy Corporation XXXXXXXX* Final Report. Retrieved from MicroSeismic, Inc.

Rich, J., B. Kennedy, and K. Rohan, 2016, A Woodford case study comparing high-quality surface and downhole microseismic locations: 86th Annual International Meeting of the SEG, Expanded Abstracts, 2662-2666.

Schorlemmer, D., S. Wiemer, and M. Wyss, 2005, Variations in earthquake-size distribution across different stress regimes: Nature, **437**, 539-542.

Thornton, M., and P. Duncan, 2012, Microseismic imaging with combined surface and downhole arrays: 82nd Annual International Meeting of the SEG, Expanded Abstracts, 1-5.

Tonn, R., 1989, Comparison of seven methods for the computation of Q: Physics of the Earth and Planetary Interiors, **55**, no.3-4, 259-268.

Urbancic, T., A. Wuestefeld, and A. Baig, 2013, Black Box Recording of Passive Seismicity: Pitfalls of not Understanding your Acquisition Instrumentation and its Limitations: Integration geoConvention, Calgary, Canada.

Verma, S., O. Mutlu, and K. J. Marfurt, 2013, Seismic modeling evaluation of fault illumination in the Woodford Shale: 83rd Annual International Meeting of the SEG, Expanded Abstracts 2013, 3310-3314.

Viegas, G., A. Baig, W. Coulter, and T. Urbancic, 2012, Effective monitoring of reservoir-induced seismicity utilizing integrated surface and downhole seismic networks: First Break, **30**, 77–81.

Wheaton, B., J. Miskimins, D. Wood, T. Lowe, and R. Barree, 2015, Integration of Distributed Temperature and Distributed Acoustic Survey Results with Hydraulic Fracture Modeling: A Case Study in the Woodford Shale: 85th Annual International Meeting of the SEG, Expanded Abstracts, 4926-4927.

*Well Name withheld for confidentiality.

Appendix A: Vector Rotation of Downhole Signals for All 12 Events

The following images show the original X and Y components and corresponding vector-rotated radial and tangential components of the highest SNR event of each of the 12 stages. Vector rotation was applied only to the traces recorded from geophone 1 (farthest geophone from the source) and geophone 12 (nearest geophone to the source).

Stage 1:

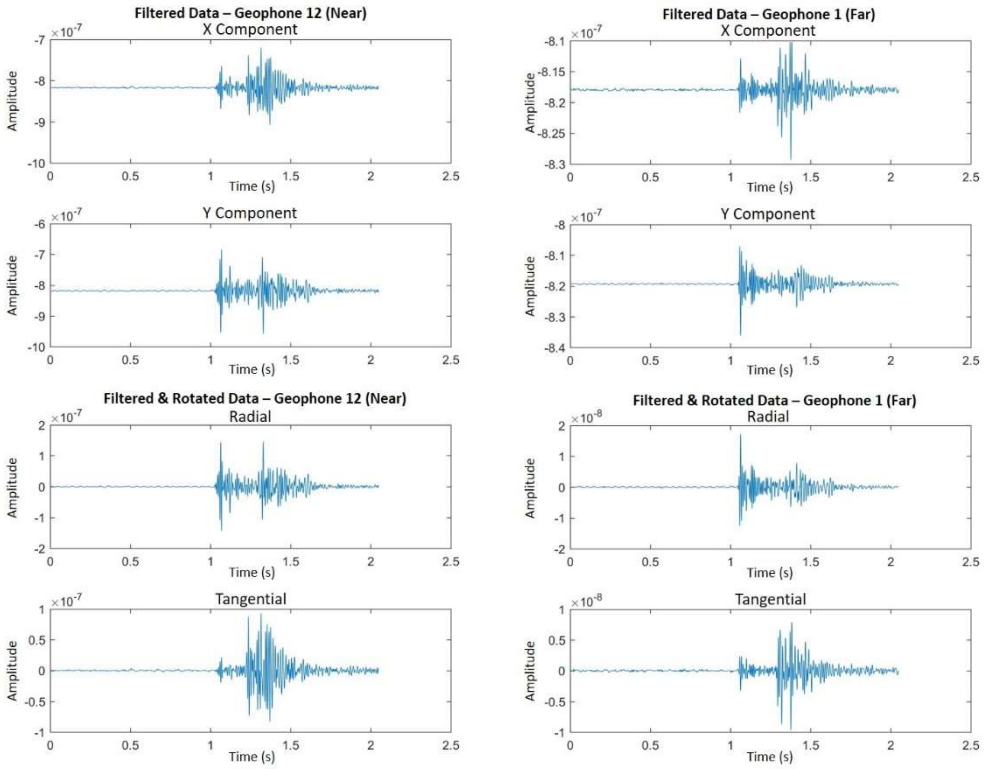

Stage 2:

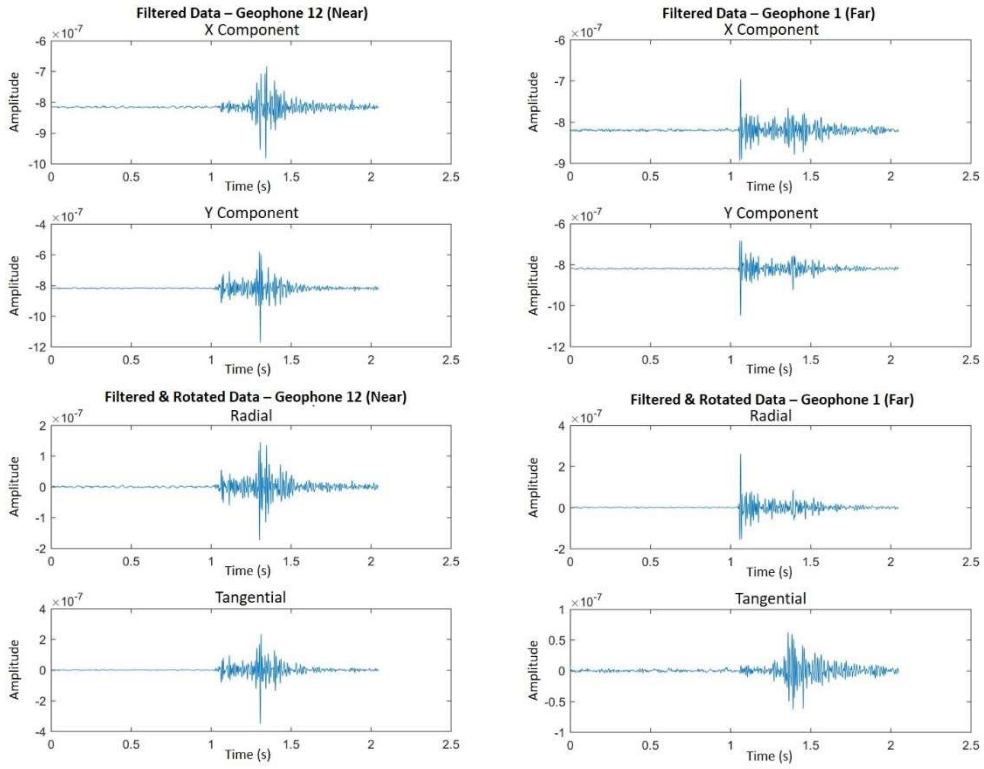

Stage 3:

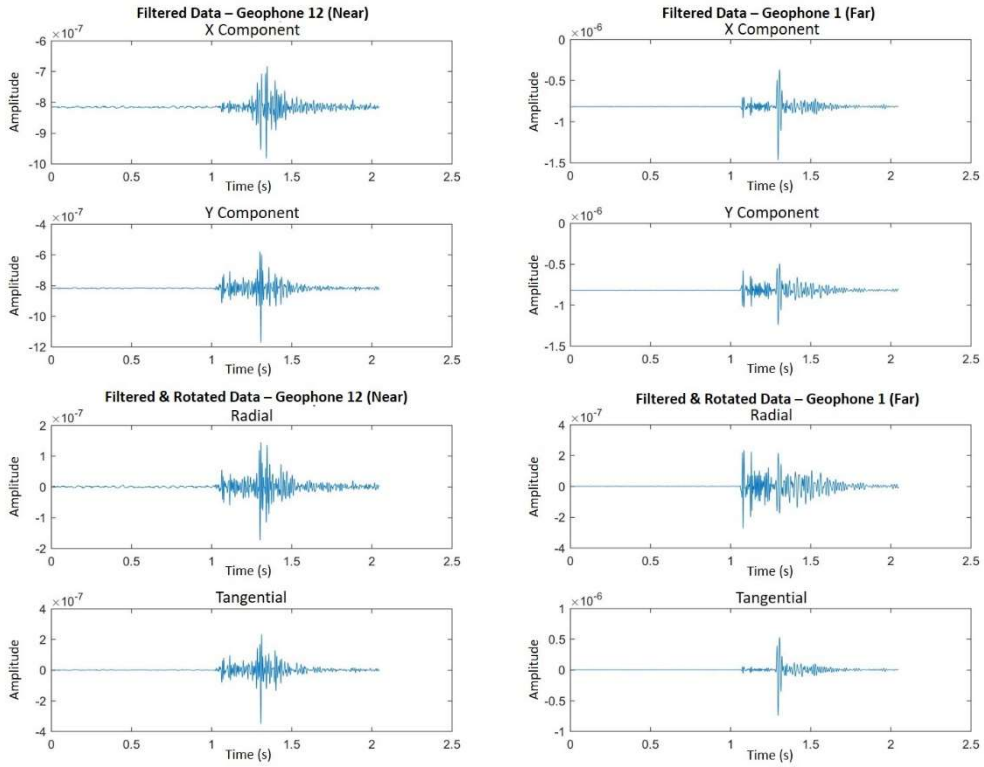

Stage 4:

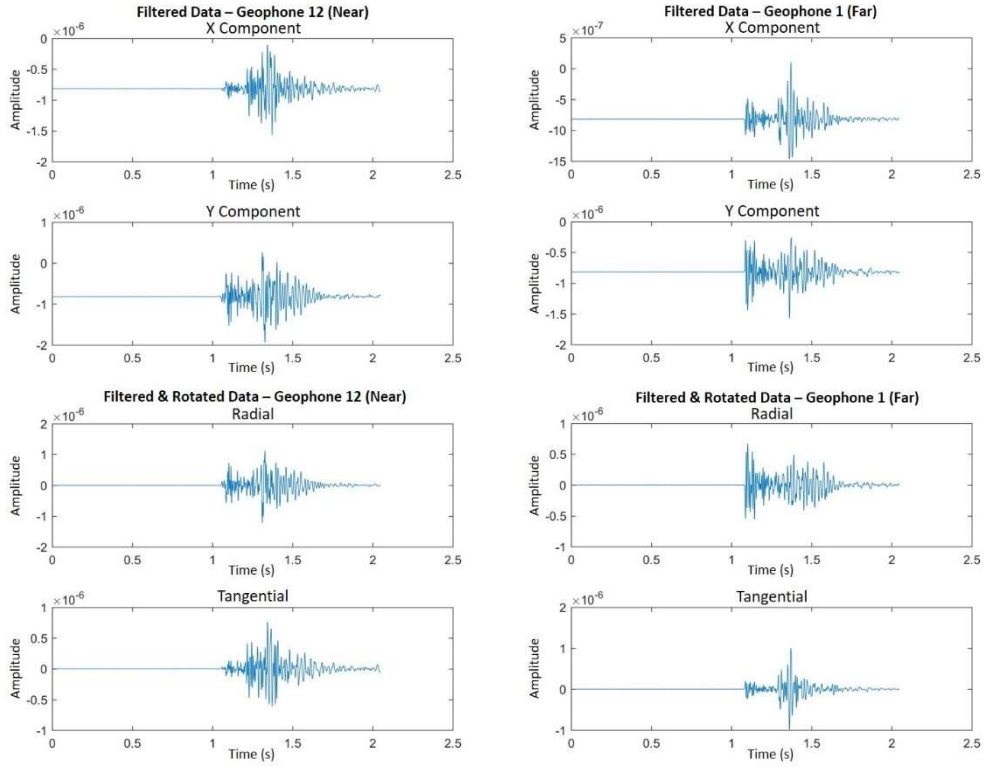

Stage 5:

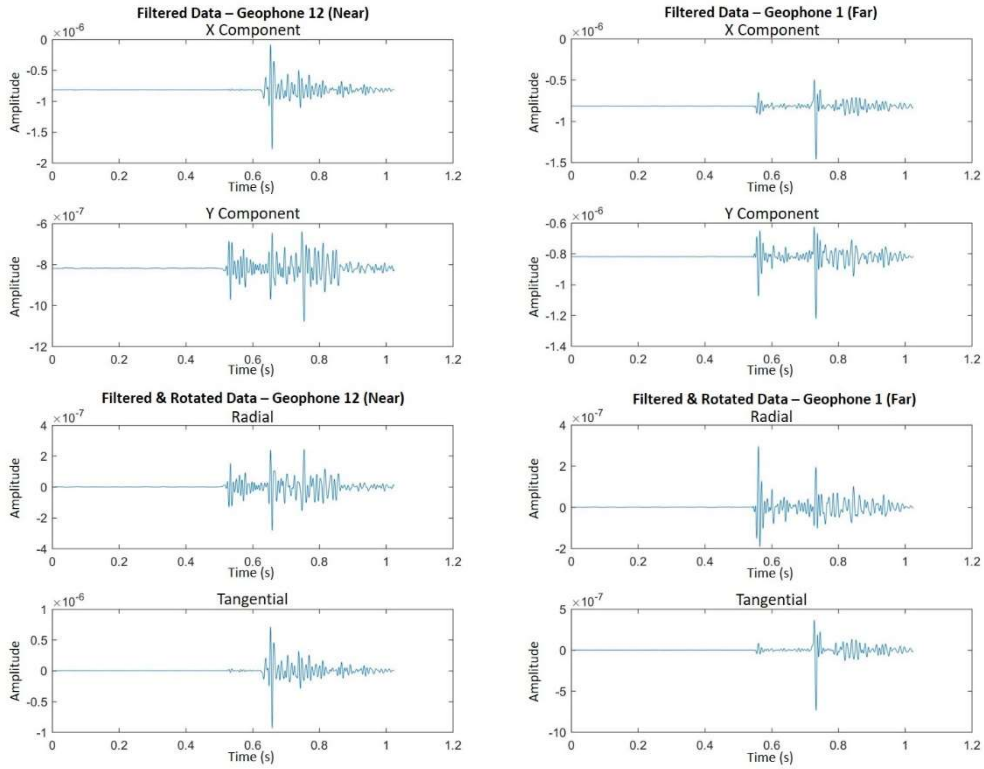

Stage 6:

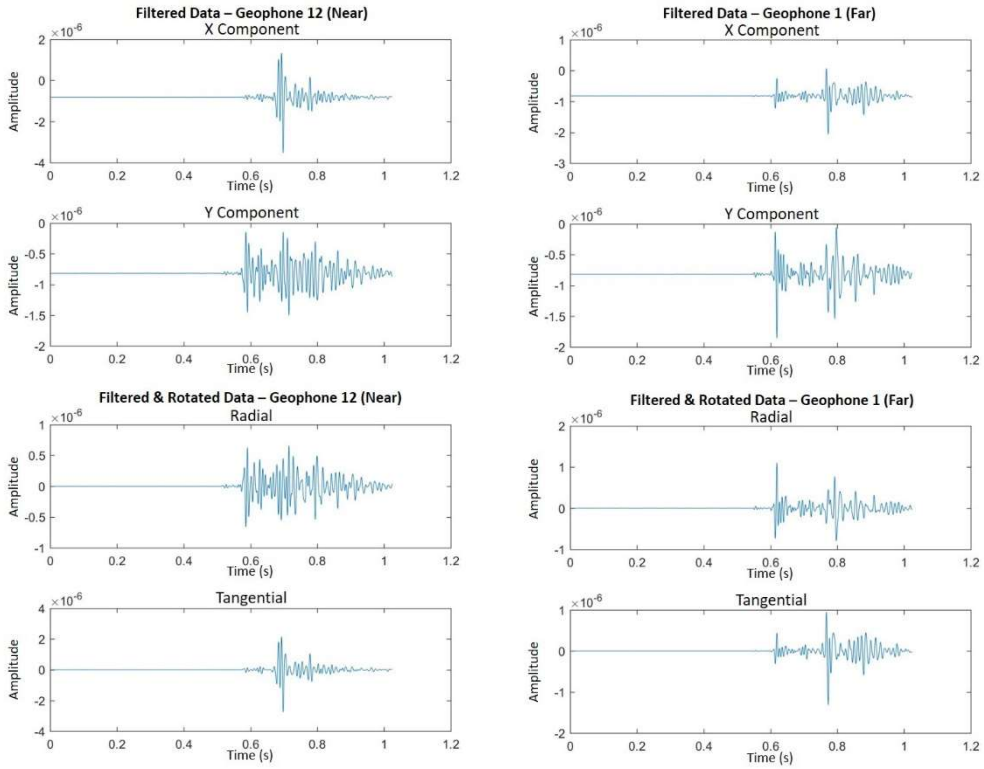

Stage 7:

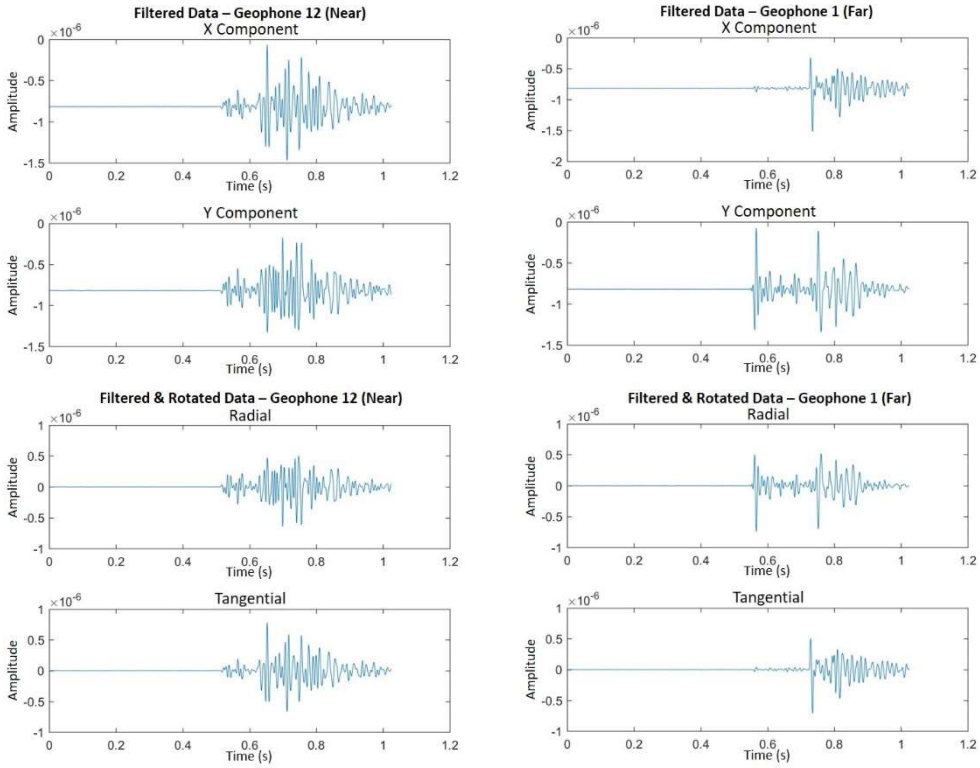

Stage 8:

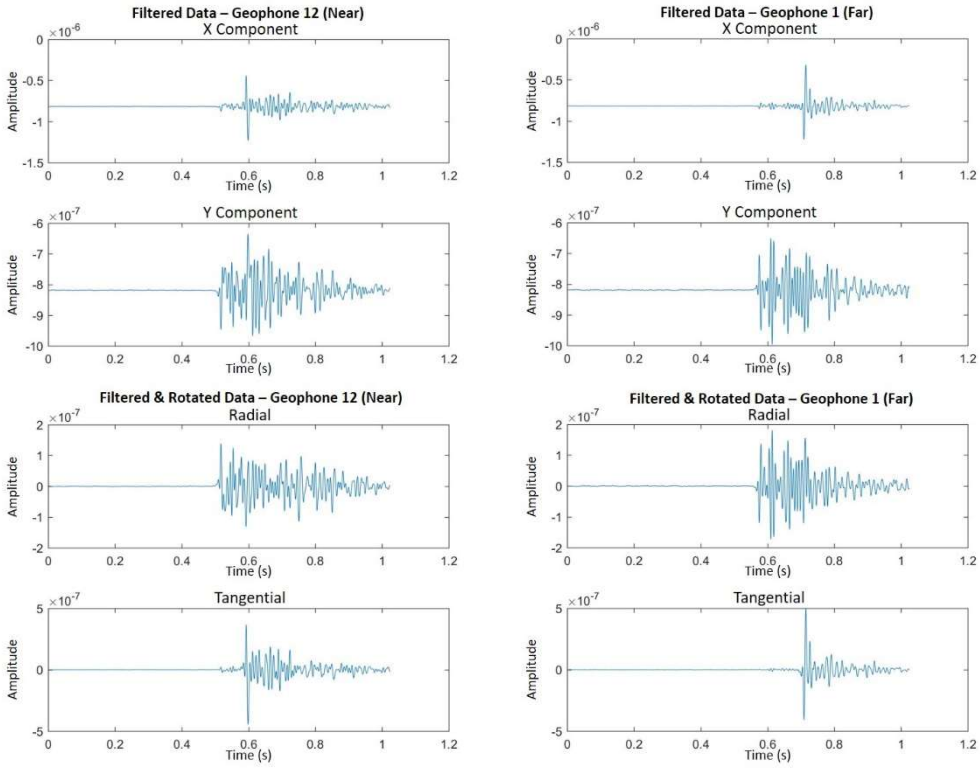

Stage 9:

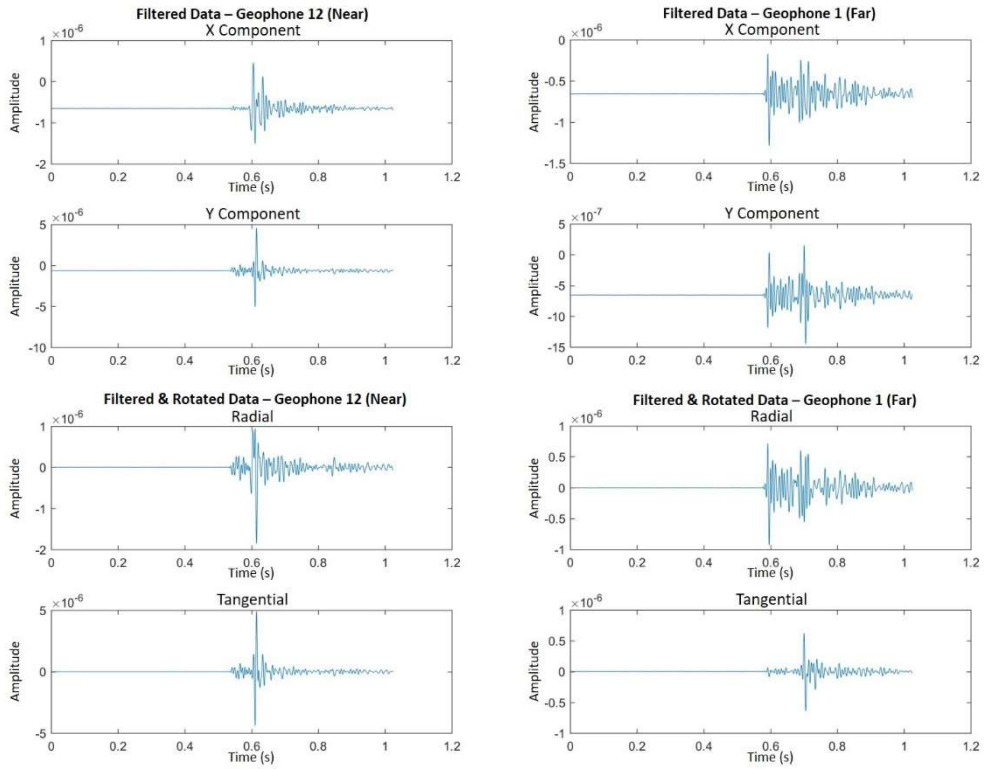

Stage 10:

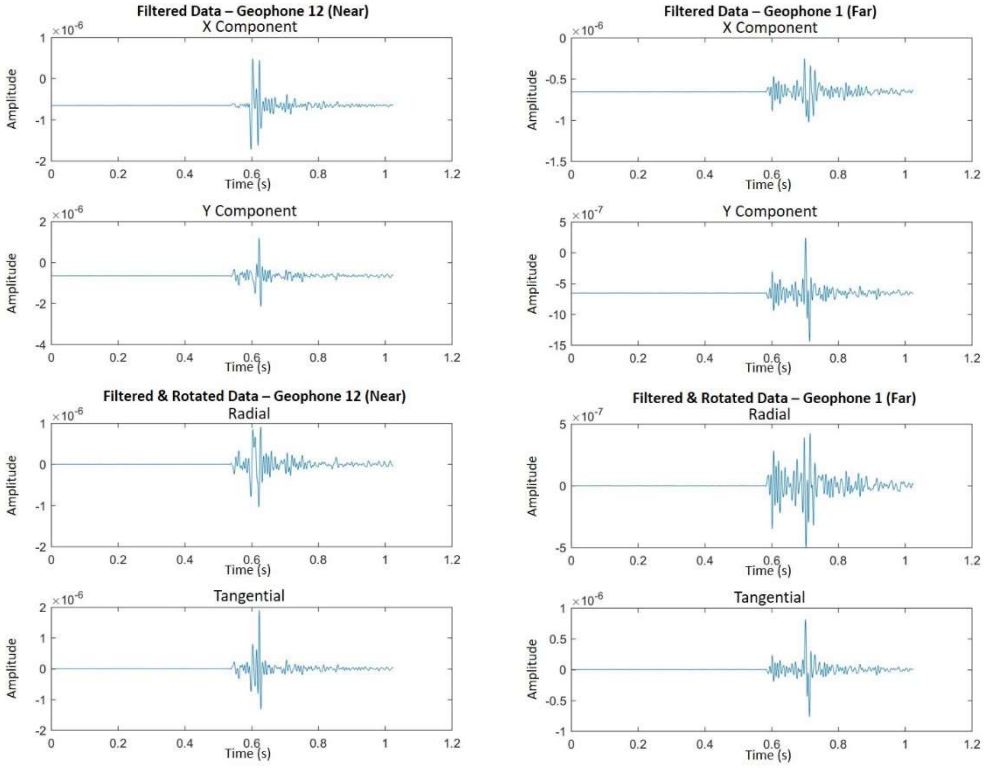

Stage 11:

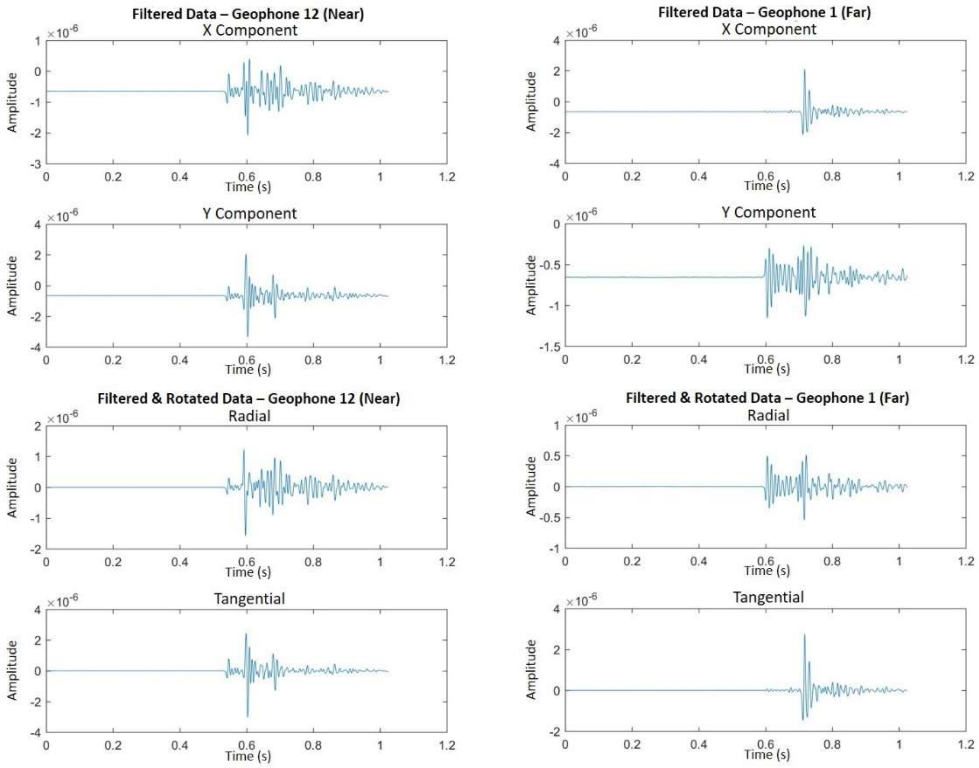

Stage 12:

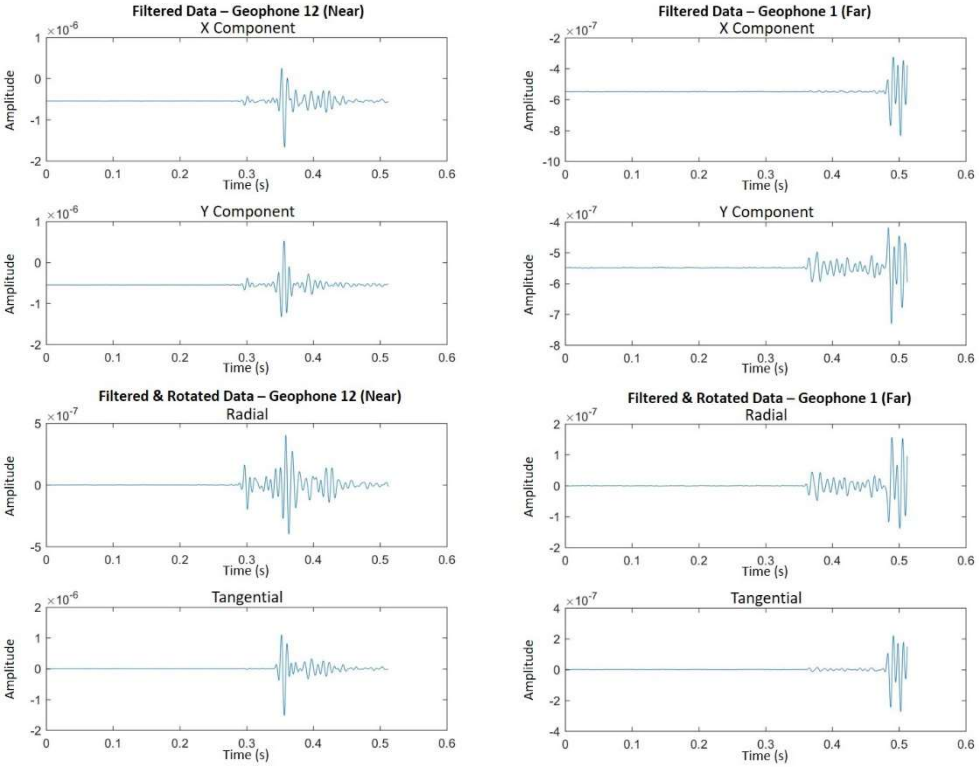

Appendix B: Downhole Signals with Mutes for All 12 Events

The downhole signals are shown below, each with their corresponding mute superimposed on top. This is done to show what all is being taken out from the signal, and the direct P-wave arrival that will eventually be left behind to use for the spectral ratio analysis. The mutes were performed on the vector-rotated radial components because these were the waveforms that showed the highest P-wave response.

Stage 1:

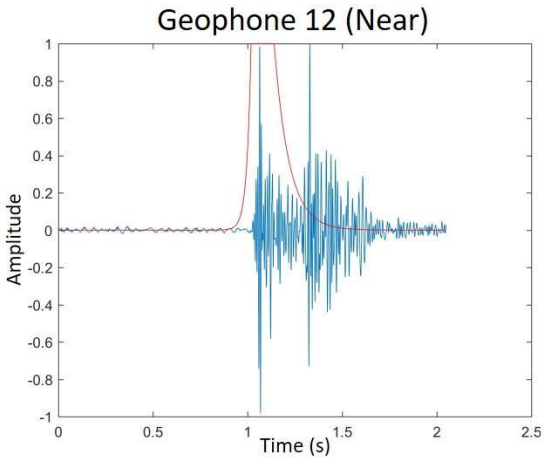

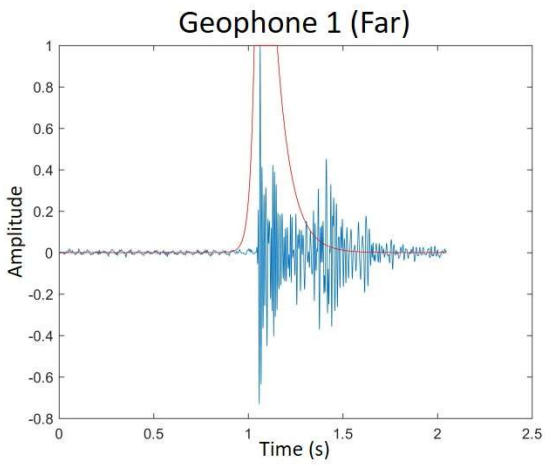

Stage 2:

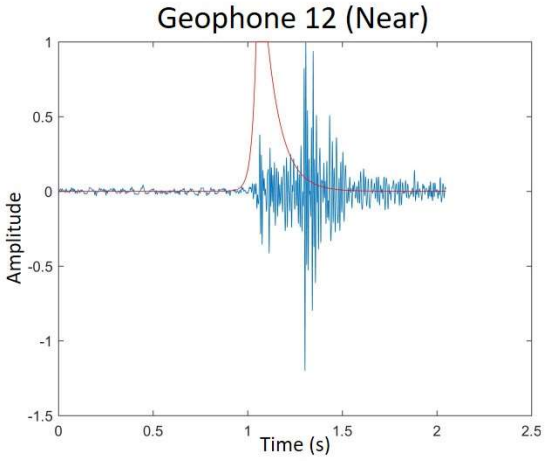

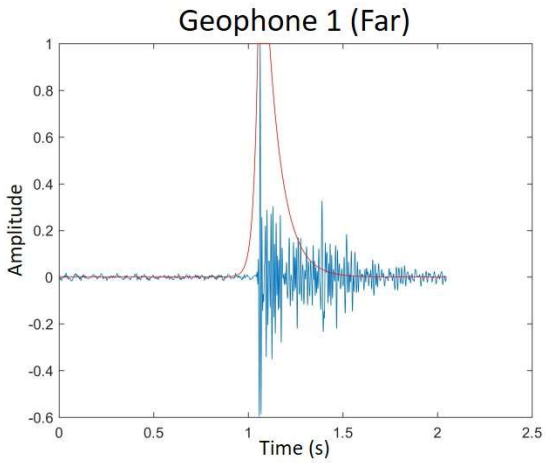

Stage 3:

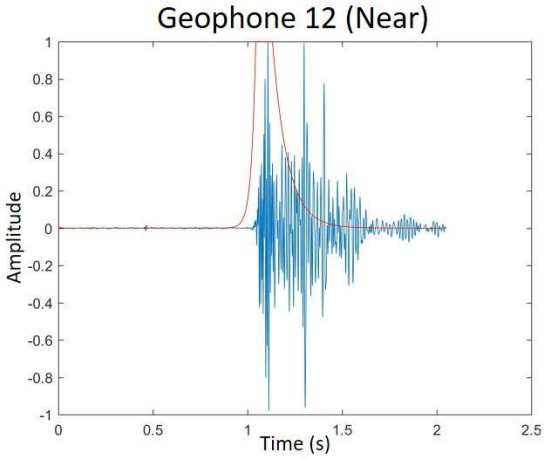

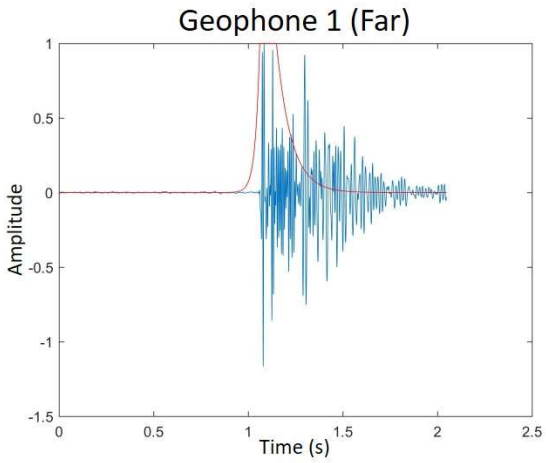

Stage 4:

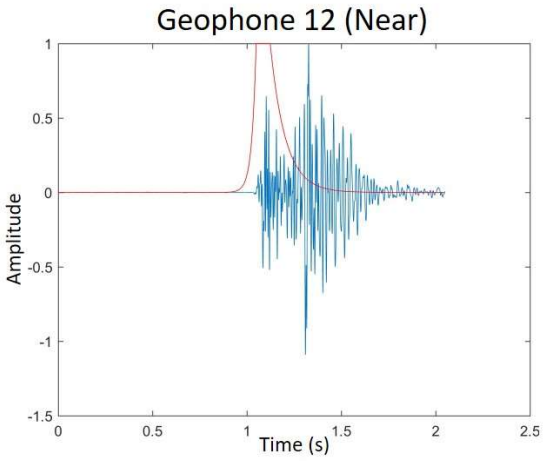

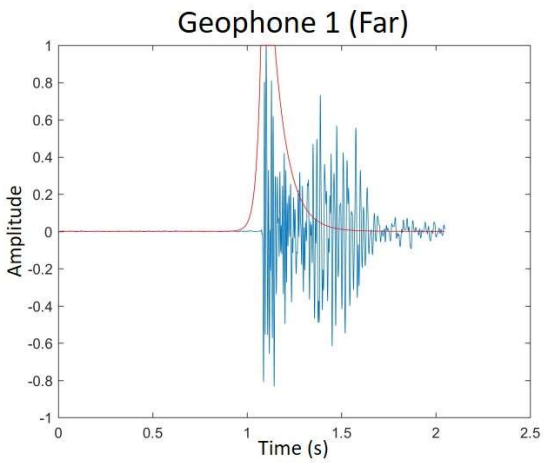

Stage 5:

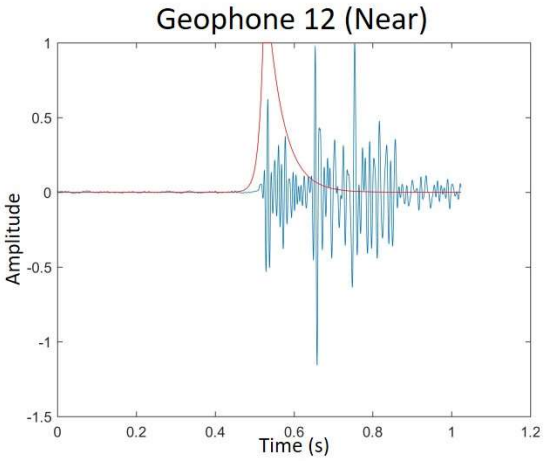

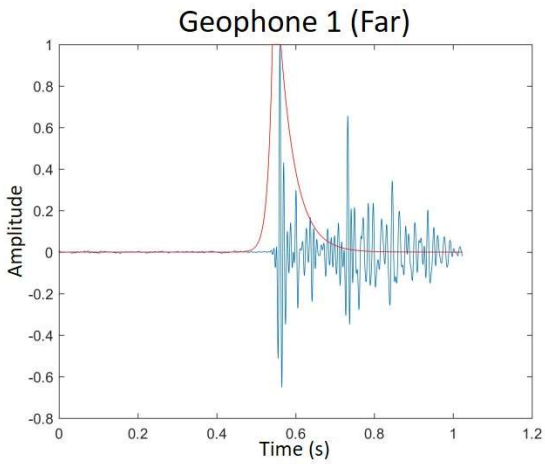

Stage 6:

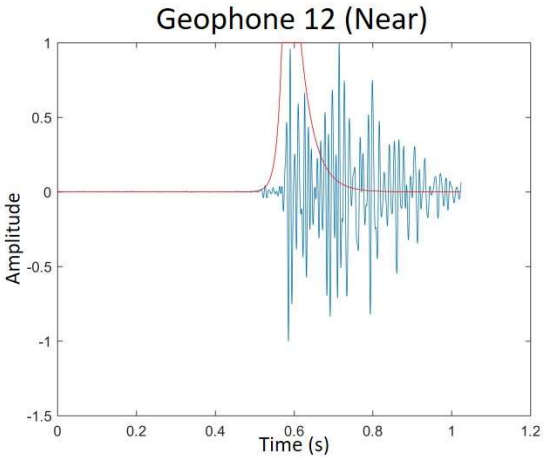

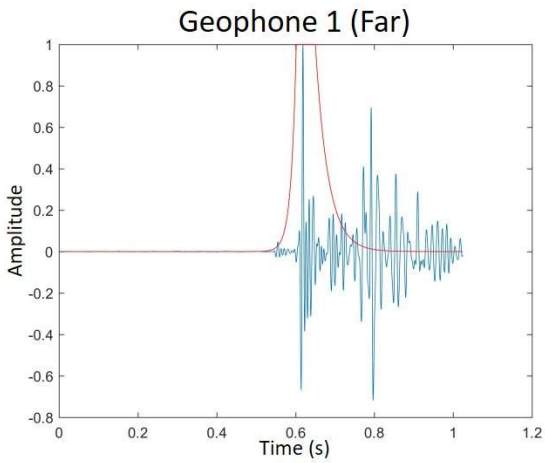

Stage 7:

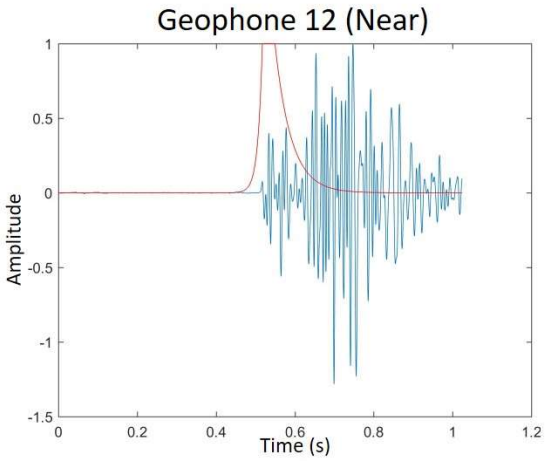

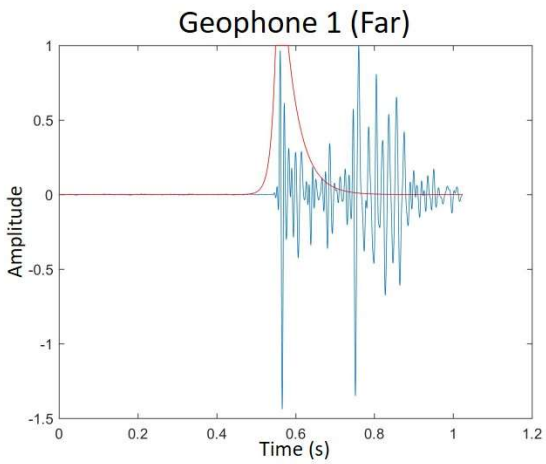

Stage 8:

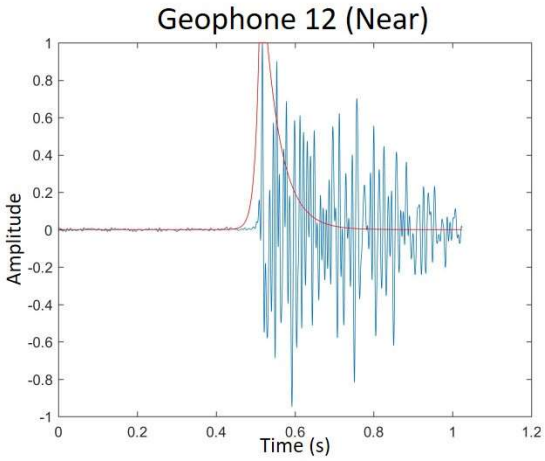

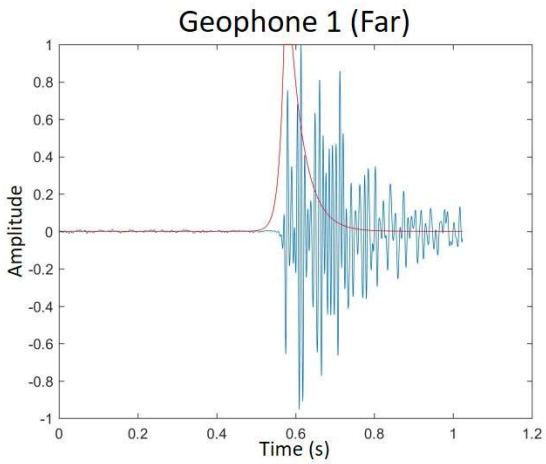

Stage 9:

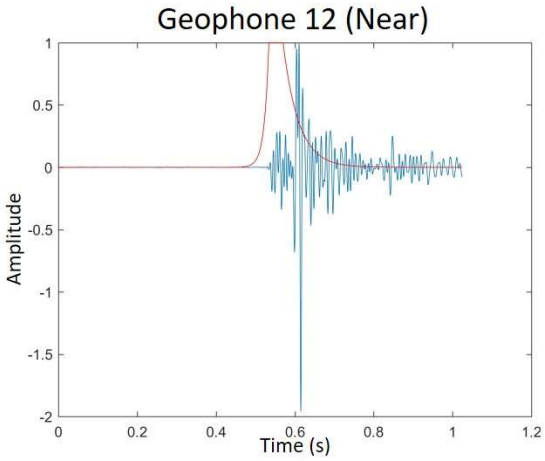

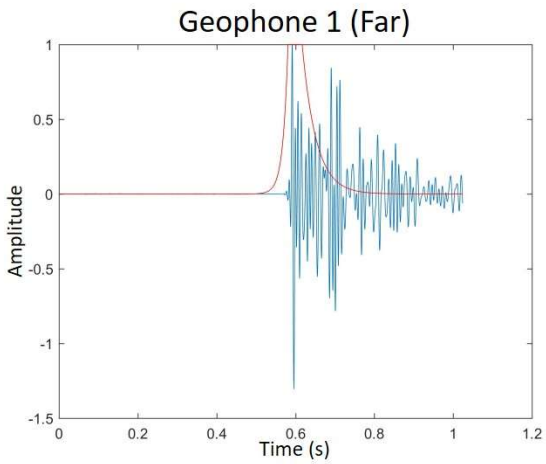

Stage 10:

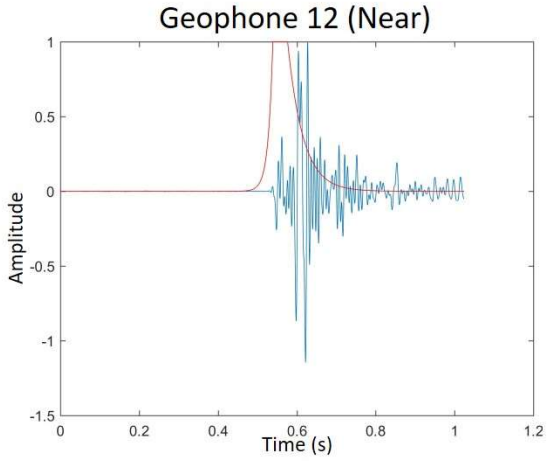

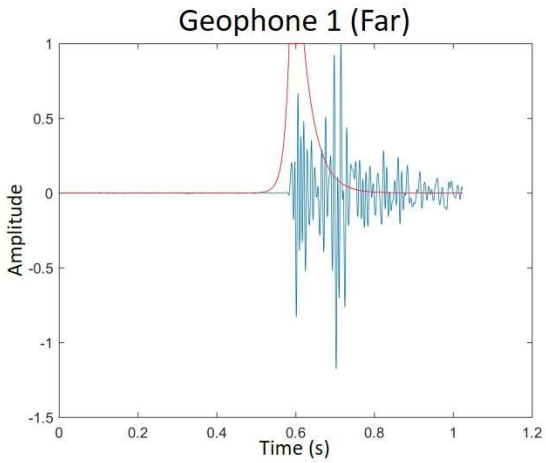

Stage 11:

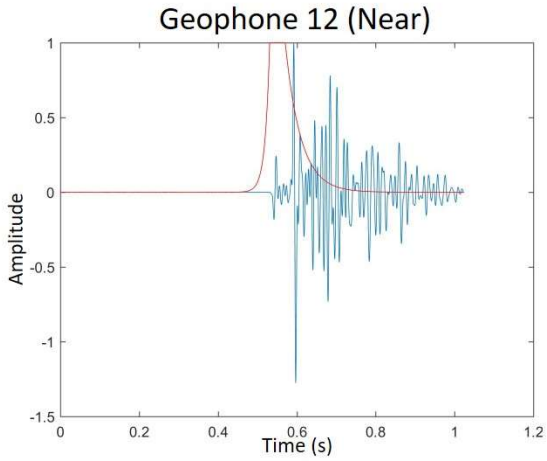

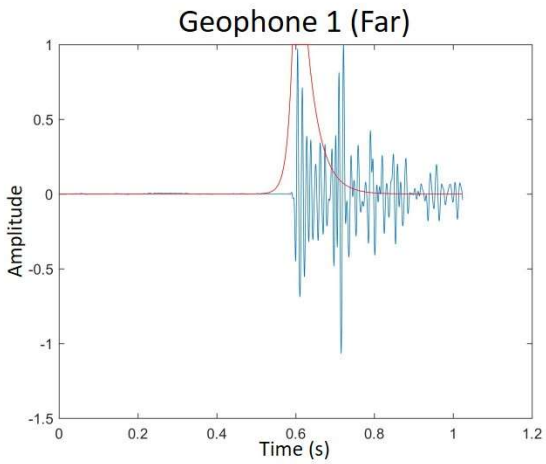

Stage 12:

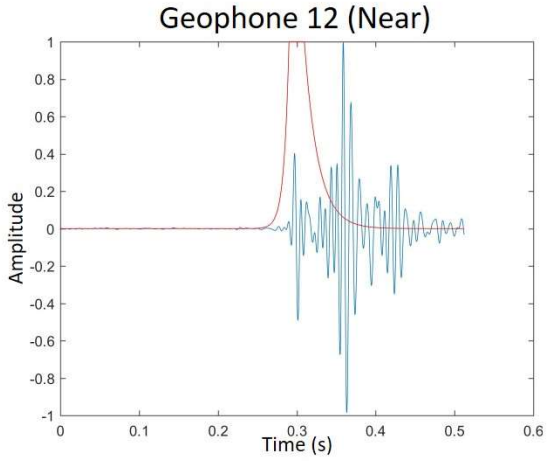

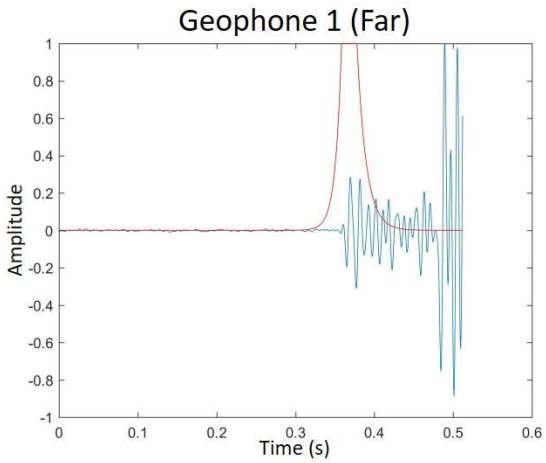

Appendix C: Amplitude Spectra of Downhole Signals and Resultant Amplitude Ratio for All 12 Events

The following images show the amplitude spectrums between every near geophone (geophone 12) and every far geophone (geophone 1) of all 12 stages. Their corresponding amplitude ratios with line of best fit is plotted to the right of them.

Stage 1:

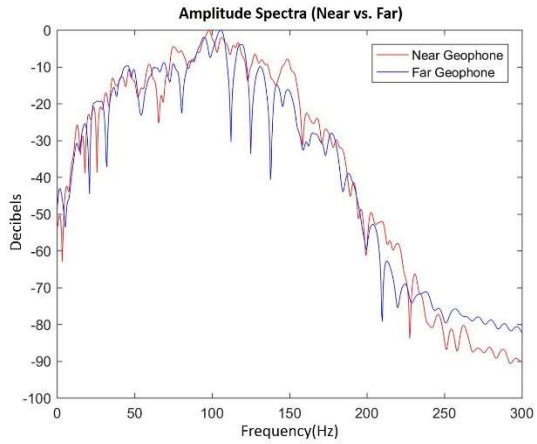

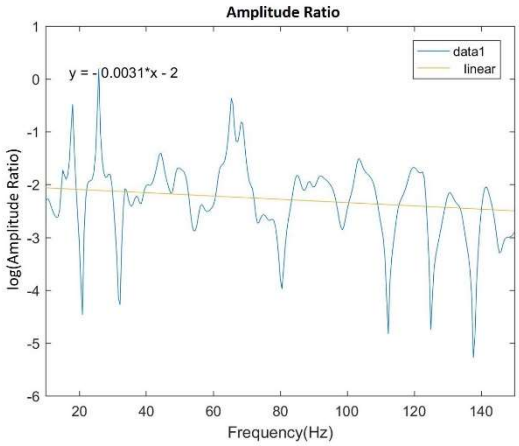

Stage 2:

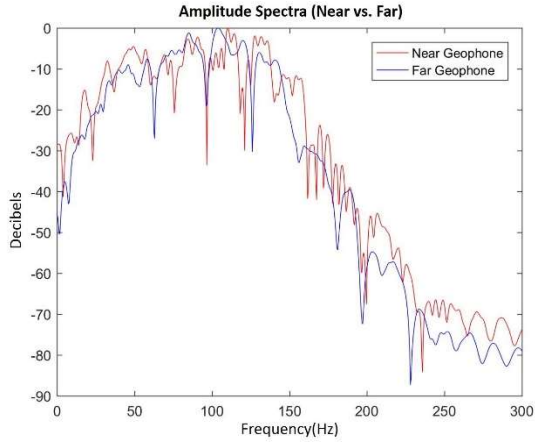

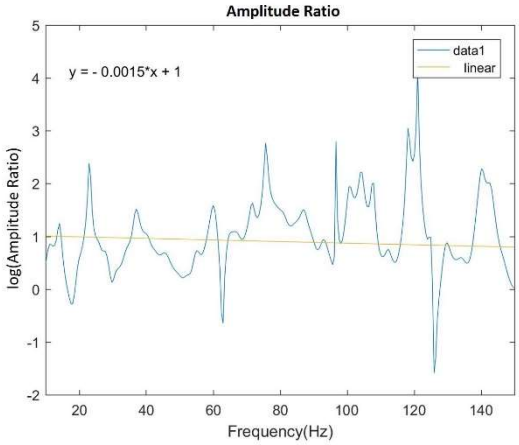

Stage 3:

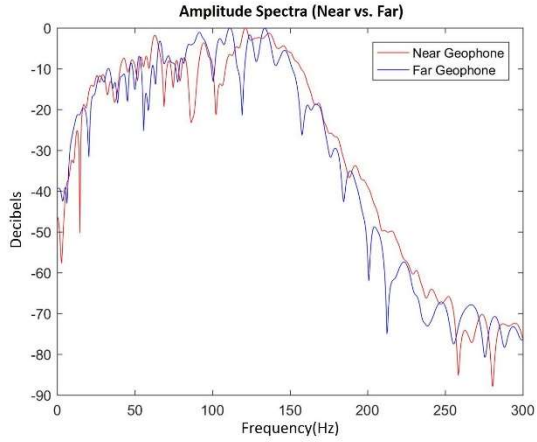

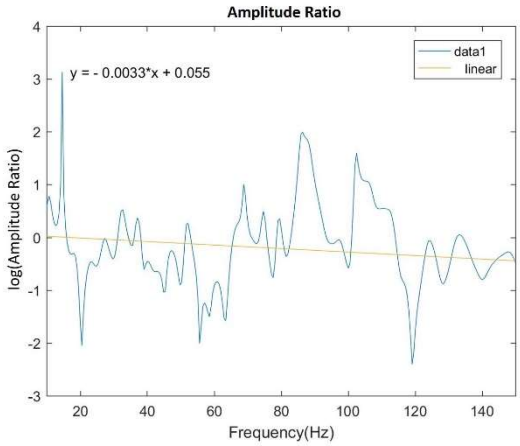

Stage 4:

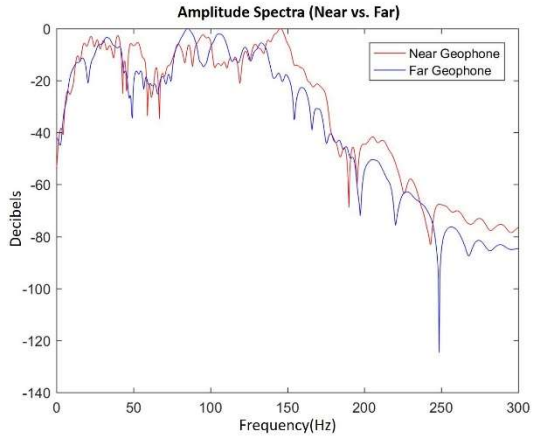

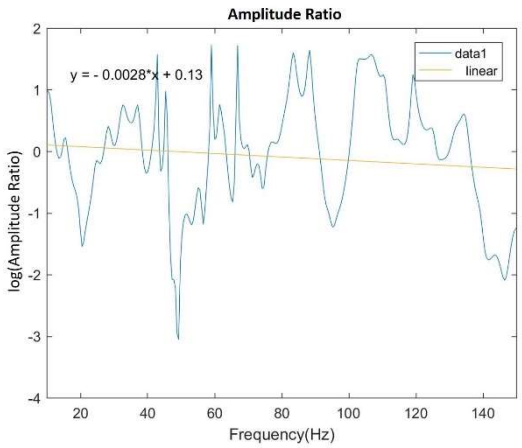

Stage 5:

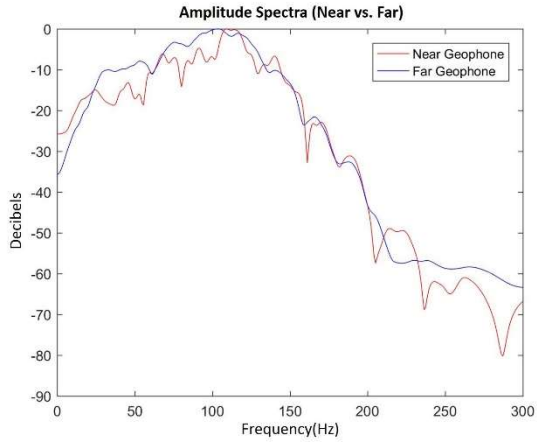

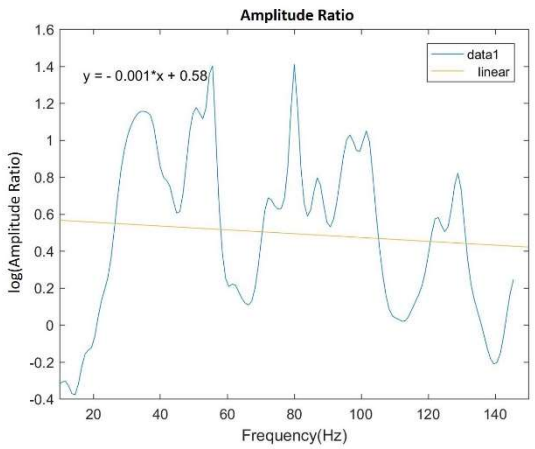

Stage 6:

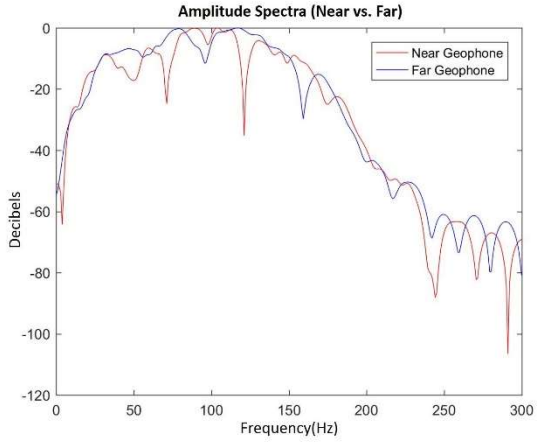

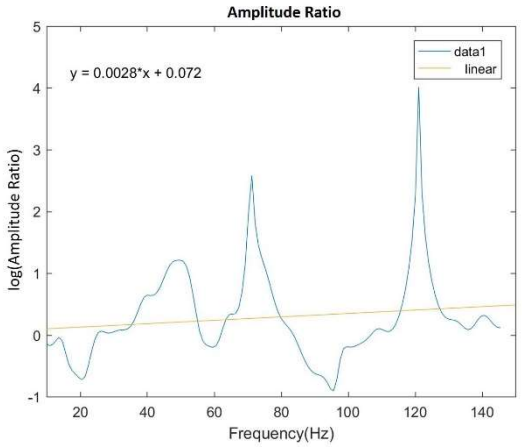

Stage 7:

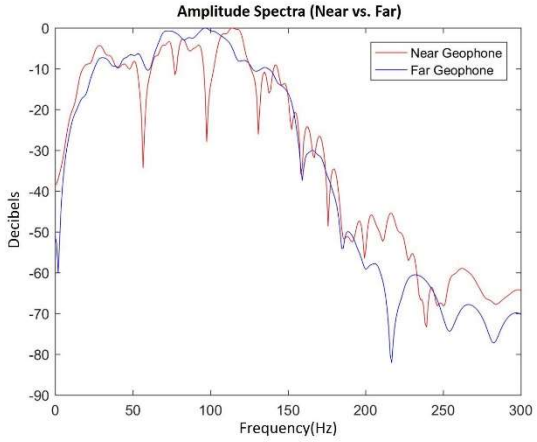

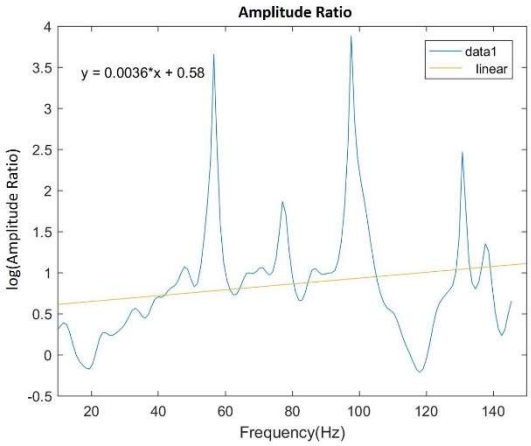

Stage 8:

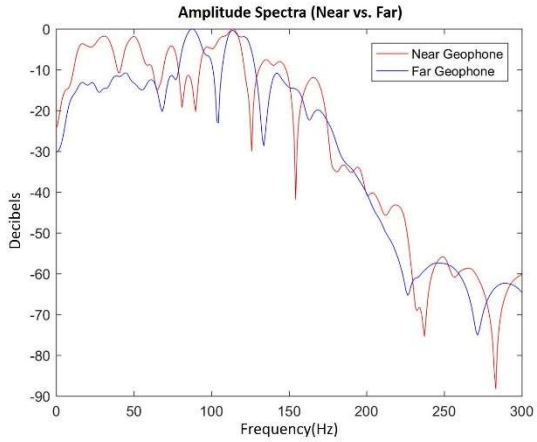

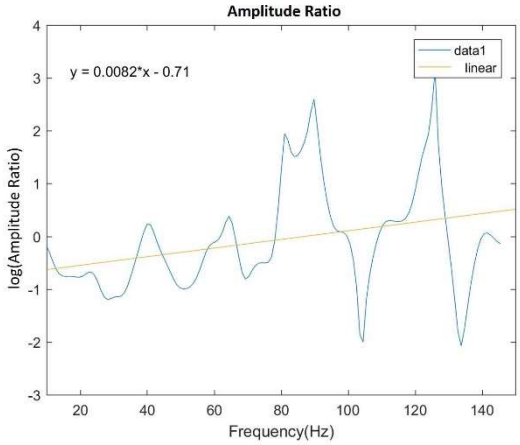

Stage 9:

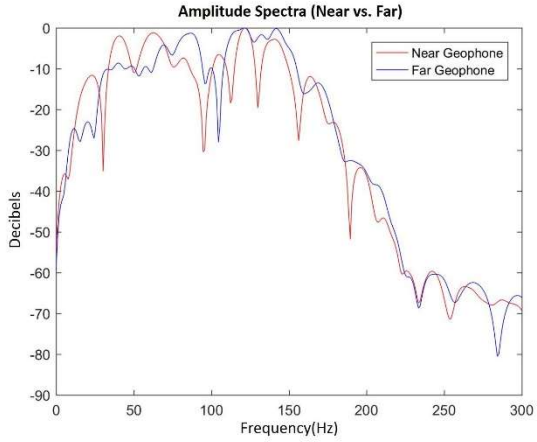

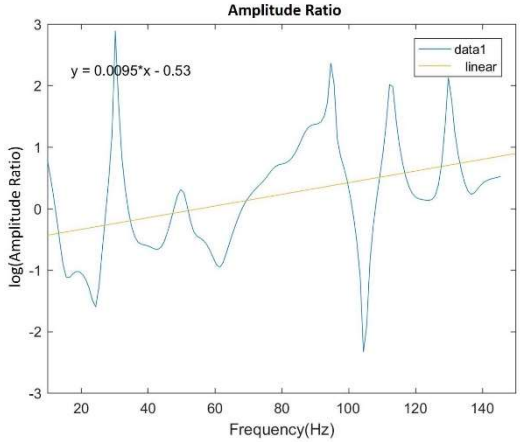

Stage 10:

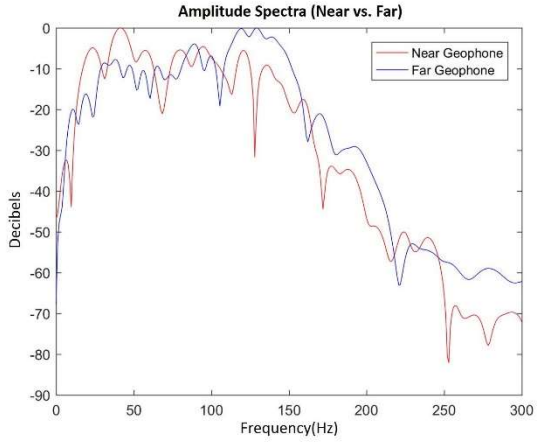

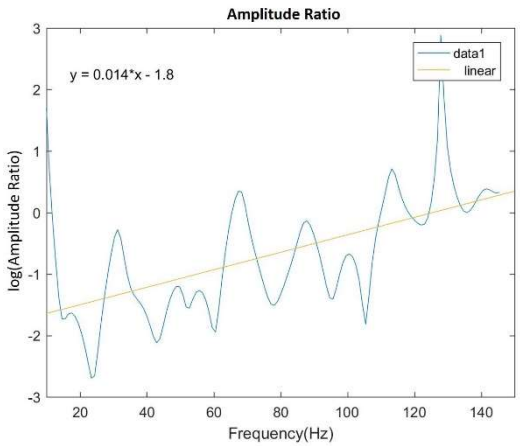

Stage 11:

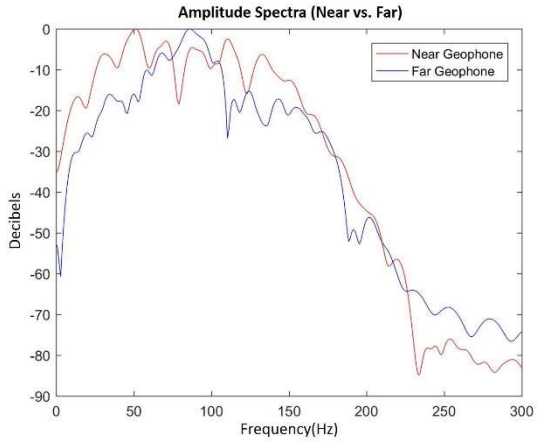

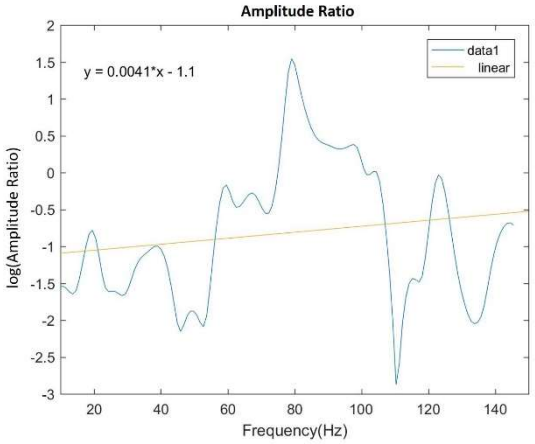

Stage 12:

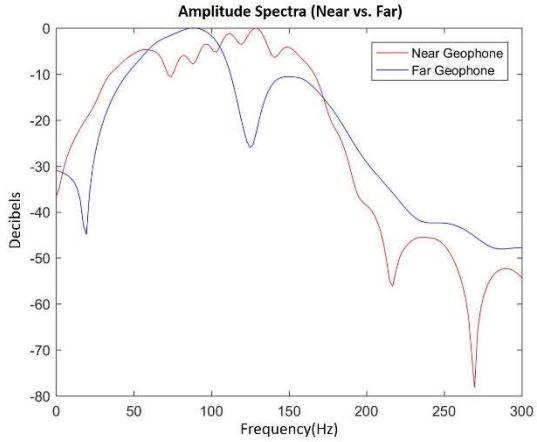

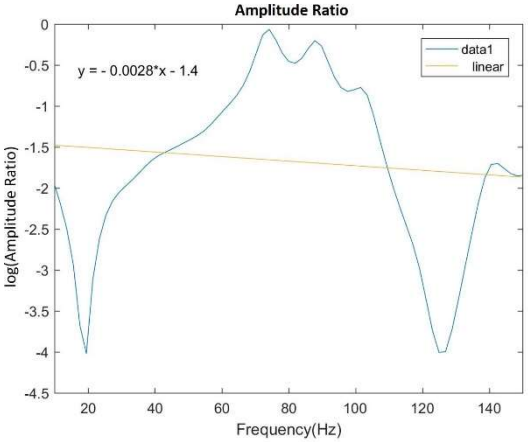

Appendix D: Surface Signals and Surface vs. Downhole Amplitude Spectra for all 12 Events

The surface signals are shown below, plotted as a single gather from all ten arms of the surface array, with NMO applied. Their corresponding amplitude spectrum is shown combined with the spectrum of its co-identified downhole event. The downhole spectrums are that of the near geophone from the downhole array. The surface spectrum was derived from a stacked trace of all surface array geophones.

Stage 1:

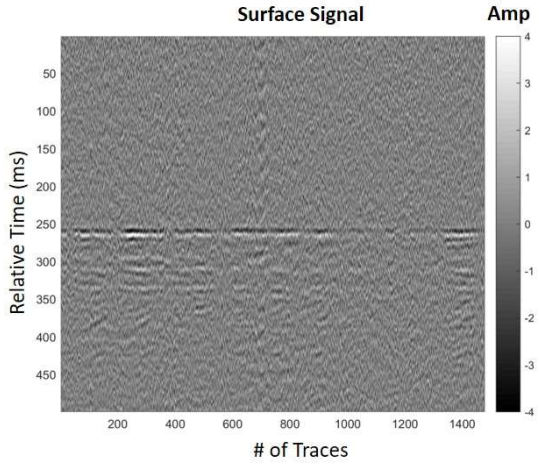

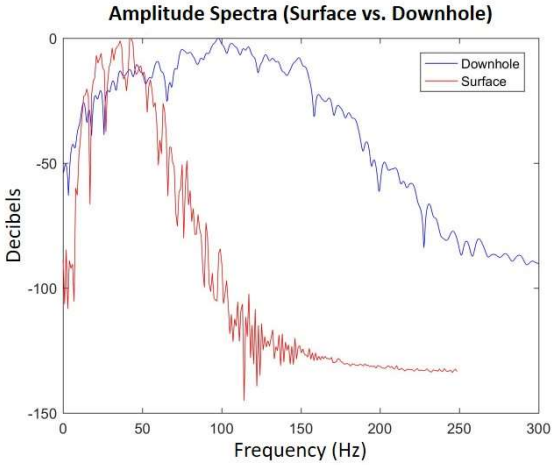

Stage 2:

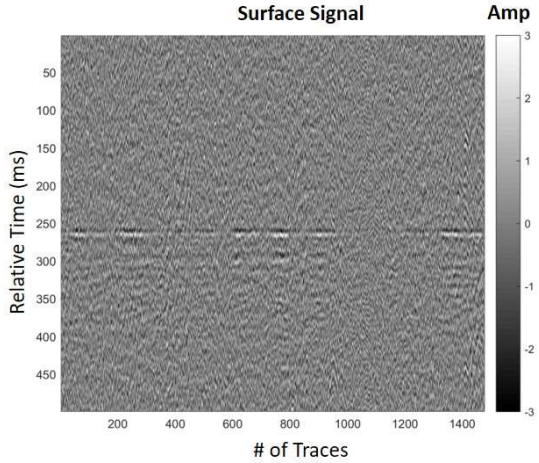

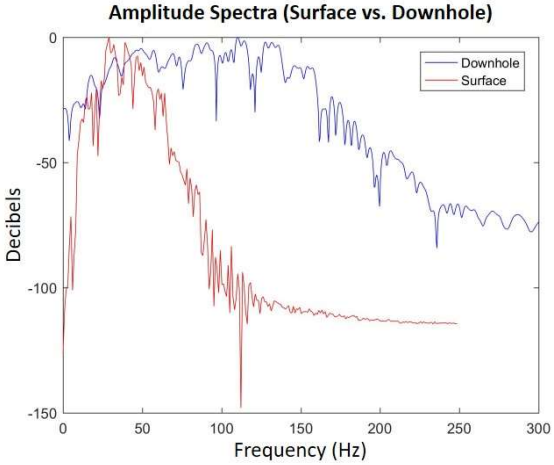

Stage 3:

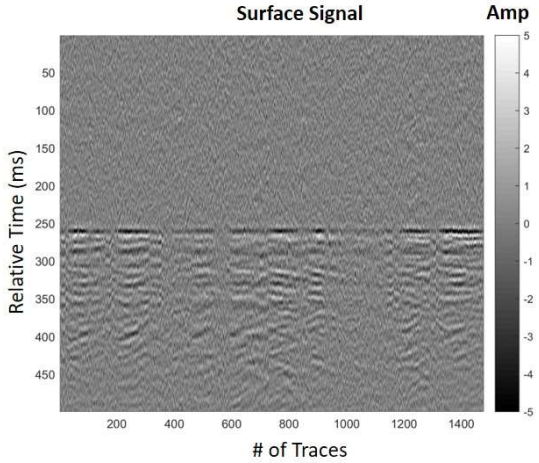

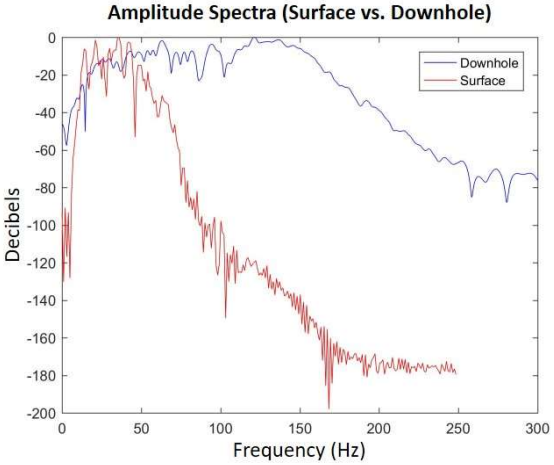

Stage 4:

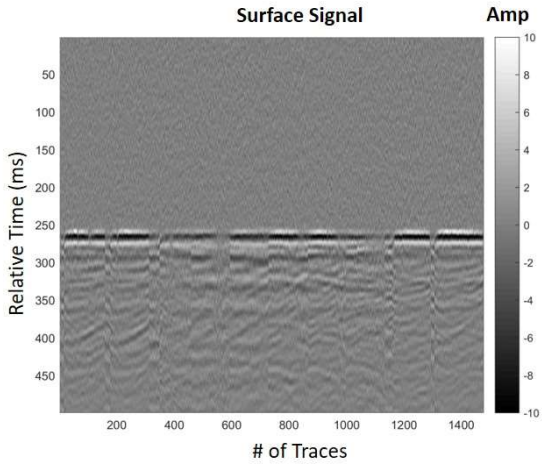

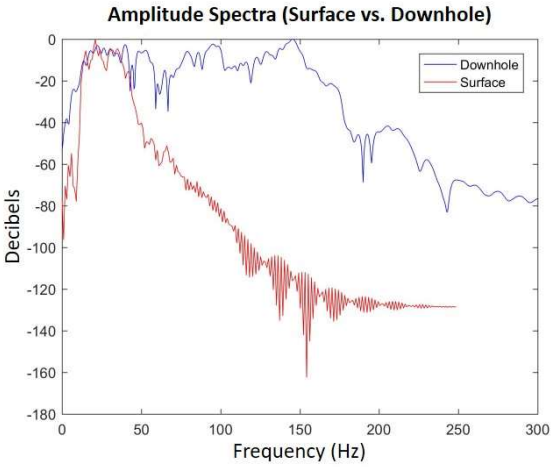

Stage 5:

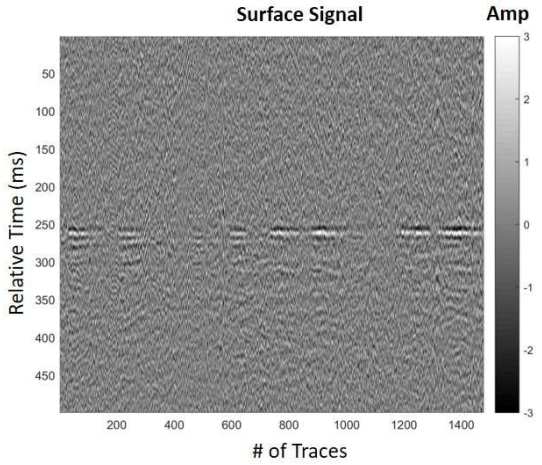

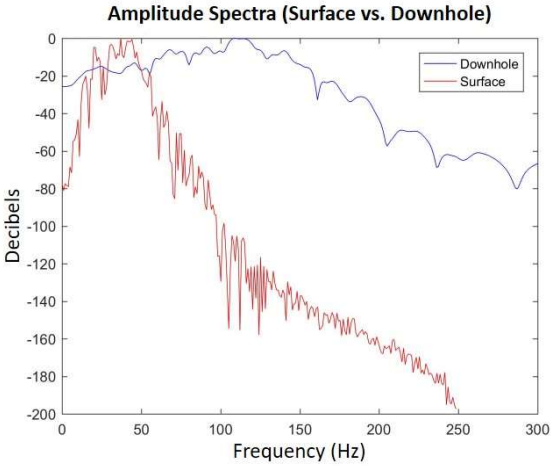

Stage 6:

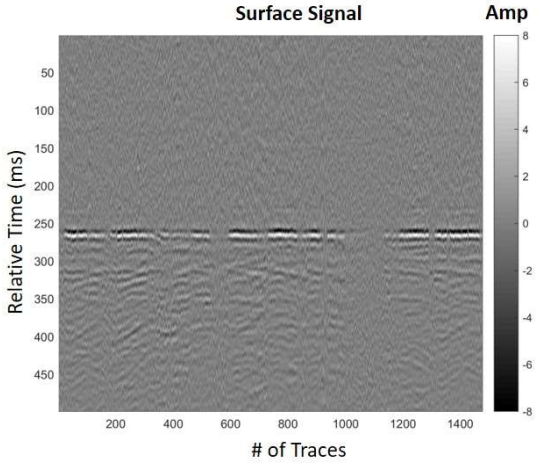

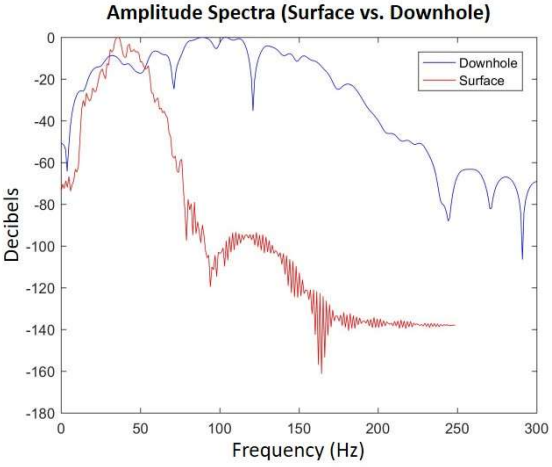

Stage 7:

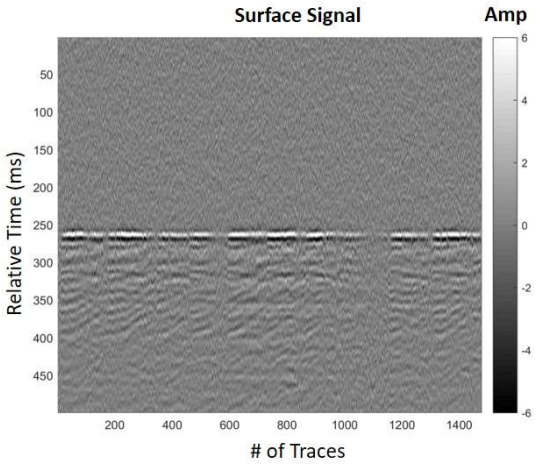

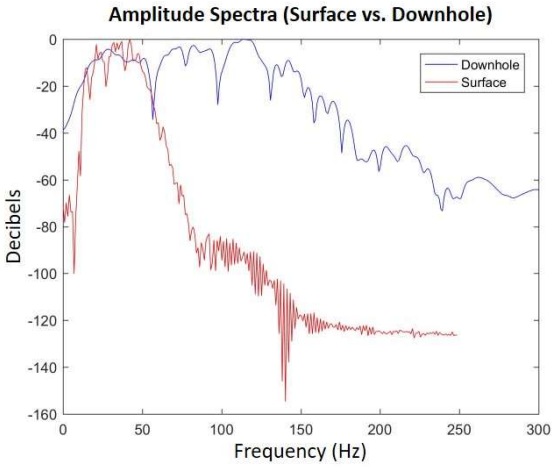

Stage 8:

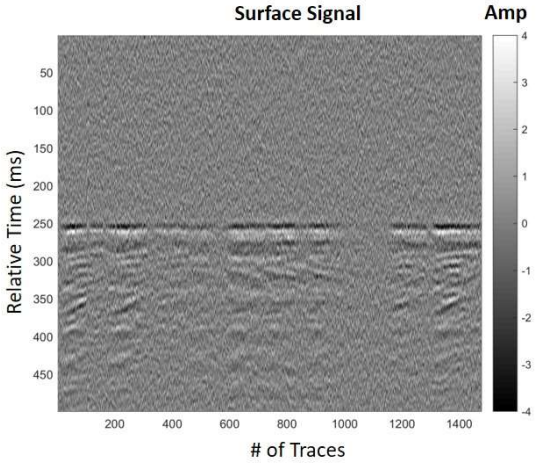

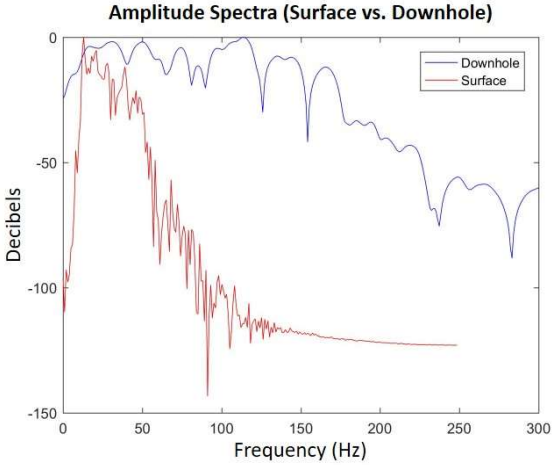

Stage 9:

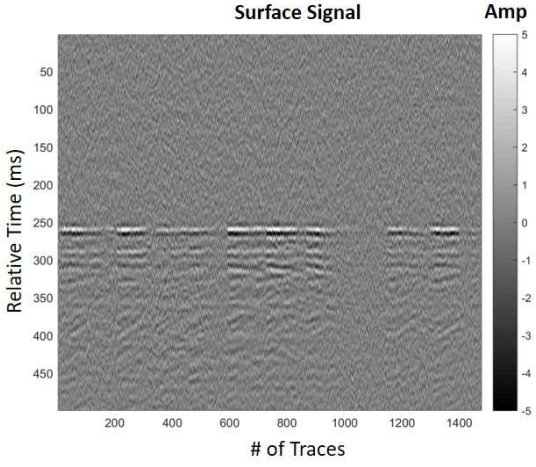

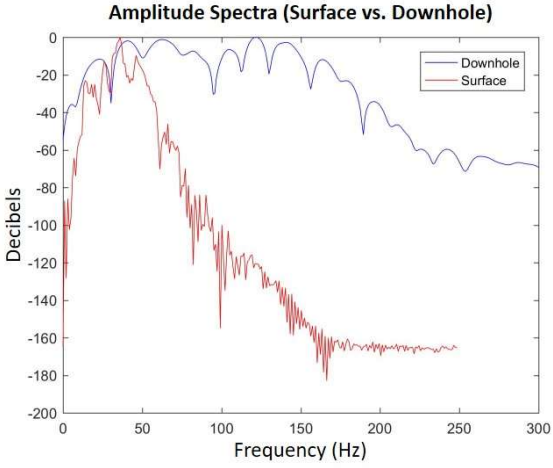

Stage 10:

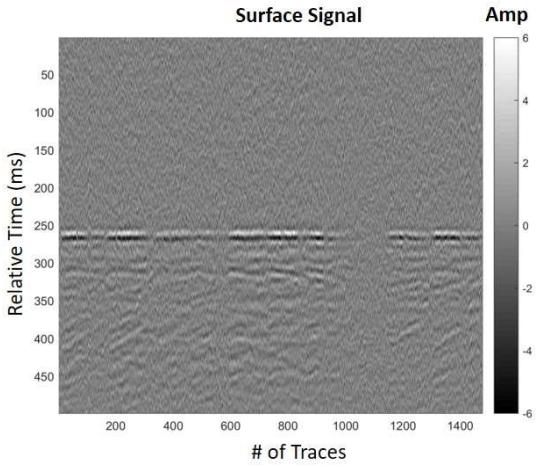

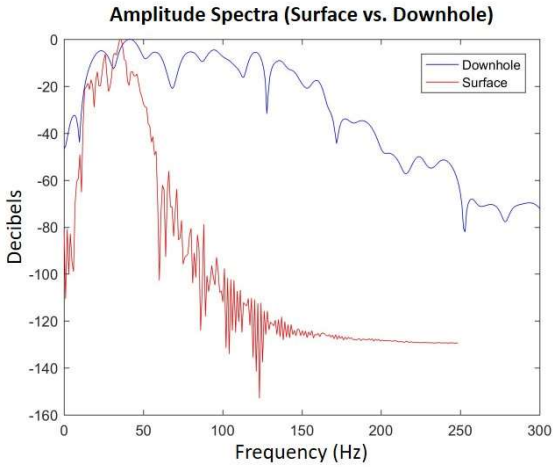

Stage 11:

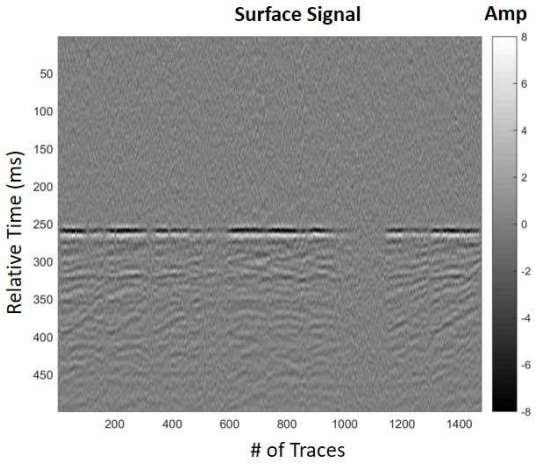

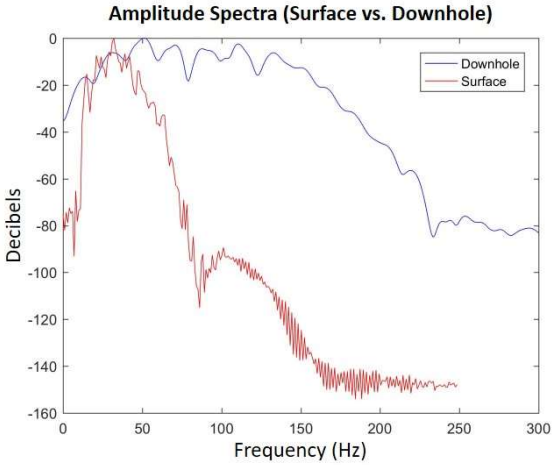

Stage 12: